

**Endoscopic imaging techniques for gas phase temperature, combustion, fuel
films, and soot in internal combustion engines**

Von der Fakultät für Ingenieurwissenschaften, Abteilung Maschinenbau und Verfahrenstechnik

der

Universität Duisburg-Essen

zur Erlangung des akademischen Grades

eines

Doktors der Ingenieurwissenschaften

Dr.-Ing.

genehmigte Dissertation

von

Muhammad Ali Shahbaz

aus

Lahore, Pakistan

1. Gutachter: Prof. Dr. Sebastian A. Kaiser
2. Gutachter: Prof. Dr. Christof Schulz

Tag der mündlichen Prüfung: 14. Juli 2021

Acknowledgments

The presented work was created during my time at the Institute for Combustion and Gas Dynamics - Reactive Fluids at the University of Duisburg-Essen. I would like to sincerely express my regards to all the people who, scientifically and emotionally, contributed towards the successful completion of this amazing journey of my life.

First, my wholeheartedly gratitude to my supervisor Prof. Dr. Sebastian A. Kaiser for providing the best possible supervision one can imagine. His continuous support, motivation, and patient answers to all my silly question has made it possible for me to complete this journey. I would also like to acknowledge his amazing support outside of the academic activities and sincerely thank him for providing a close, friendly, and cooperative environment in the engine group.

Second, I want to thank my colleagues at the engine group, with whom I worked and learned a lot. In particular, I would like to thank Martin Goschütz who supervised my master's thesis and then became my colleague when I started my PhD, and generously transferred all his knowledge to me. Special thanks to Patrick Kranz, Niklas Jüngst, Ming Zhao, Kai Banke, Judith Laichter, Julian Heimrath, Sebastian Wiemann, Philipp Barth, Daniel Fuhrmann, and Syahar Shawal for the good time spent. I will miss all those coffee break discussions with these wonderful people every day. I would also like to thank Jan Geiler and Dr. Roman Grzeszik for their help and support during my measurement campaigns at Bosch GmbH.

I would like to thank Natascha Schlösser, Beate Endres, Birgit Nelius, Jörg "Aldi" Albrecht, and Erdal Akyildiz for their constant support and helping with whatever was needed, wherever and whenever. Additionally, I would like to express my gratitude for all the help I got from student assistants, Arno Litterscheidt, Jörg Wende, and Joel Albrecht, and graduate students, Dominik Meller, Sobri Daud, Sadik Shaik, Esma Karapinar, and Emre Kara, that I supervised and worked with.

In the end, I would like to deeply acknowledge my parents, who raised me in the best possible way and always supported me. My best regards to my sisters, Dr. Ayesha and Dr. Arfa, for always being proud of me. Last but not the least, my special thanks to my wife Bushra and my children Aroosh and Hashim, for the love and color they brought in my life, and their patience and support during my work.

Abstract

In this work, a large-aperture hybrid UV endoscope system is used for minimally-intrusive optical diagnostics to visualize various phenomena in the combustion chamber of spark-ignition engines. The first part of the thesis describes the characterization of the UV endoscope system. To make the endoscopic imaging more universally applicable, the hybrid diffractive-refractive relay element (DOE) of the endoscope system was replaced by commercial UV camera lenses, and several combinations were compared in terms of resolution, brightness, and chromatic aberration. The modulation transfer function (MTF) was measured to quantify the resolution. With an unintensified CCD camera, endoscope systems using commercial camera lenses had better resolution. However, with an intensified camera the system with the DOE in the design wavelength range had the best overall performance. Selected imaging systems were used in a port fuel injection (PFI) spark-ignition engine to image OH^{*}-chemiluminescence, with results consistent with those from bench-top characterization.

The second part focuses on gas-phase temperature measurements in PFI spark-ignition engine based on two-color laser-induced fluorescence (LIF) thermometry. The red-shift of the anisole fluorescence spectrum with increasing temperature and oxygen partial pressure was exploited for ratiometric temperature measurements based on single-shot images. The available spectroscopic data was used to develop several models, which were calibrated in-situ. Calibration models with two-step interpolation yielded good agreement with the adiabatic temperature during compression. Temperature images based on single-shots were obtained using one selected model, showing a near-uniform and a stratified temperature distribution during the compression stroke and gas exchange, respectively.

The third part of the thesis describes endoscopic imaging in an all-metal direct-injection spark-ignition engine. Liquid fuel films on the piston were visualized via LIF, and the effects of injection time, injection pressure, engine temperature, and combustion on the fuel-film evaporation were investigated, with engine temperature having the primary effect on evaporation. LIF from fuel films and soot incandescence were also visualized quasi-simultaneously with an intensified double-frame CCD camera, and the effect of engine temperature on the spatial location of fuel films and soot was investigated. Finally, high-speed imaging showed the spray, chemiluminescence, and soot incandescence, with results broadly consistent with fuel-film LIF and soot incandescence imaging.

Kurzfassung

In dieser Arbeit wird ein hybrides UV-Endoskopsystem für eine minimalinvasive optische Diagnostik zur Visualisierung verschiedener Phänomene im Brennraum von Ottomotoren eingesetzt. Der erste Teil der Arbeit beschreibt die Charakterisierung des UV-Endoskopsystems. Für universellere Einsetzbarkeit des Systems wurde das diffraktiv-refraktive Hybrid-Relayelement (DOE) des Endoskopsystems mit kommerziellen UV-Kameraobjektiven ersetzt. Verschiedene Kombinationen wurden hinsichtlich Auflösung, Helligkeit und chromatischer Aberration verglichen. Die Modulationsübertragungsfunktion (MTF) wurde zur Quantifizierung der Auflösung gemessen. Mit einer nicht-bildverstärkten Kamera haben Endoskopsysteme mit kommerziellen Objektiven eine bessere Auflösung. Mit einer bildverstärkten Kamera hat jedoch das System mit DOE im Auslegungs-Wellenlängenbereich die beste Gesamtleistung. Ausgewählte Abbildungssysteme wurden in einem Ottomotor mit Saugrohreinspritzung zur Abbildung der OH*-Chemilumineszenz eingesetzt, wobei die Ergebnisse mit denen der Charakterisierungsmessungen übereinstimmten.

Der zweite Teil konzentriert sich auf die Messung der Gasphasentemperatur in einem Ottomotor mit Saugrohreinspritzung, basierend auf der Thermometrie durch 2-Farben-Laser-induzierte Fluoreszenz (LIF). Die Rotverschiebung des Anisol-Fluoreszenzspektrums mit steigender Temperatur und steigendem Sauerstoffpartialdruck wurde für die verhältnisbasierte 2-Farben-Messung der Temperatur im Einzelschuss ausgenutzt. Aus den verfügbaren spektroskopischen Daten wurden mehrere Modelle entwickelt, die in-situ kalibriert wurden. Modelle mit 2-Schritt-Interpolation ergeben eine gute Übereinstimmung mit der adiabatischen Kompressionstemperatur. Gasphasentemperaturbilder wurden auf der Basis von Einzelschüssen mit einem ausgewählten Modell generiert. Sie zeigen eine nahezu gleichförmige Temperaturverteilung während des Kompressionshubs und ausgeprägte Inhomogenität während des Gaswechsels.

Der dritte Teil der Arbeit beschreibt endoskopische Bildgebung in einem direkteingespritzenden Ottomotor. Zunächst wurden flüssige Kraftstofffilme auf der Kolbenoberfläche durch LIF visualisiert und die Auswirkungen der Einspritzzeit, des Einspritzdrucks, der Motortemperatur und der Verbrennung auf die Verdampfungszeit des Kraftstofffilms untersucht, wobei die Motortemperatur den größten Einfluss auf die Verdampfung hatte. LIF von Kraftstofffilmen und Rußinkandeszenz wurden quasi-simultan mit einer bildverstärkten Doppelbild-CCD-Kamera visualisiert und der Einfluss der Motortemperatur auf die räumliche Struktur von Kraftstofffilmen und Ruß untersucht. Schließlich wurden mit Hochgeschwindigkeitsaufnahmen das Spray, die Chemilumineszenz und die Rußinkandeszenz visualisiert, wobei die Ergebnisse weitgehend mit den Aufnahmen durch LIF und Rußinkandeszenz konsistent waren.

Table of contents

Acknowledgments	I
Abstract	II
Kurzfassung	III
Table of contents	IV
Nomenclature	VI
1 Introduction	1
2 Theoretical background	5
2.1 Optical diagnostics in internal combustion engines	5
2.1.1 Chemiluminescence	6
2.1.2 Laser-induced fluorescence.....	6
2.1.3 Soot luminosity	10
2.1.4 Mie scattering.....	11
2.2 Optical aberrations.....	11
2.2.1 Monochromatic aberrations.....	12
2.2.2 Chromatic aberrations	15
2.3 Resolution measurement.....	16
3 Endoscopic imaging in combustion engines	21
3.1 Imaging with conventional endoscopes.....	21
3.2 Hybrid UV endoscope system	22
3.2.1 Optical design of the hybrid UV endoscope system	22
3.3 Illumination endoscopes	25
3.3.1 Sheet illumination endoscope.....	25
3.3.2 Inhomogeneous illumination endoscope.....	27
3.3.3 Flood illumination endoscope	28
3.4 Review of previous work with the hybrid UV endoscope system.....	29
3.4.1 Bench-top demonstration experiments.....	29
3.4.2 OH* and broadband chemiluminescence imaging.....	31
3.4.3 Laser-induced fluorescence imaging.....	38
4 Characterization of the UV endoscope system	43
4.1 Introduction.....	43
4.2 Methods	43
4.2.1 Imaging systems	43
4.2.2 Experiment	44
4.3 Measurements and post-processing	47
4.3.1 Images	47
4.3.2 Modulation transfer function.....	48

4.4	Results.....	50
4.4.1	Chromatic aberrations	50
4.4.2	Quasi-monochromatic resolution	52
4.4.3	Light collection efficiency	53
4.4.4	Effect of magnification.....	54
4.4.5	Effect of the intensifier on the resolution.....	56
4.4.6	OH*-chemiluminescence imaging	56
5	Endoscopic two-color anisole-LIF temperature imaging in a PFI engine.....	59
5.1	Introduction.....	59
5.2	Engine and optics.....	60
5.3	Anisole vs. toluene as a fuel tracer	64
5.4	Gas-phase temperature measurement	67
5.4.1	Spectroscopic model	67
5.4.2	Calibration.....	70
5.4.3	Extrapolation of calibrated signal model	76
5.4.4	Images and post-processing	80
5.4.5	Results	84
5.5	Experimental challenges	89
5.5.1	Laser	90
5.5.2	Engine.....	90
6	Spray, fuel film and combustion imaging in a DISI engine	92
6.1	Introduction.....	92
6.2	Experiment.....	93
6.2.1	Engine and optics	93
6.2.2	Operating conditions	95
6.3	Image post-processing	97
6.4	Results.....	99
6.4.1	LIF imaging of fuel films	99
6.4.2	Simultaneous fuel-film LIF and soot incandescence imaging	103
6.4.3	High-speed visualization of spray, flame front, and soot incandescence.....	106
7	Conclusions.....	110
8	References.....	116
8.1	Publications.....	123
8.1.1	Journal publications.....	123
8.1.2	Conference proceedings	123
8.2	Supervised student theses	125
9	Appendices.....	126

Nomenclature

List of symbols

Symbol	Unit	Description
ϕ_{fl}	-	Fluorescence quantum yield
ξ_c	lp/mm	Cut-off frequency
σ_{abs}	mm ²	absorption cross-section of the tracer
Π	-	collection efficiency of the detection system
η	-	Quantum efficiency of the detection system
λ	mm	Wavelength of light
λ	-	Relative air/fuel ratio
ξ	lp/mm	Spatial frequency
d	mm	Working distance (of relay lens)
f	mm	Focal length
$f/\#$	-	f-number of the objective
I_{laser}	-	Intensity of incident laser
m	-	Relay magnification
n_{tr}	m ⁻³	Tracer number density
p	bar	Pressure (generic)
p_{O_2}	mbar	Partial-pressure of oxygen
$S_1, S_2 \dots$	eV	Electronic states
S_{blue}	count	Fluorescence signal in blue channel
S_{red}	count	Fluorescence signal in red channel
S	count	Fluorescence signal from tracer
SR	-	Signal ratio (of signals in red and blue channel)
T	K	Temperature (generic)
V	m ³	Volume (generic)
w	mm	Pixel width

List of abbreviations

Abbreviation	Full description
aIT	After ignition time
BDC	Bottom-dead center
BG	Background
BMEP	Brake mean-effective pressure
BP	Bandpass (filter)
BS	Beam splitter
CA	Crank angle
CAI	Controlled auto-ignition
CCD	Charge-coupled device
CFD	Computational fluid dynamics
CL	Chemiluminescence
CMOS	Complementary metal-oxide semiconductor
CNG	Compressed natural gas
DC	Direct current
DISI	Direct-injection spark-ignition
DOE	Diffractive optical element
ECU	Engine control unit
EEA	European environment agency
EGR	Exhaust gas recirculation
ESF	Edge spread function
EU	European union
EV	Exhaust valve
FAR-LIF	Fuel/air ratio laser-induced fluorescence
FF	Flatfield
FOV	Field-of-view
FQY	Fluorescence quantum yield
FS	Fused silica
FWHM	Full-width at half-maximum
GDI	Gasoline direct injection
HCCI	Homogeneous-charge compression-ignition
HRR	Heat release rate
HS	High speed

HWHM	Half-width at half-maximum
IC	Internal combustion (engine)
ICCD	Intensified charge-coupled device
IMEP	Indicated mean-effective pressure
IR	Infrared
IRO	Intensified relay optic
ISC	Intersystem crossing
ISO	International Organization for Standardization
ITO	Institute for Technical Optics
IV	Intake valve
IVC	Intake valve close (time)
IVG	Institute for Combustion and Gas Dynamics
KE	Knife edge
LED	Light-emitting diode
LIF	Laser-induced fluorescence
LII	Laser-induced incandescence
LP	Longpass (filter)
LSF	Line spread function
MTF	Modulation transfer function
Nd:YAG	Neodymium-doped yttrium aluminum garnet
OTF	Optical transfer function
PaREGEn	Particle Reduced, Efficient Gasoline Engines (EU project)
PCI	Institute of Physical Chemistry
PFI	Port-fuel injection
PIV	Particle image velocimetry
PLIF	Planar laser-induced fluorescence
RGB	Red, green, blue (relevant for light emission and camera sensors)
RIM	Refractive index matching
RMS	Root mean square
ROI	Region of interest
RON	Research octane number
SI	Spark ignition
SIDI	Spark-ignition direct-injection
SLIPI	Structured laser illumination planar imaging
SNR	Signal-to-noise ratio

SOI	Start of injection
TDC	Top-dead center
USAF	United States Air Force
UV	Ultraviolet
VIS	Visible
VR	Vibrational relaxation
VTEC	Variable Valve Timing & Lift Electronic Control

1 Introduction

Among the many incredible engineering developments during the past few hundred years, internal combustion engines (IC engines) are one of the most significant ones. They have greatly affected the quality of human life in many ways, but most importantly, the mobility on both the local and global scale. However, despite all the positive impacts on human life by the IC engines, they have had a negative impact on the sustainability of life and have recently received much criticism and restrictions due to production of pollutants and greenhouse gases such as CO, CO₂, SO_x, NO_x, unburnt hydrocarbons, and particulate matter such as soot. In 2016, according to European Environment Agency (EEA), the transport sector was responsible for more than half of all NO_x emissions and contributes significantly (around 10 % or more) to the total emissions of the other pollutants [1], and the share of road transport alone was 28 % for NO_x, and 19 % for CO [1]. Even though stricter environmental legislations are implemented in different countries and engines that are more efficient are being produced, the global pollutant emissions from road transport are still expected to increase due to increasing number of consumers worldwide. To reduce the emissions from the road transport and from the other combustion processes, engineers and scientists are looking for new and more efficient technologies. One of the innovative substitutes for IC engines in the road transport are electric vehicles. These electric vehicles do help in reducing the local pollutant concentrations in densely populated urban areas, but they are limited by the controversies revolving around the production and capacity of batteries, and the availability of infrastructure for charging stations. Also, the real advantage of these electric vehicles can only be realized once the production of electricity used for charging their batteries is entirely, or at least mostly, from the renewable sources, rather than from fossil fuels. Therefore, the IC engines are still expected to remain the main driver of road transport at least in the near future. However, with the gradual introduction of stricter environmental legislations, e.g., Euro 6d emission standards in 2020, further reduction in emissions is needed.

One of the approaches to increase the efficiency of IC engines and reduce emissions are advanced fuel injection and combustion strategies such as direct-injection

spark-ignition (DISI), controlled auto-ignition (CAI), and homogeneous-charge compression-ignition (HCCI). To visualize the effect of the injection and combustion strategies on the efficiency of the IC engines, a detailed and systematic investigation of the in-cylinder processes is required. This includes investigating the in-cylinder flow patterns, air-fuel mixing, flame propagation, formation of the intermediate species that may lead to formation of particular pollutants and measuring the concentration of different pollutants. Measuring the crank-angle resolved cylinder pressure provides temporally resolved information only about the global thermodynamic quantities like heat release rate (HRR) and mean effective pressure. Other quantities like species concentration or temperature have been measured in the past by fast measurement probes inserted in the combustion chamber. These measurements can sometimes give temporally resolved information about the measured quantity, but the probe affects the local flow. On the other hand, optical diagnostics of the in-cylinder processes provide both temporal and spatial information in high resolution about the in-cylinder processes and are non-intrusive in nature. Typically, research engines with transparent liners and transparent pistons are used for this purpose. These “optical” engines provide good optical access to visualize the in-cylinder processes, but the heat transfer and speed/load range are compromised. A complementary approach is using minimally invasive endoscopes in all-metal engines. These “endoscopic” engines have nearly unmodified thermodynamic properties and can operate over the same speed/load range as a production engine.

Various endoscopes have been used in the past for imaging different in-cylinder phenomena. Most of these endoscopes were essentially modified medical endoscopes that have poor light collection efficiency, and are only transparent in the visible spectrum. Therefore, their application was limited to relatively bright events in the visible spectrum. In this work, a modular large-aperture UV-transparent hybrid endoscope system is used, which was designed and developed by Institute of Technical Optics (ITO), University of Stuttgart, in collaboration with Institute of Physical Chemistry (PCI), University of Heidelberg and Institute for Combustion and Gas Dynamics (IVG), University of Duisburg-Essen [2]. This hybrid UV endoscope system consists of two parts: a front endoscope and a refractive/diffractive hybrid relay lens for specific wavelength ranges. Initial testing of the hybrid UV endoscope system in bench-top experiments and in an all-metal endoscopic engine were performed at the Institute for Combustion and Gas Dynamics (IVG), University of Duisburg-Essen [3-5].

The custom design and manufacture of the diffractive element inside the hybrid relay is expensive and limits the application of a given endoscopic system. To make the hybrid UV endoscope system more universally usable, in chapter 4, the hybrid relay lens was replaced with different commercial UV lenses and the system performance of various combinations was compared in terms of resolution, brightness, and limiting the chromatic aberration. The resolution of the system was quantified as the half-width-at-half-maximum (HWHM) of the modulation transfer function (MTF) determined by the slanted-edge method (ISO 12233 [6]). The effect of an image intensifier on the system performance was investigated. Finally, the selected imaging systems were used with an intensified camera to visualize OH*-chemiluminescence in an all-metal port-fuel injected commercial gasoline engine with endoscopic access.

The hybrid UV endoscope system is used to implement advanced optical diagnostics in all-metal engines that typically are performed in optical engines only. Chapter 5 describes an improved method to determine the gas-phase temperature during the compression stroke and the gas exchange via laser-induced fluorescence (LIF) of anisole. This work is in direct extension of previous work at IVG. The technique for determination of gas-phase temperature, two-color LIF thermometry, exploits the temperature dependence of the anisole LIF spectrum, which shifts towards longer wavelengths with an increase in temperature. The signal ratio in two spectral bands is determined by pixel-wise signal ratio of the bands. The temperature is determined by a signal model based on the photophysical properties of anisole and the quantum efficiency of the detection train, and also takes into account the spectral shift of the LIF spectrum due to variation in oxygen partial pressure. The signal model was calibrated in situ in the standing engine and extrapolated as the available photophysical data and calibration measurements did not cover the complete temperature range of the compression stroke of the test engine at the given operating point. This resulted in spatially resolved single-shot temperature images during the compression stroke and the gas exchange process.

Since it had been concluded that the front endoscope of the UV endoscope system can indeed be coupled with commercial UV lenses without any disadvantage in terms of system resolution and with the additional benefit of a wider spectral range, this configuration was used in experiments in an all-metal single-cylinder DISI engine. Chapter 6 describes such applications where the front endoscope was coupled with commercial UV lenses, and imaging of spray, piston fuel-films, and combustion was performed in the UV and visible.

First, the evaporating fuel films on the piston surface were visualized via LIF using two fuels: a commercial gasoline, and a mixture of isooctane and toluene. The effects of injection timing, injection pressure, engine temperature and combustion on fuel-film evaporation were investigated, which was quantified as survival time in cycles. Second, the fuel films were visualized quasi-simultaneously with imaging measurements of natural soot incandescence, giving insights into the instantaneous spatial correlation between evaporating fuel films and soot. Finally, high-speed color combustion imaging was performed, showing the temporal evolution of spray, broadband chemiluminescence from the flame front, and soot incandescence.

2 Theoretical background

This chapter gives a brief introduction to the most important optical phenomena encountered or utilized in this thesis. A discussion of the state of the art and the recent previous work is given at the beginning of each subsequent chapter. A brief review of previous work with the UV endoscope system is given in section 3.4.

2.1 Optical diagnostics in internal combustion engines

Optical diagnostics can visualize various phenomena in IC engines such as flame front propagation, intermediate species, 2D temperature fields, in-cylinder flow patterns, fuel films, soot incandescence, etc. Table 2.1 shows few such in-cylinder phenomena and the optical diagnostics used to visualize them. In this section, the principles of optical diagnostics used in this work will be briefly explained.

Table 2.1: In-cylinder phenomena and suitable optical diagnostics techniques

Phenomenon	Optical diagnostics technique
Flame front visualization, apparent flame speed	Flame luminosity, chemiluminescence
Temperature	Two-color laser-induced fluorescence (LIF) thermometry
Air-fuel ratio	Fuel/air ratio LIF (FAR-LIF)
In-cylinder flow	Particle image velocimetry (PIV)
Piston fuel films	LIF, Refractive index matching (RIM)
Soot	Natural incandescence, laser-induced incandescence (LII)
Spray, preferential evaporation	Mie scattering, LIF

2.1.1 Chemiluminescence

During combustion, many short-lived intermediate species are formed. Some of these are electronically excited by the energy provided by the reaction enthalpy and relax to their ground state by emitting photons. This emission of photons is called chemiluminescence. The emitted light from each species has characteristic wavelengths or bands. Interpreting these spectra can be used to find the reactants or spatial location of reaction products. This information enables, e.g., the characterization of the combustion process or the determination the combustion air ratio and the heat release rate [7, 8].

Table 2.2: Emission wavelengths of some combustion species [9]

Species	Wavelength [nm]
OH*	306–315
NH*	336
CN*	359–386
CH*	380,431
C ₂ *	469–476,510–516
CH ₂ O*	395,423
CO ₂ *	broadband visible

Some typical species produced during combustion and their chemiluminescence wavelengths are shown in Table 2.2 [9]. Since most of these species emit UV and blue light, non-sooting flames often appear blue in color. The dominant orange-yellow light from some flames is mainly due to incandescence from heated soot particles.

The hydroxyl radical (OH) is formed during combustion via various reaction pathways [10-12]. The chemiluminescence of OH* is commonly used as a marker for the flame front [13-17] as it exists in the high-temperature reaction zone of the flame.

2.1.2 Laser-induced fluorescence

Laser-induced fluorescence (LIF) is the spontaneous emission of light, when a molecule is excited to a higher state of energy by absorbing a photon from a laser beam and relaxes from the singlet to the ground electronic state by spontaneous emission of photons with

wavelengths different from that of the absorbed one. The spectrum of the emitted light is strongly dependent on the electronic configuration of the absorbing molecule, wavelength of the incident light, and ambient conditions. Detailed descriptions of the photophysical processes are given in [18, 19], and are briefly summarized below.

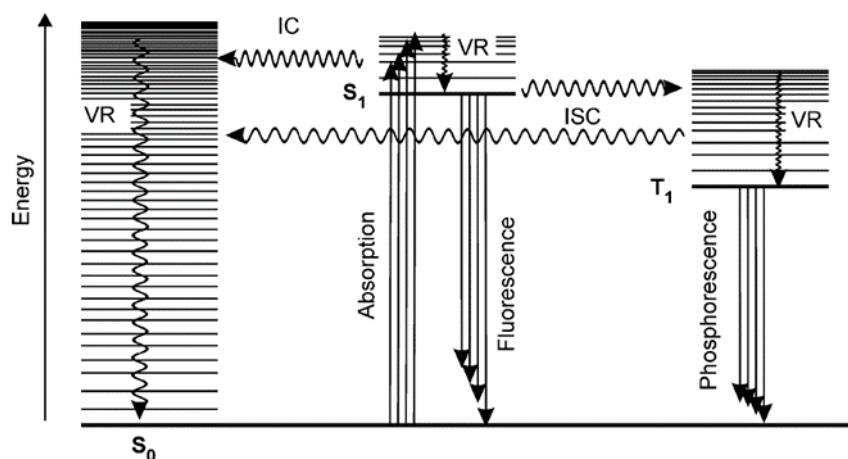


Figure 2.1: Jablonski diagram showing the transition of electrons during excitation and relaxation [19].

Figure 2.1 shows the Jablonski diagram explaining the processes involved in the excitation and relaxation of the fluorescing molecule. S_0 and S_1 represent the ground and first singlet electronic states and T_1 represents the triplet state. Each electronic state is further discretized into vibrational and rotational levels (not shown here). The population of the vibrational levels in each state are described by the Boltzmann distribution. When the molecule in the ground state S_0 absorbs a photon (from the laser in this case), it may be excited to the S_1 state and occupy one of the vibrational and rotational levels of S_1 (or the higher state S_2 if the energy of the absorbed photon is high enough). Shortly afterwards, the molecule relaxes to the lowest vibrational level of the excited state S_1 by vibrational (VR) and rotational relaxations, transferring the energy to other molecules.

From this level, the molecule can relax to the ground state by different chemical and physical processes. The latter are of interest in this work and fall into three categories [19].

- Radiative processes: The excess energy is emitted by spontaneous emission of photons.
- Non-radiative processes: The excess energy is thermalized by vibrational and rotational energy transfer to neighboring molecules.
- Collisional quenching: Electronic excitation of colliding molecules, i.e., electronic energy transfer.

The processes of the first two categories are shown in Figure 2.1. The radiative processes are represented by straight lines and non-radiative by curved lines. If the molecule relaxes from S_1 to S_0 by spontaneous emission of a photon, the process is called fluorescence. The wavelengths of the emitted photon are governed by the energy gap between the two electronic states and the temperature-dependent Boltzmann distribution, and are typically shorter (red-shifted) than the wavelength of the absorbed photon due to energy losses during absorption and relaxation. Fluorescence has typical lifetimes of 1–100 ns, but for ketones it is on the order of microseconds due to symmetry and orbital forbidden S_1 to S_0 transition [19]. If the molecule first undergoes a transition from S_1 to triplet energy state T_1 by intersystem crossing (ISC) and relaxes from T_1 to S_0 by emitting a photon, that process is called phosphorescence. Phosphorescence is significantly longer lived due to spin-forbidden radiative relaxation to S_0 , and has typical lifetimes of milliseconds to seconds [19]. The molecule can also lose its excess energy by exciting vibrations and rotations in the colliding molecules, which is a non-radiative process and represented by internal conversion (IC) followed by vibrational relaxation (VR) in the Jablonski diagram in Figure 2.1.

LIF is extensively used to investigate combustion-relevant processes. Often, a fluorescent molecule (tracer) in a predetermined quantity is added to a non-fluorescent base-fuel. The fluorescence from the laser-excited tracer can be captured by a suitable camera and post-processed to obtain information about the quantity of interest. The application of LIF to obtain quantitative information on fuel concentration and composition, air/fuel ratio, temperature, and concentration of residual gas are summarized in [19, 20].

2.1.2.1 Two-color LIF thermometry

The two-color LIF thermometry is a non-invasive temperature measurement method that uses the temperature-dependent spectral shift of LIF of aromatic tracers towards longer wavelengths (red-shift) to measure the temperature [19]. Due to the increase in temperature, the probability to populate higher vibrational levels of the ground electronic state increases, which decrease the energy gap for the molecule relaxing from the excited state and emitting a photon. Due to the smaller energy gap, the wavelengths of the emitted photons are therefore longer or red-shifted. The detailed quantum-mechanical explanation of this spectral shift is discussed in [18]. The fluorescence signal detected by a camera for weak

excitation at a given wavelength and low tracer number density is given by the linear relation:

$$S = I_{laser} \cdot V \cdot n_{tr}(p, T) \cdot \sigma_{abs}(T) \cdot \phi_{fl}(T, p, n_i) \cdot \Pi \cdot \eta \quad Eq\ 2.1$$

where

I_{laser}	Intensity of the incident laser
V	Probe volume
$n_{tr}(p, T)$	Tracer number density
$\sigma_{abs}(T)$	Absorption cross-section of the tracer
$\phi_{fl}(T, p, n_i)$	Fluorescence quantum yield (FQY)
Π	Collection efficiency of the detection system
η	Quantum efficiency of the detection system

A rearrangement of Eq 2.1 for ratio of signal intensities detected in two channels yields:

$$\begin{aligned} \frac{S_{red}}{S_{blue}} &= \frac{I_{laser} \cdot V \cdot n_{tr}(p, T) \cdot \sigma_{abs}(T) \cdot \phi_{fl(red)}(T, p, n_i) \cdot \Pi \cdot \eta_{red}}{I_{laser} \cdot V \cdot n_{tr}(p, T) \cdot \sigma_{abs}(T) \cdot \phi_{fl(blue)}(T, p, n_i) \cdot \Pi \cdot \eta_{blue}} \\ &= \frac{\phi_{fl(red)}(T, p, n_i) \cdot \eta_{red}}{\phi_{fl(blue)}(T, p, n_i) \cdot \eta_{blue}} \quad Eq\ 2.2 \end{aligned}$$

Eq 2.2 shows that the signal ratio depends on the temperature-dependent FQY and wavelength-dependent quantum efficiency of the detection system. The other terms in the equations influence the absolute intensity of the LIF signals and have no influence on the spectral shift of the LIF spectrum. Since the signal ratio is independent of the laser intensity, the shot-to-shot fluctuation in laser intensity and transverse profile do not influence the determination of the temperature. The FQY is also influenced by the bath gas composition. Oxygen is a significant bath gas species and, along with temperature, causes a spectral shift towards longer wavelengths with increase in number density or partial pressure [21, 22]. The correlation between the signal ratio and the temperature (or oxygen partial pressure if needed) can be determined from the available spectroscopic data. However, the ratio of the quantum efficiencies η of the detection system in Eq 2.2 must be calibrated with an identical optical setup for accurate determination of the temperature. The calibration can be done in-situ or in a separate experiment, where the temperature of a tracer-laden mixture is varied. Either way, the accuracy in the quantification of temperature is strongly dependent on the accuracy of the temperature calibration.

Figure 2.2a shows the peak-normalized LIF spectra of anisole shifting towards longer wavelengths with temperatures increasing from 298 to 675 K in air. The blue and red background represent the two spectral bands, or color channels, in which the fluorescence signals are integrated. Figure 2.2b shows the ratio of spectrally-integrated signals detected in two color channels indicated in Figure 2.2a as a function of temperature.

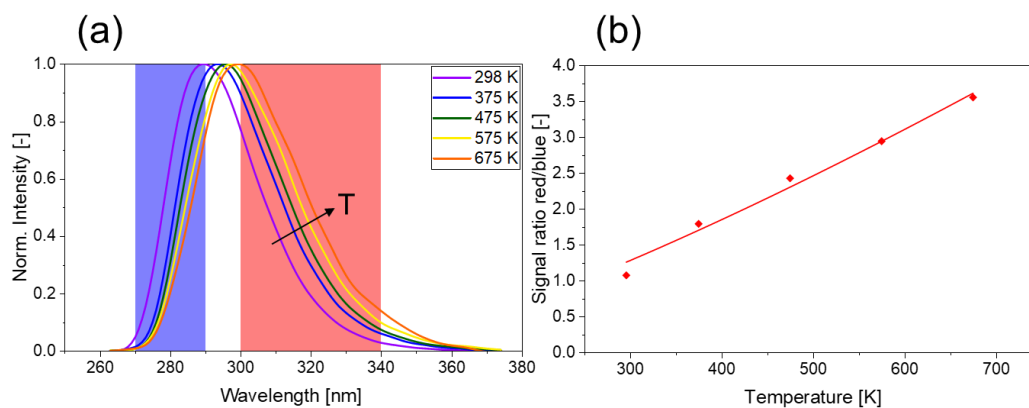


Figure 2.2: (a) Peak-normalized LIF spectra of anisole at different temperatures. The shaded regions show the ‘blue’ and ‘red’ detection channels for two-color LIF. The spectra shift towards longer wavelengths (red-shifted) with increase in temperature[23]. (b) Ratio of signals in red and blue channels with increase in temperature. Anisole was excited by a 266 nm laser in air at 1 bar.

We see that with increasing temperature, the LIF spectra of anisole are red-shifted, accompanied by an increase in the spectral width, leading to an increase in the signal in the red channel and a decrease in the blue. The signal intensities detected in each channel, resulting from the convolution of the temperature-dependent LIF spectra with the respective wavelength-dependent detection quantum efficiency, yield a signal ratio that can be used to determine the temperature.

2.1.3 Soot luminosity

Soot is produced as the result of incomplete combustion in an oxygen-depleted environment. Due to high temperatures in the flame soot emits significant light as black-body radiation following Planck’s law. A typical example of a sooting flame is a candle flame, which is a diffusion flame and has very little oxygen in the center of flame resulting in incomplete combustion and soot formation. The characteristic yellow color of the candle flame is due to the high temperature, which governs the emission spectrum of the black-body radiation from the heated soot particles. According to Planck's law, a higher flame temperature increases the intensity of radiation and shifts the peak of the radiation

spectrum to shorter wavelengths. Imaging the soot luminosity is a line-of-sight integrating technique, and has been used in various investigations [13, 14, 24, 25]. For most combustion applications, the temperature of the flame is such that the black-body radiation from the soot is in the visible spectrum and can be captured relatively easily by cameras sensitive in the visible.

2.1.4 Mie scattering

Mie scattering is elastic scattering of light from particles with diameters similar to or larger than the wavelength of the incident light. Since it is an elastic process, no energy conversion or transfer takes place due to the interaction between the incident light and the particle, and the wavelength of the incident and the scattered light are therefore identical. The intensity of the scattered light is proportional to the square of the particle diameter. In IC engine research, Mie scattering has been used for the measurement of flow fields via particle imaging velocimetry (PIV) [26-28], or for spray diagnostics [29]. In combination with laser-induced fluorescence, Mie scattering is also used to investigate the drop-size distribution within sprays [30].

2.2 Optical aberrations

The discussion in this section is summarized from references [31] and [32]. In an ideal optical system, all rays of light from a single point in the object plane would converge to a single point in the image plane producing a sharp image. The path of the light rays through the optical system are defined by the laws of geometric optics. In the simplest case, the light rays in an optical system are traced using a 1st order approximation of the laws of geometric optics, also called paraxial approximation. The deviation of the light rays from the paraxial approximation are called optical aberrations. These aberrations occur because the simple paraxial approximation is not a completely accurate model of the effect of an optical system on light rays, rather than due to flaws in the optical elements. The paraxial approximation can only be used to characterize an optical system if the image field and numerical aperture is sufficiently small. This would result in an aberration-free system in case of monochromatic light. However, with increase in field size and aperture aberrations occur. While some of the aberrations can be reduced by optimizing the optical geometry of the lenses, others are inevitable due to boundary conditions. Some can be corrected in

post-processing, e.g., distortion. The lens aberrations are mainly classified in two main categories: monochromatic and chromatic aberrations.

2.2.1 Monochromatic aberrations

Monochromatic aberrations are also called Seidel aberrations, (after Philipp Ludwig von Seidel, 1821–1896). In 1857, he decomposed the third order monochromatic aberrations into five constituent aberrations that are briefly described below. All Seidel aberrations can be minimized by reducing the aperture and optimizing the curvatures of the elements of the optical system, the latter being the preferred choice since the former reduces the light collection efficiency of the optical system.

2.2.1.1 Spherical aberration

For lenses made with spherical surfaces, rays that are parallel to the optical axis but at different distances from the optical axis fail to converge on a single point. This happens because the light rays striking the spherical lens off-center are refracted more than those that strike close to the center, hence deviating from the paraxial approximation, as shown in Figure 2.3. The farther the rays are away from the optical axis, the greater is the magnitude of the spherical aberration. This aberration can be minimized by using an aspheric lens shape. In case of multiple lenses, spherical aberrations can be canceled by overcorrecting in some elements.

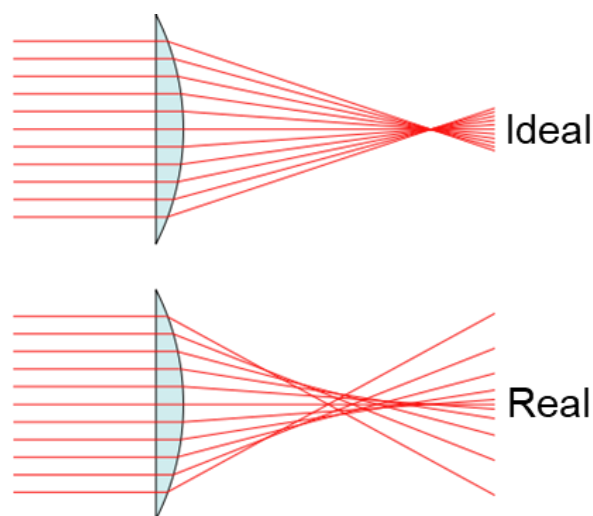


Figure 2.3: Spherical aberration. Top: Ideal lens, all rays are focused at a single point. Bottom: Real spherical lens, rays are not focused at a single point. Rays further away from the axis are more affected. Drawing is exaggerated [33].

2.2.1.2 Coma

Coma, or comatic aberration, is an aberration that causes rays from an off-axis point in the object plane to create a trailing "comet-like" blur directed away from the optical axis (in case of positive coma). A lens with considerable coma may produce a sharp image in the center of the field, but the image becomes increasingly blurred towards the edges.

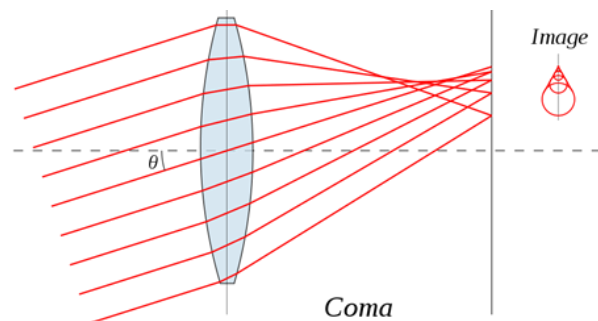


Figure 2.4: Coma or comatic aberration of a single lens [34].

Coma depends on the shape of the lens, thus a lens shape can be chosen with zero coma for a given object distance, but that lens would not be optimum for other object distances. For a more versatile solution, a combination of two lenses, which are corrected for zero coma at infinite object distance, can be used with appropriate distance between them. Lenses in which both spherical aberration and coma are minimized at a single wavelength are called bestform or aplanatic lenses.

2.2.1.3 Astigmatism

In an optical system with astigmatism, the local curvature is different in meridional and sagittal planes, resulting the rays in these planes having different foci. This could result from an object being off-axis or lens defects due to poor manufacturing. The latter is not truly a higher-order aberration but is also relevant to vision science and eye care since the human eye often exhibits this aberration due to imperfections in the shape of the cornea or the lens. Figure 2.5 shows a simplified case of astigmatism, where rays in sagittal and meridional planes are focusing at S_1 and T_1 points, respectively.

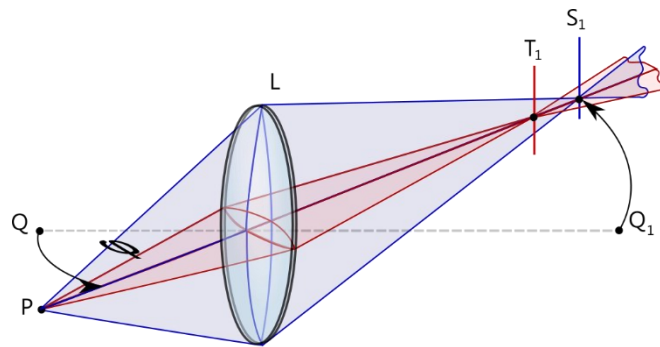


Figure 2.5: Graphic illustration of astigmatism. The rays in sagittal and meridional planes have different foci at S_1 and T_1 respectively. [35].

2.2.1.4 Field curvature

Field curvature is also known as Petzval field curvature (named after Joseph Petzval [1807–1891]). This aberration results in a planar object normal to the optical axis being projected as a curved nonplanar image (Figure 2.6). It is caused by the lens having a smaller effective diameter and higher effective power to the rays coming from an off-axis points.

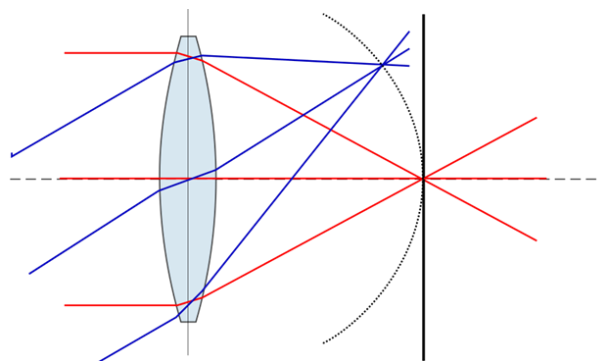


Figure 2.6: Field curvature. The object points are not imaged onto a flat image plane [36].

2.2.1.5 Distortion

Distortion is the deviation of the lens or lens system from a rectilinear projection, which means straight lines in the object are not straight lines in the image. Distortion can be irregular or it may follow some pattern. Two most commonly occurring radially-symmetric distortions are shown in Figure 2.7. Distortion occurs when the linear magnification is a function of the off-axis distance, resulting in the object points far from the optical axis getting more (pin-cushion) or less (barrel) magnified compared to object points on the axis. Distortion can be minimized by using symmetric doublets such as an orthoscopic doublet

[37] and eyepieces such as a Ramsden eyepiece [38]. However, fisheye lenses utilize the barrel distortion as a way to map an infinitely wide object plane onto a finite image area.

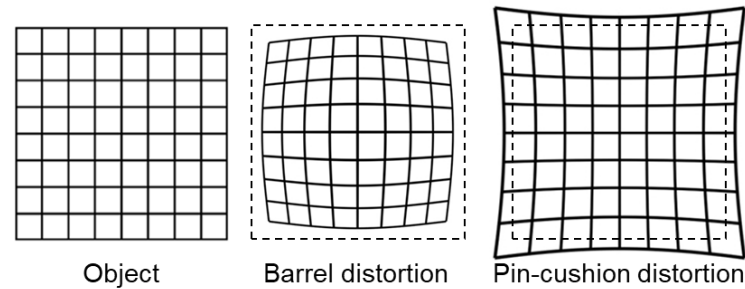


Figure 2.7: Distortion of the image. The dashed squares represent the undistorted rectilinear image [39].

2.2.2 Chromatic aberrations

Chromatic aberrations are generated due to the dispersion of light. The speed of light, and hence the refractive index of the optical material, varies with the wavelength. Therefore, each wavelength is refracted differently by the optical elements, and the lens cannot focus all the wavelengths at a single point to produce a sharp image. These aberrations are further classified in two types: Longitudinal and lateral chromatic aberration (Figure 2.8).

Longitudinal chromatic aberration occurs when different wavelengths are focused at different points along the optical axis. These are typical for lenses with longer focal lengths. Lateral chromatic aberrations occur when different wavelengths coming from off-axis point focus at different points in the focal plane due to the fact that magnification and distortion of the lens are also wavelength-dependent. These aberrations have different characteristics but may exist together.

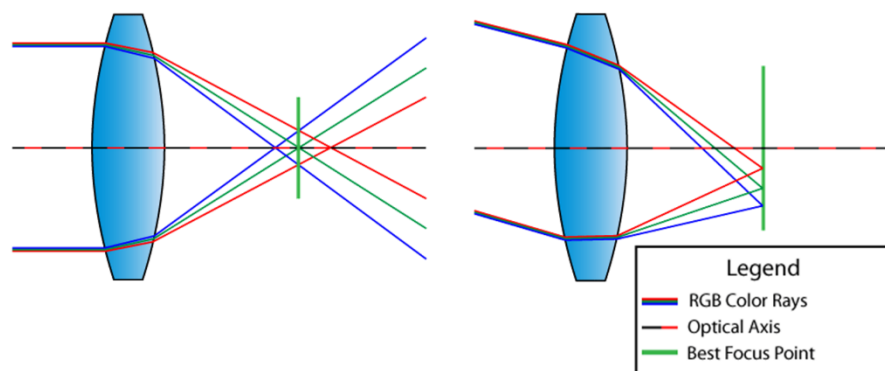


Figure 2.8: Left: Longitudinal chromatic aberration. Right: Lateral chromatic aberration [40].

Chromatic aberrations can be reduced, in addition to reducing aperture, by combining lenses from materials with different dispersion in achromatic doublets or even “apochromatic” triplets, and or by diffractive optical elements. Two examples where the chromatic aberrations are reduced by a diffractive optical element and an achromatic doublet are shown in Figure 2.9.

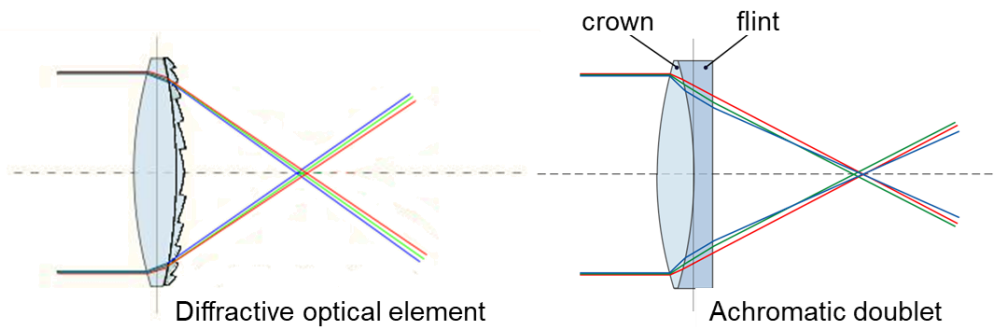


Figure 2.9: Diffractive optical element and achromatic doublet to minimize chromatic aberrations [41, 42].

2.3 Resolution measurement

The resolution of an imaging system, also known as optical resolution, describes the ability of the imaging system to distinguish the details in the object being imaged. Modulation is the process of varying one or more properties of a periodic waveform. In order to measure the resolution of an imaging system, modulated waveforms with varying spatial frequency are imaged, and the images are processed to quantify the resolution of the imaging system. One common method is to image a series of alternating black and white bars (i.e., 1951 USAF target or Ronchi ruling) representing square waves with varying spatial frequency (usually expressed as line pairs/mm) to quantify the contrast from the captured images.

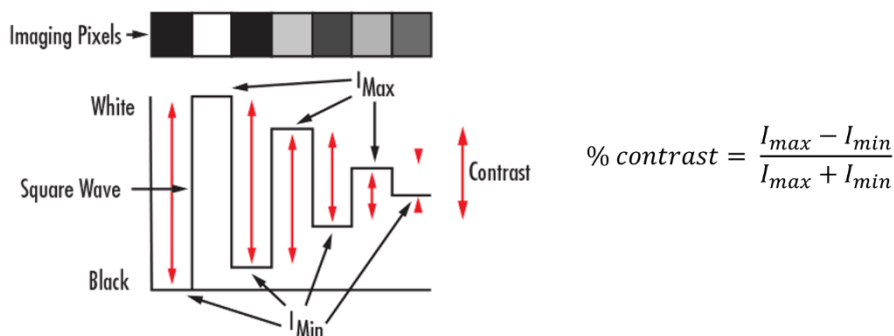


Figure 2.10: Graphical and mathematical description of contrast [43].

Figure 2.10 describes the contrast graphically and mathematically and shows the contrast depreciation of a square wave consisting of alternating black and white bars. The first line pair is ‘perfectly’ black and white, with the black bar having the minimum intensity of 0 and the white bar the maximum of 1. This corresponds to a contrast value of 1 (or 100 %) according to the equation in Figure 2.10. Each of the subsequent bars are grey such that the supposedly black bars are brighter (intensity increasing) and white bars darker (intensity decreasing), and the contrast of the line pairs decreases.

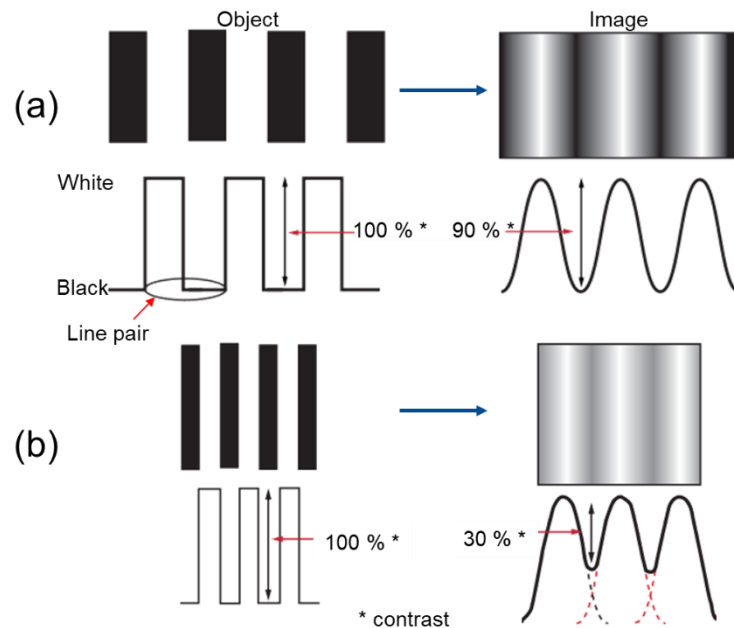


Figure 2.11: Contrast comparison of image at different spatial frequencies [43].

Figure 2.11 shows the response of a typical imaging system when used to image pairs of black and white bars with two different spatial frequencies. Figure 2.11a shows the image of a bar target with low spatial frequency. The image has blurred edges and has 90 % contrast transferred at this spatial frequency. Figure 2.11b shows the response of the same imaging system when used to image a bar target with high spatial frequency. The edges in the image are merged into each other and are hardly recognizable. Only 30 % contrast is transferred by the imaging system at this spatial frequency.

The modulation transfer function of an imaging system quantifies the contrast transfer over a range of spatial frequencies. It is the modulus of the optical transfer function (OTF), which is the Fourier transform of the impulse response of the system. The MTF of a system is simply obtained by multiplying the MTFs of all individual components.

The MTF of an imaging system can be determined mathematically in different ways, two of them are described here: diffraction-limited and pixel-limited MTF. The

diffraction-limited MTF is based on the wave-optic calculations and provides the upper limit to the performance of any optical system. It depends on the aperture size (and shape), wavelength of the light, and focal length of the imaging system [44]. The diffraction-limited MTF is calculated by Eq 2.3 and Eq 2.4 for a square and circular aperture respectively [44].

$$\text{For a square aperture } MTF_{diff} = 1 - \frac{\xi}{\xi_c} \quad Eq\ 2.3$$

$$\text{For a circular aperture } MTF_{diff} = \frac{2}{\pi} \left\{ \cos^{-1} \left(\frac{\xi}{\xi_c} \right) - \left(\frac{\xi}{\xi_c} \right) \left[1 - \left(\frac{\xi}{\xi_c} \right)^2 \right]^{\frac{1}{2}} \right\} \quad Eq\ 2.4$$

where

ξ	Spatial frequency [lp/mm]
ξ_c	Cut off frequency [lp/mm] = $\frac{1}{\lambda \cdot f/\#}$
λ	Wavelength of light [mm]
$f/\#$	f-number of the objective

Pixel-limited MTF, also called theoretical MTF of an imaging system, is based on the pixel size of the detector, and is calculated by Eq 2.5 [44]. Eq 2.5 implies that the performance of an imaging system with a detector will improve at a particular non-zero spatial frequency with a decrease in pixel size, i.e. a 10 times smaller pixel size will result in 10 times better performance at a given spatial frequency and so on.

$$MTF_{th} = |\text{sinc}(\xi w)| \quad Eq\ 2.5$$

where

ξ	Spatial frequency [lp/mm]
w	Pixel width [mm]

Figure 2.12 shows the difference between diffraction-limited MTF based on the hybrid relay element of the UV endoscope system and incident light at 325 nm, and theoretical MTF based on a detector having square pixels of $10\ \mu\text{m} \times 10\ \mu\text{m}$. The plot shows that the diffraction-limited MTF is far superior to the theoretical MTF and is hardly degraded over the range shown in Figure 2.12. The cut-off frequency for the diffraction-limited MTF (the spatial frequency where the MTF of the system would become zero) is 1.54×10^6 lp/mm. On the other hand, the theoretical MTF has dropped to zero at 100 lp/mm. The successive rise in the pixel-limited MTF after the spatial frequency of 100 lp/mm are mathematical, and have no physical meaning, i.e., the transferred contrast does not increase with the increasing spatial frequency once it is dropped to zero.

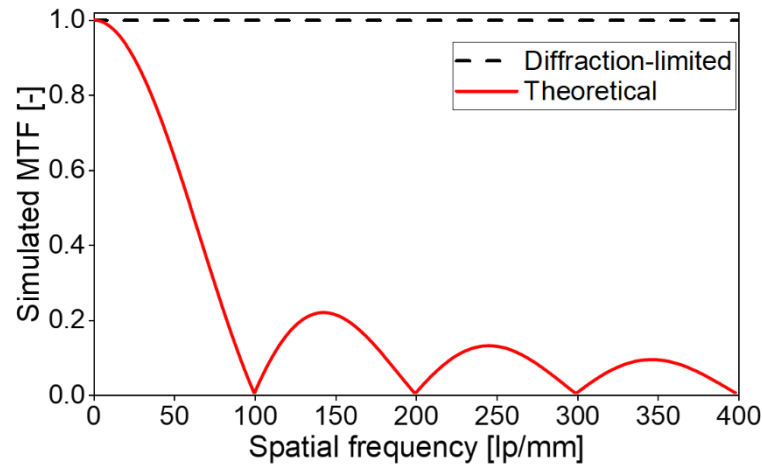


Figure 2.12: Comparison of diffraction-limited MTF based on hybrid relay element ($f/2$) and light at 325 nm, and theoretical MTF based on a detector with the pixel size of $10 \mu\text{m} \times 10 \mu\text{m}$.

The MTF of a real imaging system is measured by experiments on test benches and specialized equipment utilized by camera manufacturers. One of the methods to measure the MTF is slanted-edge method. The slanted-edge method is a simple way to determine the MTF of an imaging system. It is specified by ISO: 12233 [6]. This method involves imaging a back-illuminated, slightly tilted edge onto a detector. The MTF is then determined in three basic steps: evaluating the edge-spread function (ESF) from the image, the line-spread function (LSF) by taking the first derivative of ESF, and finally computing the MTF as the modulus of discrete Fourier transformation of the LSF. To determine the ESF, first the gradient of the edge from a smaller region of interest (ROI) is determined. The pixels in the ROI are then projected along the estimated edge direction onto a horizontal axis, and then resampled at typically one-quarter of the pixel pitch.

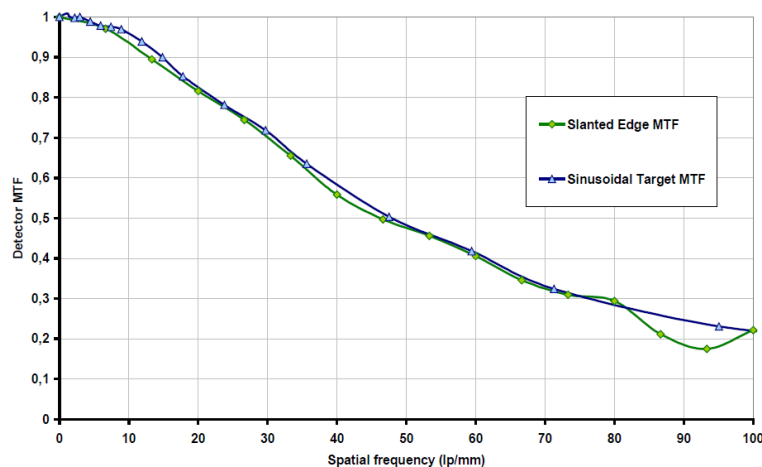


Figure 2.13: Typical MTF plots obtained from sine target method and slanted-edge method [45].

Figure 2.13 shows two typical MTF plots measured experimentally [45]. The results show that the system transferred 50 % contrast at $\sim 46\text{--}47$ lp/mm and a little above 20 % contrast at 100 lp/mm. MTF plots are typically normalized to unity at zero spatial frequency, which might have some implications while comparing the MTF of different imaging systems.

3 Endoscopic imaging in combustion engines

3.1 Imaging with conventional endoscopes

Endoscopic optical diagnostics can be applied in all-metal engines, which provide similar heat transfer and operating range as commercial engines. However, the light collection efficiency is often poor and the spectral range is usually limited to the visible. Therefore, early works concentrated on relatively bright events in the visible spectral region. Some examples are visualization of broadband combustion in diesel [46-49] and gasoline [25] engines, temporally resolved soot pyrometry [48, 50, 51], visualization of the spray via Mie scattering [52-54], and particle image velocimetry (PIV) [26]. However, visualizing the flame luminosity in premixed combustion was more difficult [55, 56]. Richter et al. [57] used a conventional endoscope to image LIF from 3-pentanone in an engine and found the collection efficiency to be 30 times worse than that of the widely available UV-Nikkor $f/4.5$ lens.

To enable a wider range of optical diagnostics in engines with endoscopic access, in previous work at the Institute for Combustion and Gas Dynamics (IVG), University of Duisburg-Essen and collaborating partners, a large-aperture hybrid UV-transparent endoscope system was developed [2, 3] in the projects "Micro-optical systems for diagnostics and processing in cavities" and "Minimally Invasive Engine Diagnostics", both funded by the German Federal Ministry of Education and Research and the State Foundation (Landesstiftung) Baden-Württemberg. The design and development of optical components were performed at Institute of Applied Optics (ITO), University of Stuttgart, in cooperation with Institute of Physical Chemistry (PCI), University of Heidelberg and IVG. The engine application was executed at the IVG. The endoscope system was originally built to replace standard visible-light endoscopes into a cylinder-wall-socket used by Volkswagen, restricting the diameter of the front endoscope to 10 mm [3]. This endoscope is now commercially available from LaVision. This two-component modular refractive-diffractive system is specifically tailored to engine applications and has about the same collection efficiency as an $f/4.5$ UV lens with spatial resolution well-suited for typical image-intensified cameras. This chapter summarizes the requirements and optical

design of the hybrid UV endoscope system. Previous demonstration and in-cylinder experimentations involving the hybrid UV endoscope system are also reviewed in section 3.4.

3.2 Hybrid UV endoscope system

The hybrid UV endoscope system consists of two parts: a front endoscope projecting a real intermediate image onto its back field lens, and a refractive/diffractive hybrid relay lens projecting the intermediate image onto the sensor, as shown in Figure 3.1. The images of the front endoscope and the hybrid relay lens are also included. The front endoscope is mounted in the cylinder head of the engine and is protected from the engine environment by a sapphire window press-fit into a titanium housing (see Figure 3.1 inset). The front endoscope and the relay lens, the latter mounted on the sensor, are not rigidly connected, therefore making the imaging system isolated from engine vibrations. The distance between the front endoscope and hybrid relay lens is around 20 cm, so the optical components such as beam splitters and filters can be placed in between. Commercial detection endoscopes have rigid connections between engine and imaging system, which transmits the engine vibration to imaging devices. Also, they are mostly designed for visible spectral range and accumulate chromatic aberrations due to series of image relays.

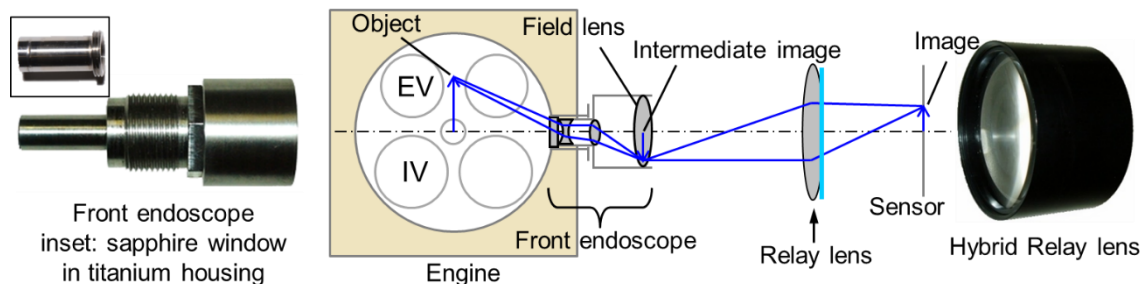


Figure 3.1: Two-component hybrid UV endoscope system. EV and IV are exhaust and intake valves respectively [5].

3.2.1 Optical design of the hybrid UV endoscope system

The design of UV imaging optics is challenging because there are very few possibilities for lens materials. In the hybrid UV endoscope system, apart from a pressure-sealing front window from sapphire, all the optical elements are made from fused silica (FS). FS makes the front endoscope transparent in UV, VIS, and IR, while the hybrid relay element is

limited to a certain range of wavelengths depending on its diffractive component. The specifications of the endoscope system are given in Table 3.1.

Table 3.1: Design specifications of the hybrid UV endoscope system [3, 4]

Front diameter	10 mm (12 mm with titanium housing)
Field of view	30 × 30 mm
Working distance	35 mm
Detector size	Ø 25 mm (photocathode of ICCD)
Paraxial magnification	0.5
Resolution	Better than 100 × 100 pixels
Correction range of the hybrid relay lens	275–350 nm (for toluene LIF) 380–440 nm (for pentanone LIF)
Focal length of the hybrid relay lens	~90 mm
Aperture	50 mm
Lens speed	~ $f/1.8$

The front endoscope consists of three refractive lenses that generate considerable spherical and chromatic aberrations. Figure 3.2 shows outputs from the Zemax model of the front endoscope and the optical aberrations assigned to the lens surfaces.

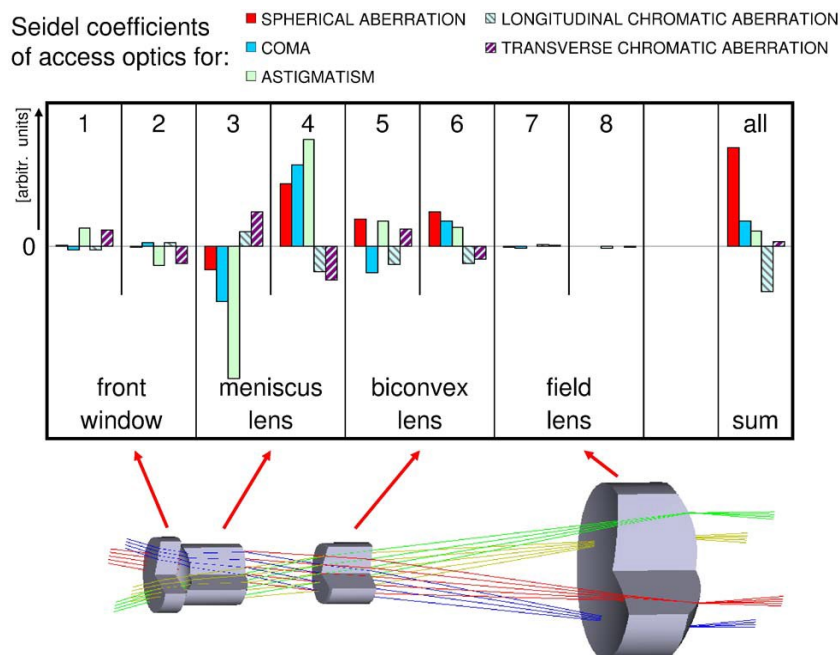


Figure 3.2: Seidel aberration coefficients for different surfaces in the front endoscope [2].

Some of these aberrations are effectively corrected within the front endoscope, e.g., astigmatism and coma. The two surfaces of the first meniscus lens produce considerable, but opposite, amount of these two aberrations resulting in relatively low residual aberrations. Spherical and longitudinal chromatic aberrations are tolerated in the front endoscope and corrected by the hybrid relay lens. Strong barrel distortion is also produced in the front endoscope (see Figure 3.3), but can be corrected in post-processing [17, 58].



Figure 3.3: Image of a target on the field lens of the front endoscope showing wide angle detection and barrel distortion of front endoscope.

The hybrid relay lens is a simple construction consisting of a refractive ‘focusing’ element and a diffractive ‘correcting’ optical element (DOE) as shown in Figure 3.4. This whole hybrid relay lens is abbreviated as DOE in this work, as in most previous works where this system has been used.

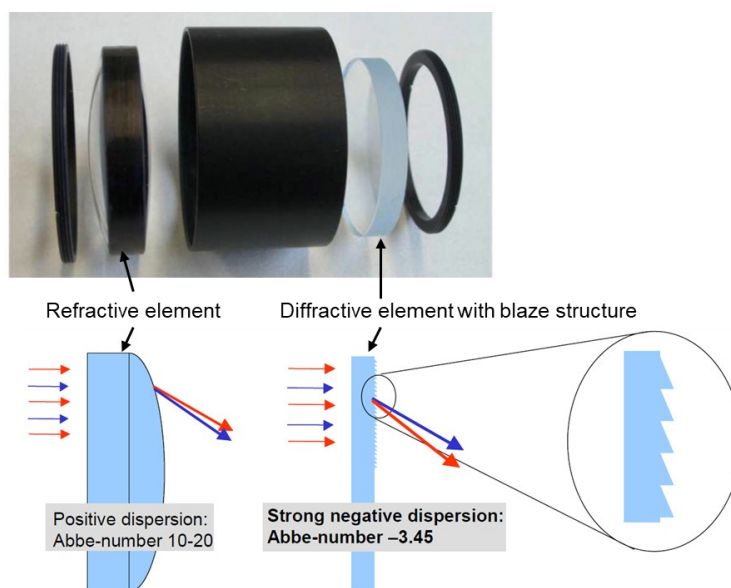


Figure 3.4: Above: Hybrid relay element exploded view [2]. Below: Schematics of refractive and diffractive elements [3].

Figure 3.4 shows that chromatic correction in the diffractive element is achieved by strong negative dispersion shown by a negative Abbe number. The higher orders of diffraction are reduced by optimized phase-modulation of the blaze structure on the DOE for a certain wavelength range (about 60 – 75 nm) and its relative position to the refractive lens in the relay [2].

Figure 3.5 shows that the RMS wavefront error for a centrally placed object has two minima and relatively low error within its design range, here 275–350 nm for toluene LIF. Outside the design range, the error increases significantly [2].

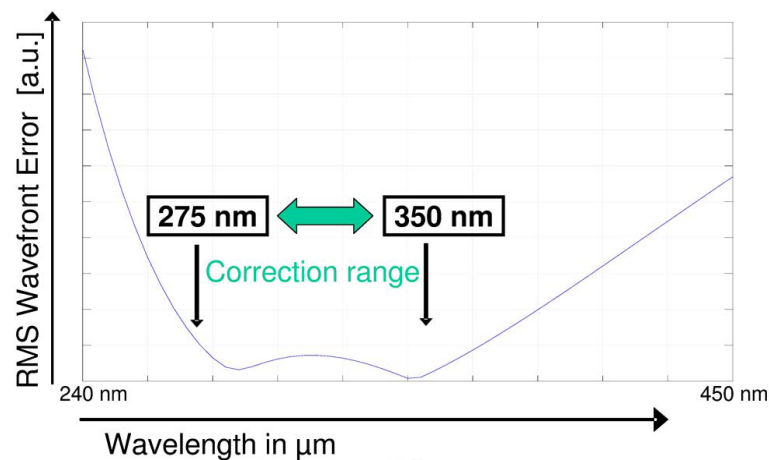


Figure 3.5: Chromatic correction for 275–350 nm DOE demonstrated by the RMS wavefront error versus the wavelength [2].

3.3 Illumination endoscopes

3.3.1 Sheet illumination endoscope

To illuminate the cylinder endoscopically for laser-based diagnostics, illumination endoscopes with an outer diameter of 9 mm were developed in previous work [3, 59]. The first endoscope converts an incoming laser beam into a 0.5 mm thick, laterally divergent light sheet, the second into an inhomogeneous 5-point illumination for flow tagging experiments. Figure 3.6 demonstrate the size of illumination endoscopes compared to a typical pen, the exit slit for the thin laser sheet, and the inside view of the micro-optics for sheet illumination endoscope.



Figure 3.6: Images of illumination endoscope (a) Size compared to a pen (b) the exit slit (c) inside view of the internal optics and spacer tubes for sheet illumination endoscope [3].

The micro-optics are cut in $4.95 \times 4.95 \text{ mm}^2$ square cross-section to avoid rotation and are placed into a tube with a square hole and a near-tight fit. The distance between lenses is controlled by precision tubes held in place by a loaded spring at the back (not shown here). The micro optics in the illumination endoscope are protected from the harsh engine environment by a 3 mm thick sapphire window sealed in the endoscope housing by copper washers (not shown here) [60]. The fused silica window offers a higher transmission ($>95 \%$) for 266 nm laser compared to sapphire ($\sim 70 \%$), but it is not strong enough and prone to break mid-experiment.

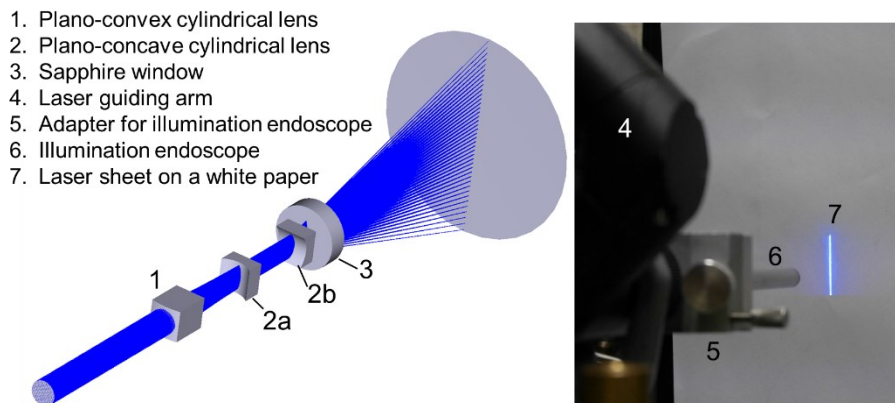


Figure 3.7: Left: Zemax simulation of the homogeneous light sheet illumination endoscope. Right: Image of laser sheet on a white paper.

Figure 3.7 shows a Zemax simulation of a $\text{Ø} 4 \text{ mm}$ laser beam transformed into a divergent laser sheet and an image of the laser sheet on a white paper. The laser is converted into a thin sheet by two cylindrical lenses (1 and 2a) acting as a telescope, while the next lens (2b) diverge this thin sheet with a 44° opening angle [3]. The lenses are cut from anti-reflective coated (245–400 nm) commercial lenses from Thorlabs: 1 from plano-convex cylindrical lens (LJ4305-UV) [61], 2a and 2b from plano-concave cylindrical lens (LK4351-UV) [62].

The drawings of the lenses cut from the source lens are given in the appendices App 1 and App 2. The lens 2b and the sapphire window (3) were found the elements most likely to be damaged due to high energy density of the laser beam.

3.3.1.1 Modification in sheet illumination endoscope

In this work, the micro-optics in the sheet illumination endoscope were modified to illuminate the area directly below the pent roof, which could not be illuminated in earlier works (Figure 3.8). This was achieved by cutting a $4.95 \times 4.95 \text{ mm}^2$ square lens (2b from Figure 3.7) off center by a maximum possible offset of 0.755 mm (see App 3 for detailed drawing). The upward steering of the light sheet by off-center cutting of the diverging plano-concave lens is shown in Figure 3.8 as both simulation and images from the engine.

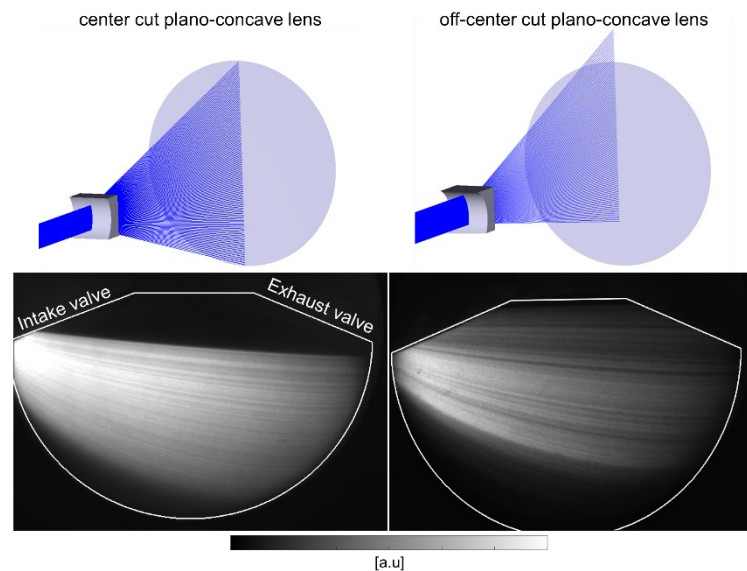


Figure 3.8: Upward steering of the light sheet by off-center cutting of the diverging plano-concave lens. Above: Zemax simulation. Below: Fluorescence images from the endoscopic engine showing the illuminated area.

3.3.2 Inhomogeneous illumination endoscope

Figure 3.9 shows the simulation and image of the illumination pattern of the inhomogeneous illumination endoscope. It was designed for flow tagging applications and included a diffractive element containing 5 diffractive micro lenses. Each micro lens creates a convergent beam with a diameter of $\sim 0.5 \text{ mm}$, and the bundle of beams was diverged by the same plano-concave lens used in the endoscope for uniform illumination [3]. This endoscope was used in calibration experiments for two-color anisole-LIF thermometry (see

section 5.4.2) and is addressed here as “point illumination endoscope”, or simply “point endoscope”.

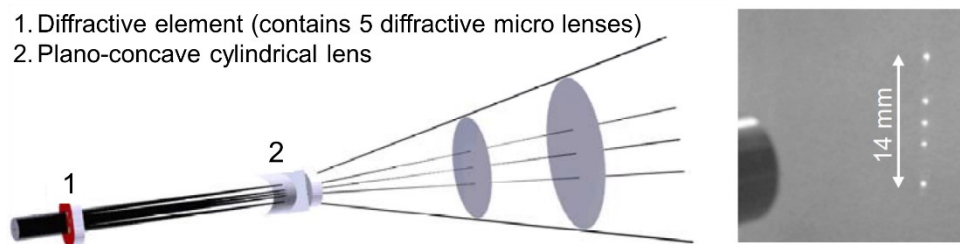


Figure 3.9: Left: Simulation of the of the endoscope for inhomogeneous illumination. Right: Illumination pattern on a white paper [3]

3.3.3 Flood illumination endoscope

To illuminate the liquid fuel films on the piston surface (Chapter 6), a simple flood illumination endoscope was designed in this work. This was done by replacing all the lenses in a commercial UV illumination endoscope from LaVision by a single commercially available anti-reflective coated (245–400 nm) bi-concave lens from Thorlabs (LD4797-UV) [63]. The illumination pattern and the area of piston surface illuminated close to TDC are shown in Figure 3.10. Note that the illuminated part of the piston surface depends on the crank angle, with areas closer to the endoscope progressively getting darker when the piston descends.

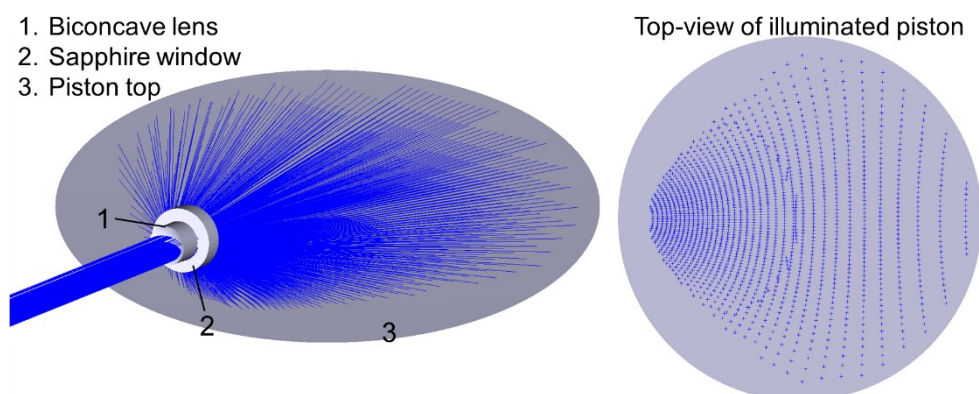


Figure 3.10: Flood laser illumination. Left: Illumination pattern. Right: Illuminated piston surface at crank angles close to TDC.

3.4 Review of previous work with the hybrid UV endoscope system

3.4.1 Bench-top demonstration experiments

In bench-top demonstration experiments, the hybrid UV endoscope was compared with a commercial UV endoscope (LaVision) and a commercial Nikkor UV lens (focal length =105 mm, $f/4.5$) [3, 59]. LIF of a turbulent nitrogen flow seeded with toluene was imaged using two of the three systems at a time. Figure 3.11 shows the key results from the demonstration experiment. The hybrid UV endoscope system collects about 1.3 times more light than the Nikkor UV lens in the center, with lower collection in the upper and lower region due to vignetting. A corona of diffuse light is visible around the edges of jet in both images but is less intense in the image taken with Nikkor. This effect is due to scattering on the diffractive surface of the DOE. Additional background signal resulted from the higher order diffraction which are not corrected in the DOE. The resolution of the image taken by the hybrid UV endoscope system was slightly inferior, but still remarkably good given the fact that the comparison is with a standard UV lens. In comparison to the commercial UV endoscope, the hybrid UV endoscope showed good resolution and about 7 times higher light collection (see Figure 3.11).

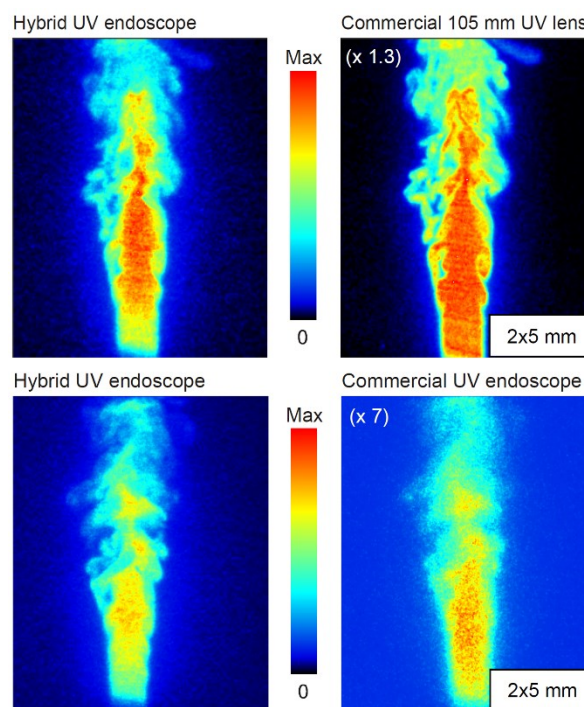


Figure 3.11: Comparison of toluene-LIF images of a turbulent flow. Above: Hybrid UV endoscope system vs. commercial Nikkor UV lens. Below: Hybrid UV endoscope system vs. commercial LaVision UV endoscope [3].

In another similar experiment, the oxygen concentration in a nitrogen flow seeded with toluene and 3-pentanone was measured by simultaneously imaging LIF of toluene and of n-pentanone by two cameras [3, 59], taking advantage of the different effect of fluorescence quenching on both tracers. Results from two experiments are shown in Figure 3.12. Top row shows the increasing oxygen concentration downstream due to mixing with surrounding air in the absence of a coflow. The bottom row shows a uniform 0 % (blue is the lower limit of color scale, black is masked region) oxygen concentration. This can be regarded as a metric for the accuracy of the measurement since the pixel values in resulted oxygen concentration image had the expected value of 1 with less than 5 % variation. The images were corrected for distortion, and not for vignetting, which show that for ratiometric measurements, the correction for vignetting is not required.

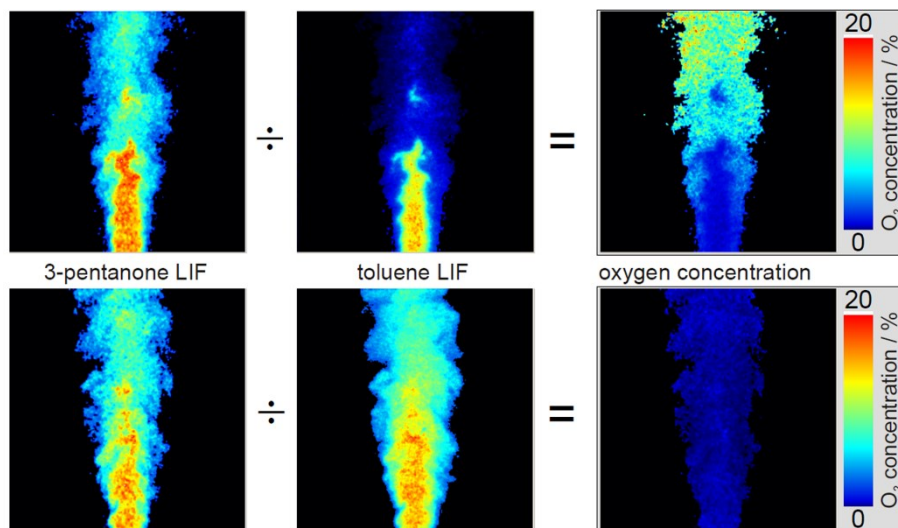


Figure 3.12: Measurement of oxygen concentration in a nitrogen flow. Top: Seeded nitrogen flow mixing with surrounding air. Bottom: Seeded nitrogen flow mixing with fast nitrogen coflow [3].

In another experiment, the inhomogeneous illumination endoscope (see section 3.3.2) was used to determine axial flow velocities by flow tagging [3, 59]. Toluene-sensitized phosphorescence of biacetyl was used to measure flow velocities, because it yields stronger signal than the direct excitation of biacetyl at 266 nm, and the phosphorescence lifetime of biacetyl is reported to be as long as 1.5 ms in the absence of oxygen [64].

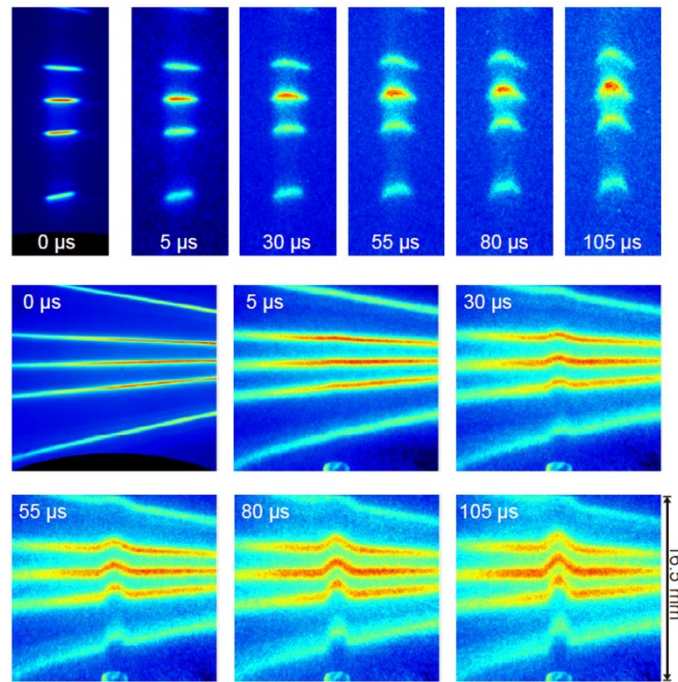


Figure 3.13: Average line-tagging images at different times after excitation. Top: Only flow seeded; bottom: Flow and co-flow seeded with tracer [3].

Figure 3.13 shows the results of the flow-tagging experiments. In images on the top, only the flow was seeded with tracer (toluene and biacetyl), and in the lower image both the flow and coflow were seeded with tracer. The first image at 0 μs is of toluene LIF. The images at later times are of the phosphorescence of toluene-sensitized biacetyl and show that the axial velocities are higher at the core of the jet compared to the velocities at edges. The measured axial velocities from these flow-tagging images agreed very well with the simulations for slow flow velocities and smaller time delays [3]. The biacetyl phosphorescence signal peaks around 520 nm [65]. The hybrid relay element used in this experiment were optimized for a spectral region from 380–440 nm, but still yielded sufficiently sharp images.

3.4.2 OH* and broadband chemiluminescence imaging

The OH*-chemiluminescence has peak emission intensity from 306–315 nm (see Table 2.2), which lies within the correction wavelength range of the DOE designed for toluene LIF, 275–350 nm (see Table 3.1).

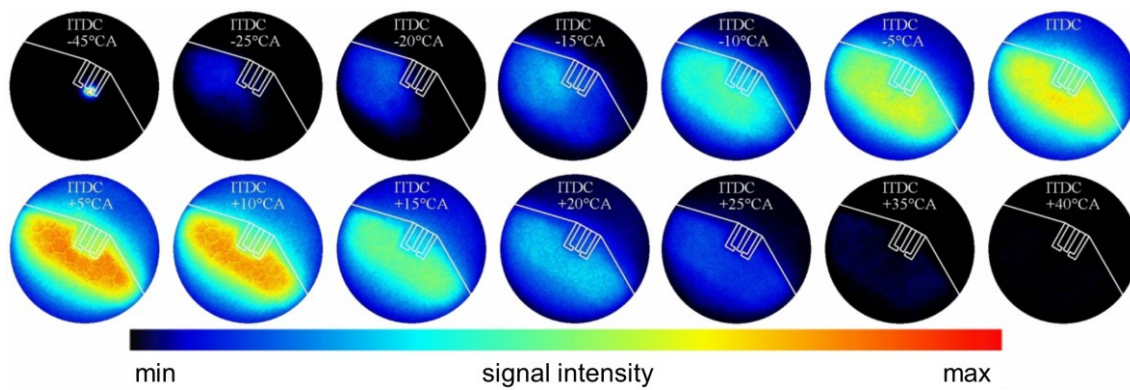


Figure 3.14: Ensemble-average mean images of OH^* -chemiluminescence at different crank angles at a low-load operating point [4].

Initial OH^* -chemiluminescence imaging in an all-metal endoscopic engine using the hybrid UV endoscope system is reported in [4, 59], and are summarized here. Figure 3.14 shows the ensemble-averaged mean images of OH^* -chemiluminescence taken in low-load operation in the production engine described in more detail in Section 5.2 and in [4, 58, 60]. The images were taken at different crank angles, ranging from -45°CA to $+40^\circ\text{CA}$. At -45°CA the spark is visible, followed by an overall developing flame. The signal intensity also increases with the development of flame until $+10^\circ\text{CA}$, after which the intensity decreases gradually and vanishes completely at $+40^\circ\text{CA}$. At crank angles close to the TDC, the flame is observed outside the limits of the combustion chamber (marked by white lines). This happened due to off-center detection of flame luminosity, which increased the apparent size of the flame. The images at low-load operating conditions show that the hybrid endoscope system has good light collection efficiency and can detect the weak chemiluminescence signals at such loads. The high light collection efficiency also allows for capturing single-shot OH^* -chemiluminescence images as shown in Figure 3.15. This can be used for investigation of cycle-to-cycle variation in the flame propagation.

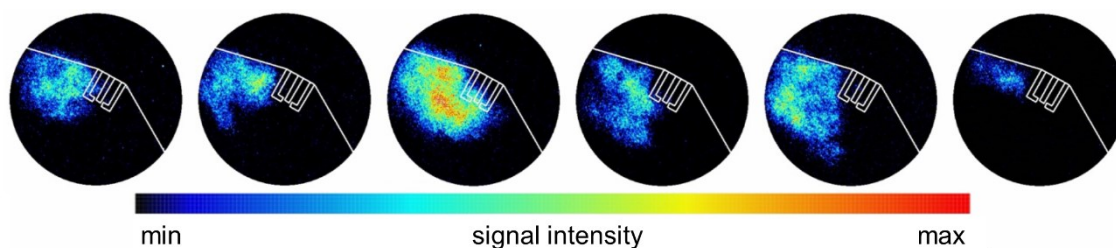


Figure 3.15: Single-shot images of OH^* -chemiluminescence at a low-load operating point in the endoscopic engine. Images were taken at 20°CA bTDC [4].

Since imaging OH*-chemiluminescence was indeed possible with the hybrid UV endoscope system, Goschütz imaged OH*-chemiluminescence at different conditions and with three different camera systems [5, 17]. Figure 3.16 shows OH*-chemiluminescence images from the same all-metal engine from which the images shown in Figure 3.14 and Figure 3.15 were taken. Figure 3.16 shows how the flame size and the intensity of the OH*-chemiluminescence increase with the load.

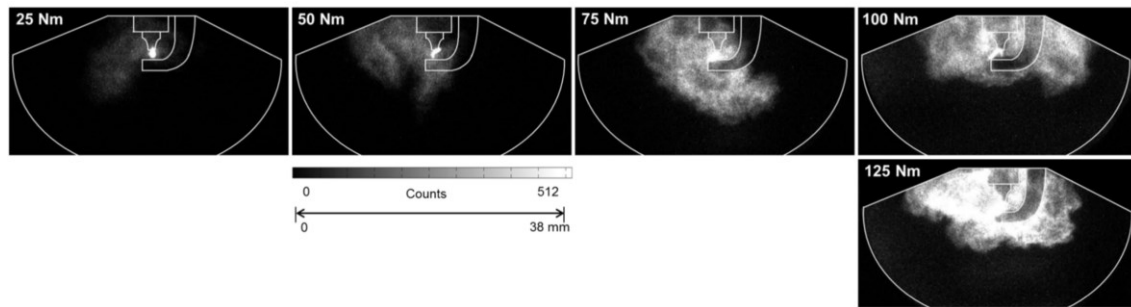


Figure 3.16: OH*-chemiluminescence images at 14°CA after ignition timing (aIT) at different engine loads ($n = 2000 \text{ min}^{-1}$) [17].

The apparent flame area was determined from the images shown in Figure 3.16 by image segmentation [17]. Figure 3.17a shows the cylinder pressure plotted against the apparent flame area at one operating point. In general, the width of the spread in pressure is a magnitude smaller than the spread of the apparent flame area [17].

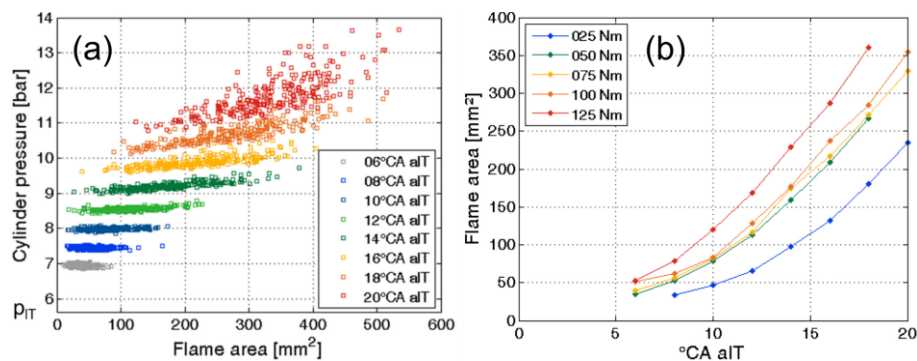


Figure 3.17: (a): Correlation between the apparent flame area and cylinder pressure at one operating point ($n = 2000 \text{ min}^{-1}$, $M = 75 \text{ Nm}$). (b) Ensemble-average apparent flame area at different engine loads ($n = 2000 \text{ min}^{-1}$) [17].

The results shows that the cylinder pressure is a much less sensitive indicator for the cycle-to-cycle variability in the early stages of flame development [17]. Figure 3.17b that the average apparent flame area increases more than linearly with time, which was expected even for a constant flame speed since the apparent flame area scales with the square of the

flame radius in first approximation. The results are also consistent with Figure 3.16, which shows that at higher loads the flame growth rates tend to be faster.

Figure 3.18 shows a high-speed imaging sequence of OH^* -chemiluminescence [5, 17]. The images clearly have less contrast and resolution than those taken as snapshots by the ICCD camera as shown in Figure 3.16. But this high-speed imaging gave insight beyond phase-locked imaging. E.g., it was observed that the delay between spark initialization and the onset of flame was different in different cycles, and that the flames keep their shape while growing [17]. Determination of the apparent flame area was relatively difficult in the high-speed images in the early stages of flame propagation due to low contrast.

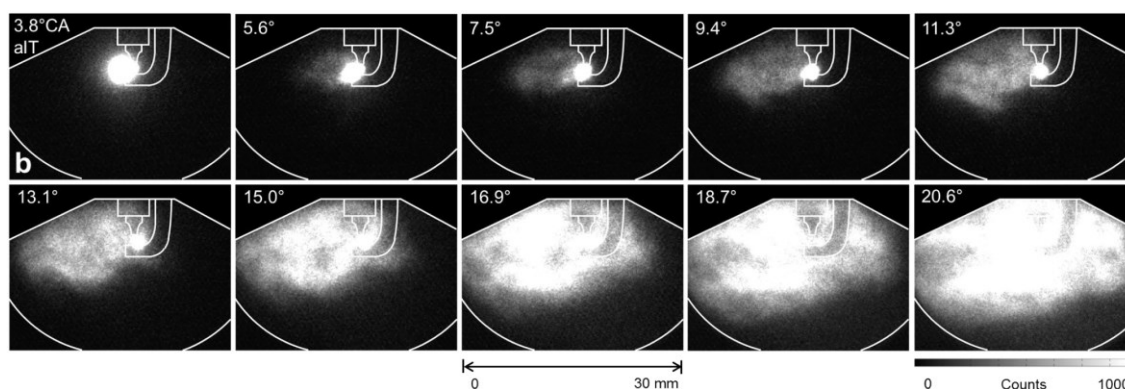


Figure 3.18: High-speed imaging sequence of OH^* -chemiluminescence
($n = 2090 \text{ min}^{-1}$, $M = 75 \text{ Nm}$) [17].

In a phase-locked double frame imaging two OH^* -chemiluminescence images were taken with an inter-frame delay of $2\text{--}4^\circ\text{CA}$ depending on the engine speed [5, 17]. Figure 3.19 shows one typical image captured at the engine speed of 2000 min^{-1} and engine torque of 125 Nm , and development of equivalent flame radius and apparent flame speed with the crank angle. The inter-frame delay was 2°CA . The images were first filtered with a non-linear diffusion filter [66], binarized, and dewarped. The flame boundaries were then extracted from the binarized images which, when plotted together, showed how much the flame had propagated during the inter-frame delay. The equivalent flame radii were calculated from the apparent flame areas in the first frame, assuming the flames as circles [17]. Figure 3.19b shows that for the first few crank angles there is some flame acceleration, then the equivalent flame radius increases nearly linearly. Figure 3.19c shows that the apparent flame speed, based on equivalent flame radii and inter-frame delay, increases until about 12°CA aIT , and then slows down due to interaction with the pent roof.

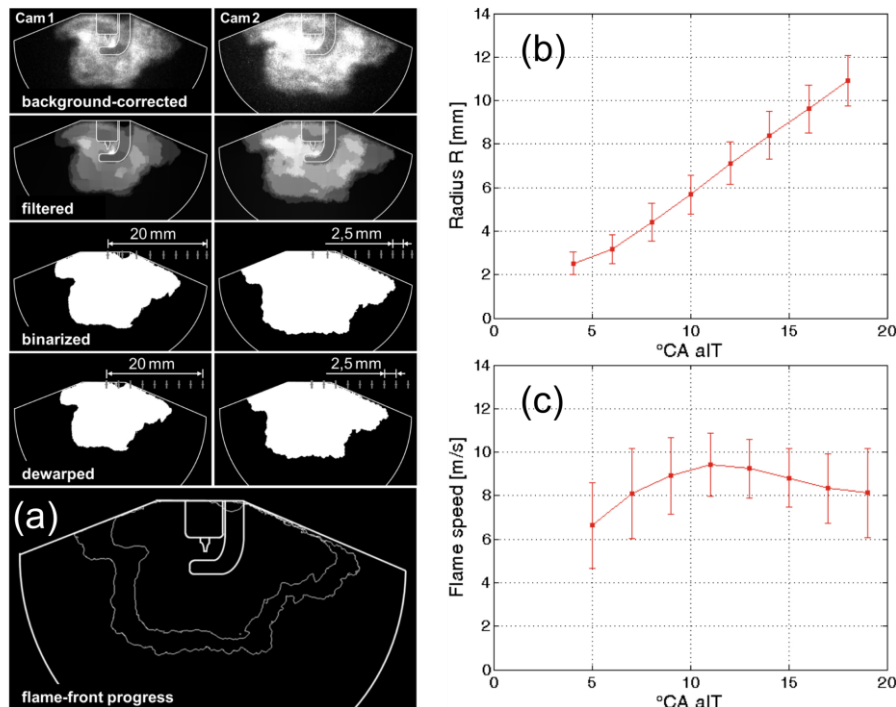


Figure 3.19: (a) Typical post-processing steps for an image pair from double-frame imaging (b) Equivalent flame radius development derived from the images in (a). (c) Apparent flame speed derived from the images in (a). The error bars in the plots represent the standard deviation, indicating the extent of cycle-to-cycle variation [17].

In another work, the image quality achievable with the front endoscope of the hybrid UV endoscope system and high-speed CMOS cameras was investigated by Shawal et al. [15]. The experiments were performed in three different engines, all of them involving imaging the broadband chemiluminescence in the spectral range of 400–800 nm with an unintensified high-speed CMOS camera. Figure 3.20 shows the chemiluminescence images obtained by the three unintensified CMOS camera systems, named HS1, HS, and HS2. HS1 is a high-speed imaging sequence from a 4-cylinder BMW engine. Here, the spark is clearly discernible, as opposed to the images shown in Figure 3.18. The signal intensity of the broadband chemiluminescence of the early flame kernel is closer to the read-out noise of the camera due to absence of an intensifier. The read-out noise has a particular pattern in this camera and is spatially shifting with time. For the best possible noise subtraction, the mean of the last 10 images before the spark in each cycle was subtracted from the images in subsequent cycle.

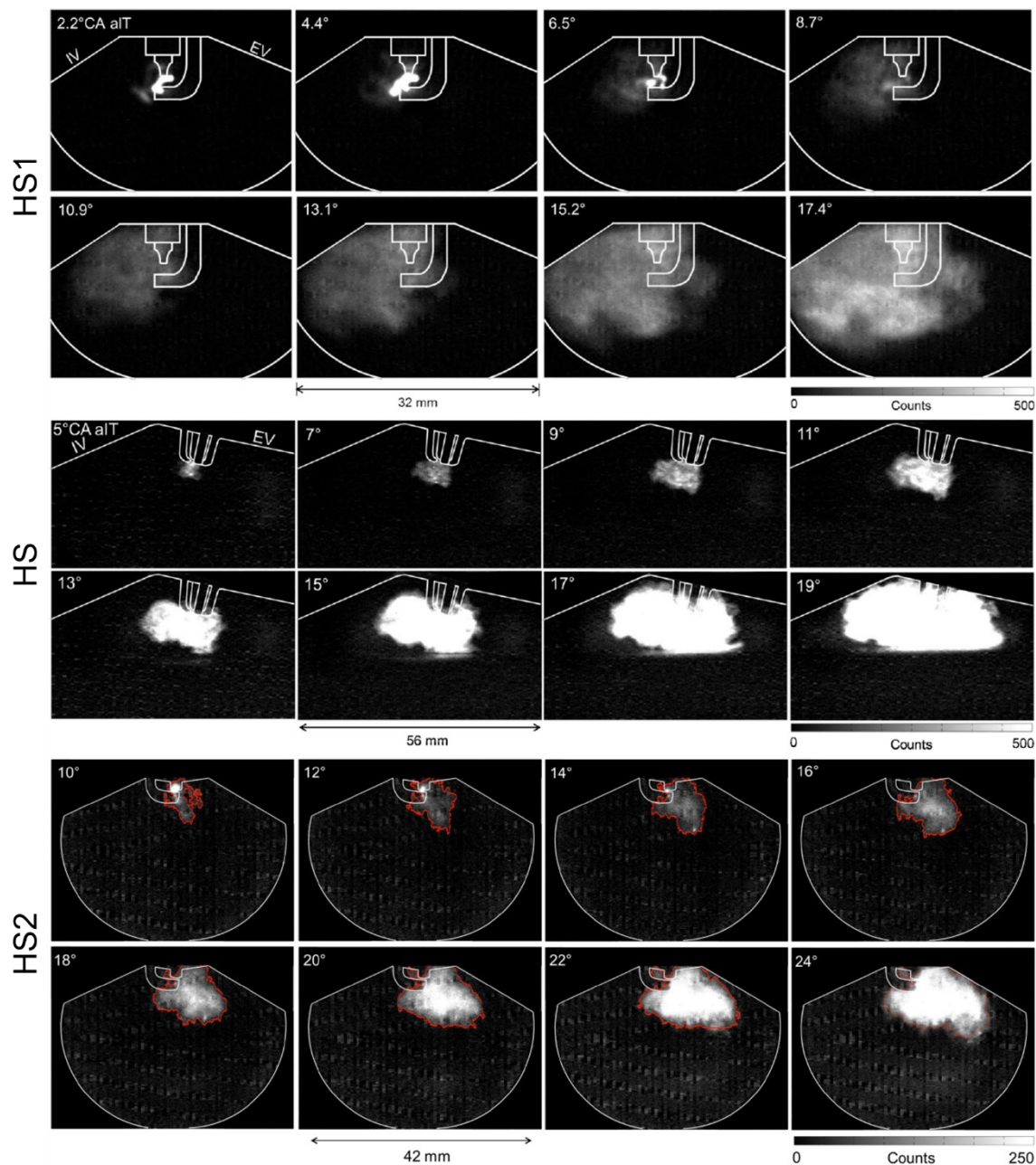


Figure 3.20: High-speed unintensified cinematography in different experiments. HS1: endoscopic cinematography in a 4-cylinder BMW endoscopic engine. HS: cinematography in a single cylinder optical engine. HS2: Endoscopic cinematography in a single cylinder motorcycle endoscopic engine [15].

The image sequence labelled “HS” in Figure 3.20 is from an optical engine with a large optical access. Despite higher frame rate and lower IMEP, the detected signal is twice as high as in HS1, and the image appears sharper. The flame front can be seen reaching the piston top between 13° and 15°CA aIT, and the lower part of luminous area is limited by a horizontal boundary, i.e., piston top. The endoscopic experiments never show such clear lower boundary, even when the flame would have impinged on the piston. This difference

is due to much wider viewing angle of the endoscope, which induces a systematic error of up to 15 % [17] in the burnt-area estimation.

The image sequence “HS2” in Figure 3.20 is from a single cylinder motorcycle engine. The optical setup was similar to that of HS1. The red line in the images represent the flame front as detected by the binarization procedure described in detail by Shawal et al. [15]. The read-out pattern noise was not subtracted in this sequence to give an impression of the noise. In this sequence, the spark was less discernible compared to the HS1 due to the fact that the endoscope was mounted lower in the cylinder head in this case, and the spark was away from the image center of the endoscope, where the resolution is worse. At this position, the vignetting also reduces the image brightness, which is critical for the detection of weak luminosity of early flame kernel.

From the HS2 high-speed sequences, equivalent flame radius was determined by assuming the flame area determined by the binarization procedure to be a circle. This equivalent flame radius was used to determine flame speed, which was then averaged to obtain an average flame speed for one cycle. Figure 3.21 shows the average flame speed plotted against pressure-derived CA5 (crank angle position where 5 % fuel mass is burnt). The result shows that the “optically slower” cycles reach CA5 slower than the faster ones. This is in agreement with the results of Aleiferis et al. [67, 68], and Salazar et al. [69].

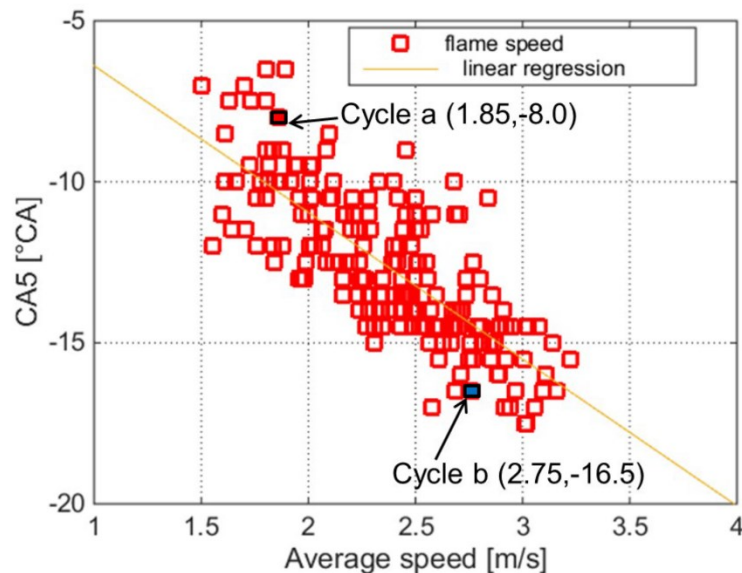


Figure 3.21: CA5 vs. flame speed for all cycles in HS2 [15].

3.4.3 Laser-induced fluorescence imaging

3.4.3.1 LIF imaging of commercial fuel

Commercial fuel consists of various fluorescent species that can be excited via laser and emit broadband fluorescence. The LIF of commercial fuel (RON 95) was visualized during the gas exchange process to detect the inhomogeneities in the fuel distribution [4, 59]. Figure 3.22 shows the fuel-LIF images from different cycles at -355°CA (about 35°CA after opening of the intake valves).

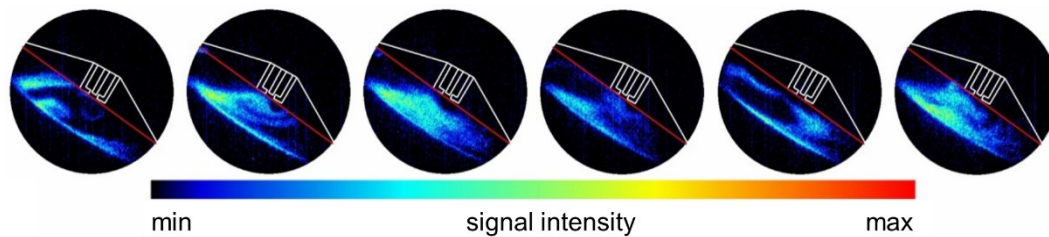


Figure 3.22: snapshots of fuel LIF at -355°CA (5°CA after gas-exchange TDC) [4].

3.4.3.2 Toluene-LIF imaging of fuel distribution

The broadband LIF signals from commercial fuel are typically not used to quantitative measurements because they originate from a large number of species with different physical properties. For this purpose, a mixture of non-fluorescent base fuel and a well-characterized fluorescent “tracer” is used. In a similar setup and operating conditions as mentioned in the section 3.4.3.1 above, LIF from mixture of 85 % isooctane and 15 % toluene was imaged during the gas exchange and compression stroke. Figure 3.23 shows the toluene-LIF images averaged over 20 cycles. The mixture inhomogeneity can be seen only during the gas exchange.

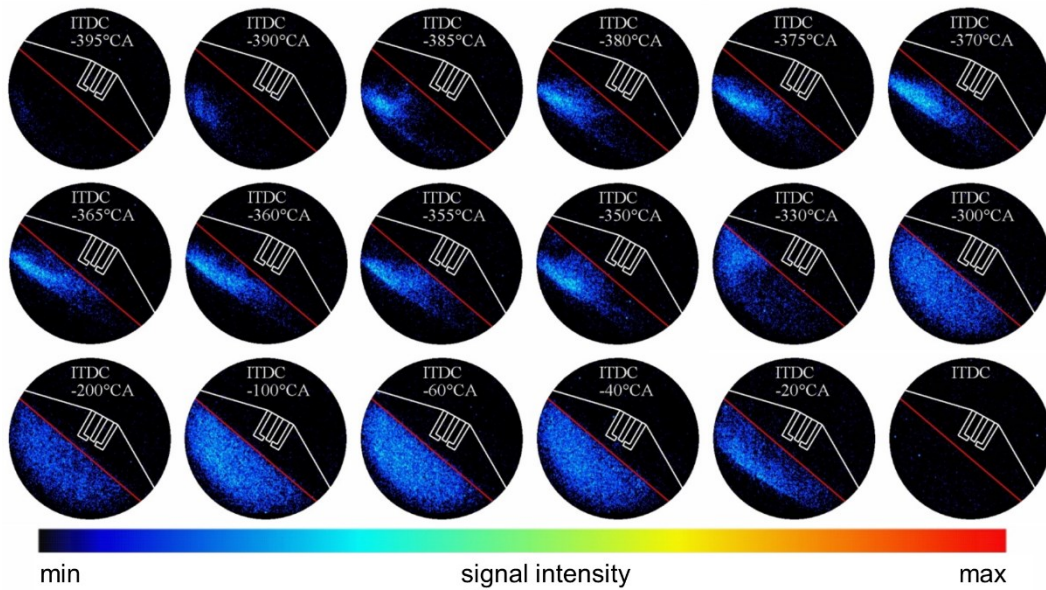


Figure 3.23: Toluene-LIF images during the gas exchange and compression stroke. The images are averaged over 20 cycles [4].

3.4.3.3 Two-color toluene-LIF imaging of gas-phase temperature

In the next phase, endoscopic visualization of the temperature field during compression stroke and gas exchange inside the combustion chamber was performed via two-color LIF thermometry [4, 58]. The principle of two-color LIF thermometry is described in section 2.1.2.1. Figure 3.24 shows the averaged images from both “blue” and “red” channels (280 ± 10 nm and 320 ± 20 nm, respectively) at different crank angles during the compression stroke and the temperature distribution [58]. The spatial temperature distribution is uniform, but the temperature images become noisier at later crank angles due to lower signal levels due to higher pressures. The small ROIs ‘a’ and ‘b’ were used to obtain a local average temperature for comparison.

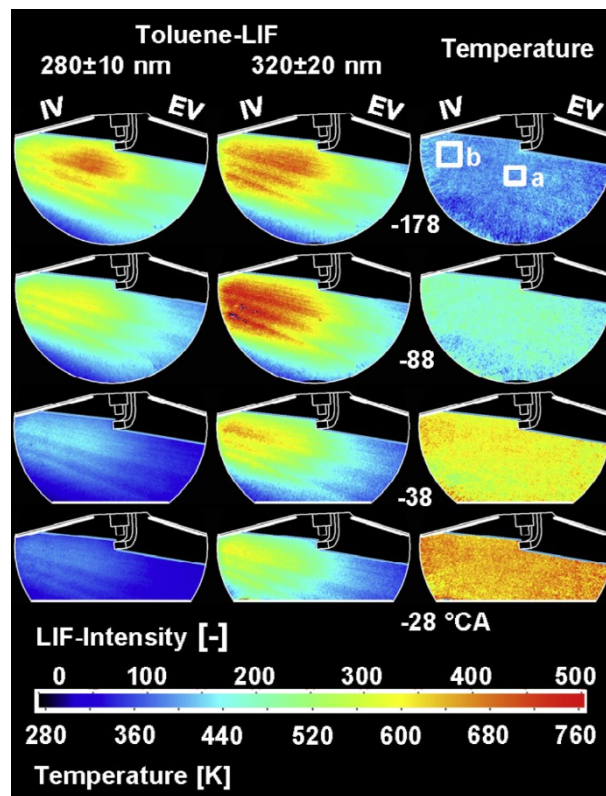


Figure 3.24: Averaged imaged of “blue” and “red” channels of toluene-LIF, and the resulting average temperature field during the compression stroke [58].

Figure 3.25 shows the average temperatures measured by two-color LIF during the compression stroke and the simulated temperatures (simulated in GT-power) [58]. Measured temperatures labeled (a) and (b) are from the ROIs shown in Figure 3.24. The measured temperatures are in good agreement with the simulation during the early and middle compression stroke. The higher difference between measured and simulated temperature increased in late compression stroke could be due to several reasons, e.g., lack of spectral and calibration data, and lower signal levels at high temperature and pressure [58].

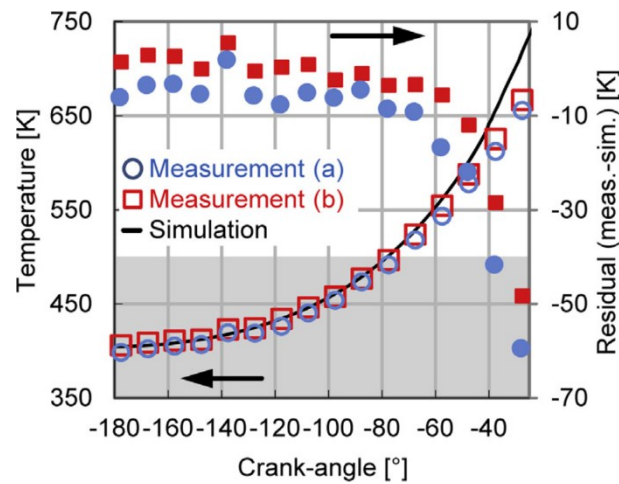


Figure 3.25: Comparison of temperature measured by two-color LIF and simulated temperature. Grey background indicated the range of in-situ calibration. The difference between measured and simulated temperatures is indicated on the secondary axis [58].

Figure 3.26 shows the single-shot images of the “blue” channel and the temperature image at different crank angles during gas exchange [58]. Higher signal levels due to atmospheric pressure during the gas exchange make it possible to get an instantaneous spatial temperature distribution. The image at 333°CA (late in the exhaust stroke) shows some signal, even though the intake valve was still closed, possibly due to an evaporating fuel film or crevice outgassing. The temperature was determined nonetheless, based on the assumption that these signals were from toluene or some altered species, with fluorescence spectrally similar to that of toluene [58]. The temperature at this crank angle was 545 K, which increased to 680 K at 373°CA. This indicated mixing of unburnt/fresh charge with back-flowing exhaust gases which is consistent with the simulations in GT-power, and also supported by the convective flow direction of the unburnt/fresh charge shown in the images in Figure 3.26. Once the exhaust valve is closed, the convective flow pattern disappears and fresh charges starts filling up the cylinder, with hot gases in front ultimately mixing with it.

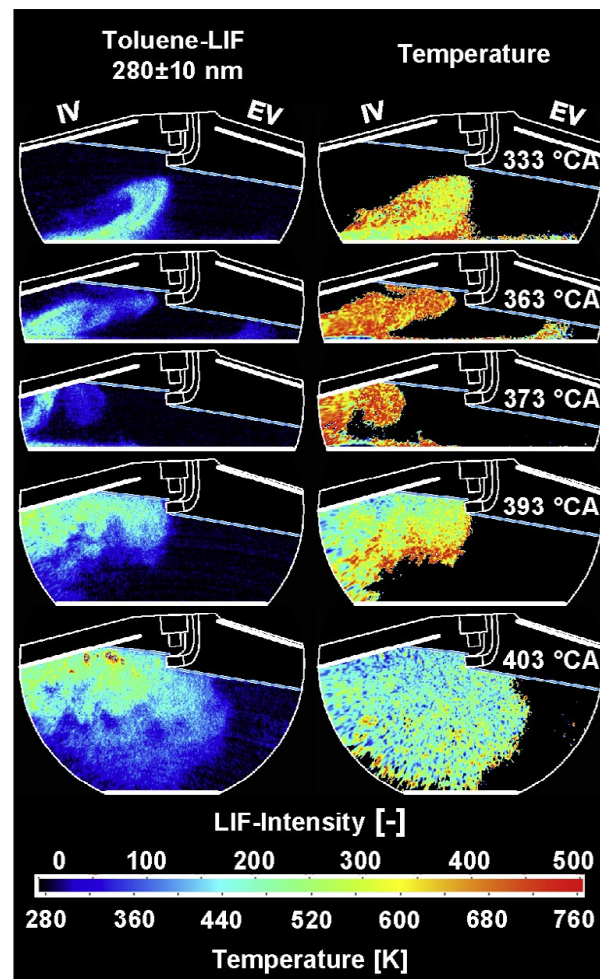


Figure 3.26: single shot “blue” channel and temperature images at different crank angles during gas exchange process [58].

4 Characterization of the UV endoscope system

This chapter presents the results from the experiments performed at the University of Duisburg-Essen in cooperation with LaVision GmbH. The results are partially reported in Shahbaz et al. [70].

4.1 Introduction

As discussed in section 3.2, the hybrid UV endoscope system consists of two parts: a front endoscope, and a hybrid diffractive/refractive optical element (DOE) acting as a relay lens projecting the intermediate real image onto the sensor. The DOE is customized for individual wavelength bands and corrects the spherical and axial chromatic aberration incurred in the front endoscope. However, the custom design and manufacture of the diffractive element is expensive and limits the application of a given endoscopic system to a narrow range of wavelengths. To make the system more universal, the hybrid DOE relay lens was replaced with a commercial UV lens, and the system performance of different combinations was compared in terms of resolution, brightness, and chromatic aberration. In this chapter, the results from the comparison of system performance are presented, and suitability of the imaging systems for different applications is discussed.

4.2 Methods

4.2.1 Imaging systems

Three basic endoscopic imaging systems were compared in this work, and two of them tested with further variations. All imaging systems included the same front endoscope, while three different lenses were used to accomplish the relay from the intermediate image plane to the sensor:

- a) Hybrid diffractive-refractive element for 275–350 nm, focal length 90 mm, $f/2$. (abbreviated DOE)
- b) LaVision 85 mm $f/2.8$ UV lens (LV)

c) Cerco 45 mm $f/1.8$ UV lens (CERCO)

The DOE and LV lenses were tested in further variations. The DOE has a fixed $f/2.0$ aperture, while the LV lens has a maximum aperture of $f/2.8$. To assess the performance of the DOE in comparison to the LV in more detail, an aperture was mounted just in front of the DOE. Relative aperture values of $f/2.8$ (DOE/2.8) and $f/3.5$ (DOE/3.5) were used. Since even the maximum aperture of the LV lens is smaller than the $f/2$ that the system was originally designed for, it was examined if it possible to improve the light collection of that lens by mounting a UV achromat in front of it. Such addition of “close-up lenses” is common practice in macro photography, albeit there typically to increase the maximum reproduction ratio. Here, one of two UV achromats with $f=200$ and 300 mm (Halle GmbH, Berlin) were used. These combinations are designated LV-ac200 and LV-ac300 in the following. Adding the achromats improves the relative aperture to $f/2$ and $f/2.2$, respectively. To focus the relay lens at the desired magnification, extension tubes were added as appropriate to the LV and CERCO lenses.

4.2.2 Experiment

A schematic diagram of the imaging train is shown in Figure 4.1. A back-lit knife edge was positioned 35 mm in front of the endoscope. LEDs with center wavelengths of 280, 310, 325, 340, 355, 370, and 385 nm, with a typical spectral width of about 10 nm FWHM, were used for illumination. The LEDs were mounted on a rotating wheel, such that the alignment was not disturbed when the wavelength was changed. The large divergence angle of LEDs was reduced by using a condenser lens. Two fused-silica diffusers were used to achieve more uniform illumination. The detection endoscope projected a real intermediate image onto its field lens, which the relay lens then projected on the camera sensor.

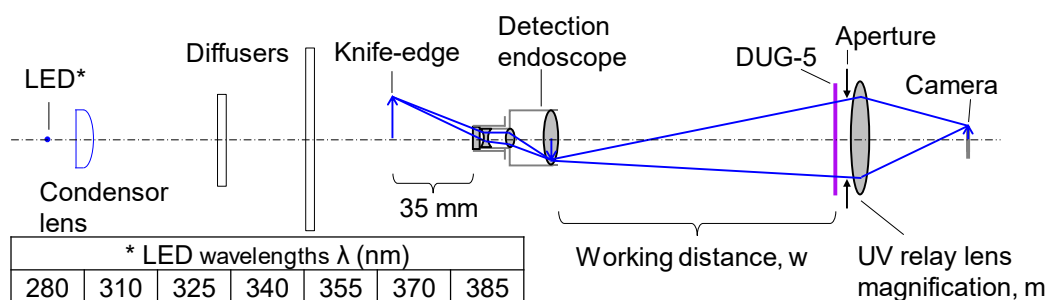


Figure 4.1: Imaging train and table of investigated wavelengths. Details on camera, magnification (m), and working distance (w) are given in Table 4.1.

Two different cameras were used. First, a UV-sensitive low-noise back-illuminated CCD camera was used at the relay magnifications of 1:2 and 1:1. Second, to investigate the effect of intensifier on the system performance an ICCD camera was used at the relay magnification of 1:1. The details on the cameras are summarized in Table 4.1. The experiments were performed in a dark room. To further prevent interference from visible light from other equipment in the room, a broad UV bandpass filter (DUG-5) was mounted on the relay lens.

Table 4.1: Camera specifications and experimental parameters. The gain is given as the user-interface input to DaVis, the camera control software used for the experiments.

	Andor iKon-M (CCD)		PCO Sencam + LaVision IRO (ICCD)
Sensor size (mm)	13.3 × 13.3		17.8 × 13.4 (at intensifier plane)
Pixel size (μm)	13 × 13		12.9 × 12.9 (at intensifier plane)
Exposure time (ms) / gain	400 / -		9.99 / 75 (bench-top) 0.02/ 75 (OH*-chemiluminescence)
Working distances, d (mm)			
Relay magnification, <i>m</i>	1:2	1:1	1:1
DOE	230	180	200
LV	230	180	200
LV-ac200	160	-	-
LV-ac300	155	-	-
CERCO	115	85	90

The CCD camera was equipped with a mechanical shutter, which was kept open throughout the experiment, and the effective frame exposure time was controlled by LED's illumination duration. That parameter was varied between 290 and 15 ms to have similar levels of detected light at all wavelengths and was kept constant for each wavelength. The camera exposure time was kept constant at 400 ms. The read-out time was 1048 ms at the read-out speed of 1 MHz. The whole timing scheme is shown in Figure 4.2. In ICCD cameras, the exposure time is typically controlled by the gate time of the intensifier. In the experiments involving ICCD, the LEDs were kept on all the time, and the intensifier gate was set to the maximum possible value of 9.99 ms with a gain of 75 (as set in DaVis

software). The imaging with ICCD was performed at 10 frames per second. Since the angle of the knife-edge should remain in a short range to avoid a systematic error in MTF evaluation (see section 4.3.2), care was taken to make sure that the knife-edge always returned to approximately same position after being moved to take the flat field images.

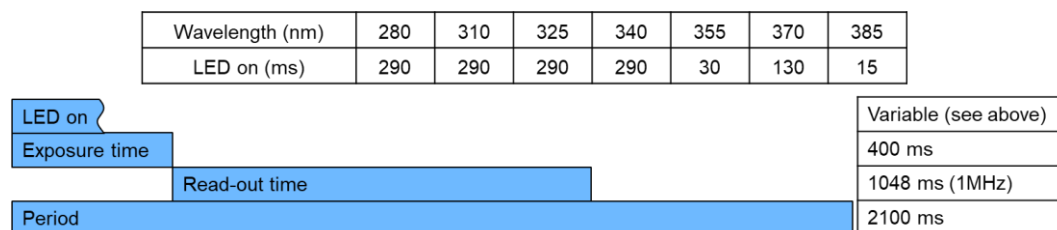


Figure 4.2: Timing scheme for the CCD camera

In order to assess how well the imaging systems limit the chromatic aberration over the wavelength range, the CCD camera with the relay magnification of 1:2 was focused at a selected wavelength, and images were taken at all available LED wavelengths. Care was taken not to disturb the focus position of the imaging system in a wavelength switch. This procedure will be called a “wavelength sweep” in the following discussion. Three wavelengths were selected for sweeps, 280, 325, and 355 nm. Two of them are on the edges of design wavelength range of the DOE (275–350 nm), and one in the center. In addition to the wavelength sweeps, individual experiments were performed with the imaging system focused at the wavelength at which the image was then taken.

In order to assess the influence of intensifier, selected imaging systems were investigated with an ICCD on the test bench. The measurements were performed only at 325 nm, which is the center of design wavelength range of the DOE. For a fair comparison, and to investigate the effect of the relay magnification on the performance of the selected imaging systems, the measurements were performed with the CCD at the same relay magnification as with the ICCD (1:1). Later, these selected imaging systems were used with ICCD to visualize the OH*-chemiluminescence and the spark in an endoscopic engine. Here, the imaging was performed with an intensifier gate of 20 μ s with a gain of 75. The detection endoscope was cleaned before each engine run. A band-pass 312/35 nm filter was used to isolate OH*-chemiluminescence signals from broadband visible chemiluminescence. The image train for imaging OH*-chemiluminescence and spark is shown in Figure 4.3.

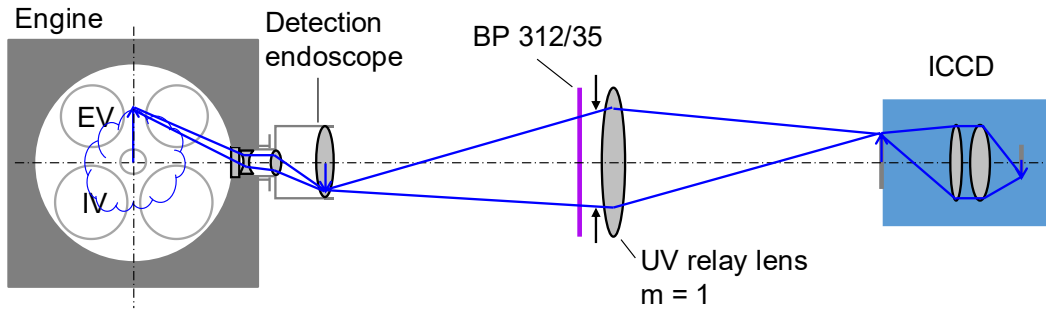


Figure 4.3: Image train for OH^* -chemiluminescence imaging in endoscopic engine.

4.3 Measurements and post-processing

4.3.1 Images

Three kinds of images were taken: Background (BG), knife-edge (KE), and flat field (FF). Background images were taken with the LEDs switched off and are not shown here. Average knife-edge and flat-field images are shown in Figure 4.4. For resolution measurements, corrected knife-edge (KE^*) were obtained by first averaging and subtracting the average background, and then dividing by the background-corrected average flat-field, as mentioned in the Eq 4.1.

$$\text{Corrected image } KE^* = \frac{\langle KE \rangle - \langle BG \rangle}{\langle FF \rangle - \langle BG \rangle} \quad \text{Eq 4.1}$$

$\langle \rangle = \text{averaged}$

The MTF was evaluated from a 50×50 pixel region of interest (ROI) in the center of KE^* . For quantifying light collection efficiency, a region of 200×200 pixels in the center of the background-corrected flat-field images was averaged.

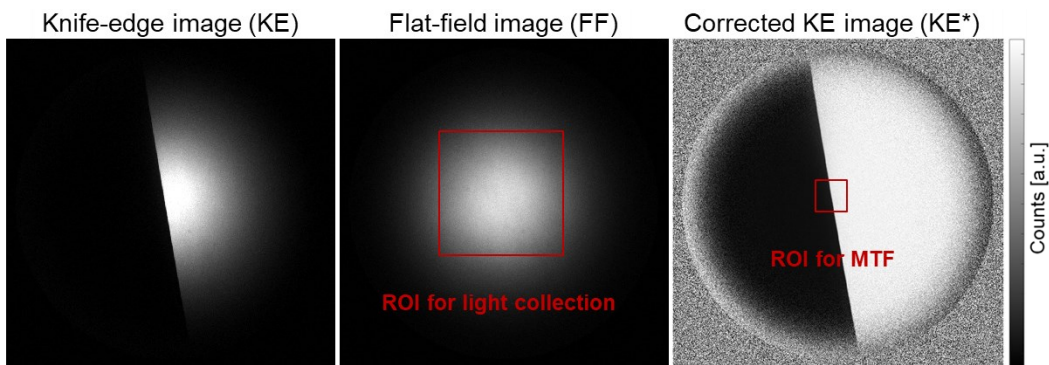


Figure 4.4: Raw and processed example images. (left to right) knife-edge image, flat-field image, corrected knife-edge image KE^* .

4.3.2 Modulation transfer function

In previous work at the IVG, a MATLAB script had been developed based on the ISO 12233 standard, with some minor changes in the method to calculate the ESF [71]. Figure 4.5 shows the steps to determine the MTF from a sample KE* image, and typical ESF, LSF, and MTF plots. First, an ROI is selected and then instead of projecting the pixels in the direction of the slope, the edge is straightened by determining the centroid and a so-called anti-slope function and shifting the rows accordingly. The pixels are then projected vertically onto a horizontal axis and resampled by taking moving average of the number of pixels defined by the resampling factor. The resampling factor used in this case was 5, which roughly corresponds to half of the pixel width. This is twice as much as suggested in the ISO standard, but was chosen as the images at some investigated wavelengths had significant noise which generated errors during the computation of MTF.

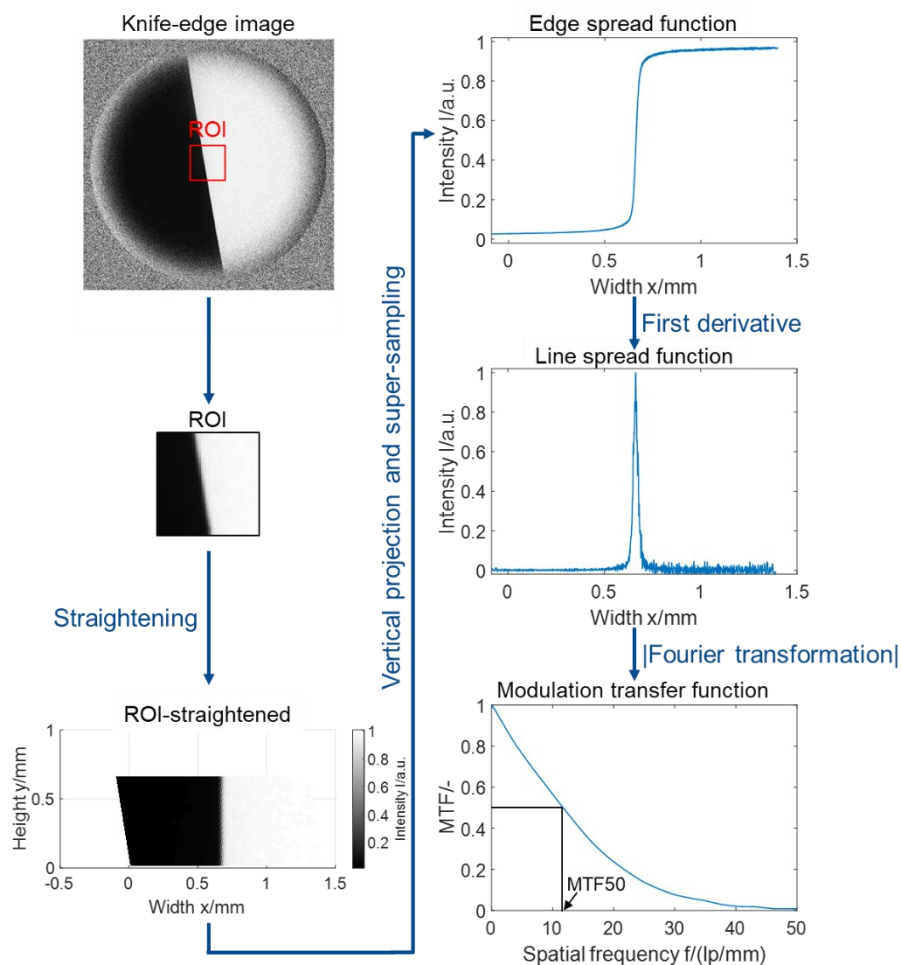


Figure 4.5: Steps to determine the MTF based on the slanted-edge method by an in-house MATLAB script.

Afterwards, the LSF was obtained by taking the first derivative of the ESF, and a Hamming window was applied. In the final step, taking the modulus of a discrete Fourier transformation of the LSF yields the MTF. MTF plots are typically normalized to unity at zero spatial frequency, which might have some implications while comparing the MTF of different imaging systems. Therefore, in this work MTF50 (the spatial frequency at 50 % MTF), which is the half-width-at-half-maximum (HWHM) of the MTF curve and is not affected by normalizing, has been used as a metric to compare the resolution of the investigated imaging systems.

To evaluate the accuracy of the MATLAB script, synthetic images (with pixel size of $10 \mu\text{m} \times 10 \mu\text{m}$) were simulated in MATLAB with different slanted-edge angles. The pixels that were blocked by the imaginary knife-edge were assigned the values of 0 (black) and those exposed were assigned the value of 1 (white). The pixels that were partially exposed (grey pixels) were assigned values based on the area of the exposed sub-pixel, e.g., 0.45 for a pixel whose 45 % pixel area was exposed. Figure 4.6 shows the MTF plots based on synthetic images with different slanted-edge angles, and the theoretical MTF of the sensor, based on the same pixel size as that of the synthetic image's, calculated by Eq 2.5. The MTF curve at 5° angle is slightly over the theoretical MTF curve, while the curves at the rest of the slanted-edge angles are below, with the difference increasing with the angle. This is broadly consistent with the results of Estribeau et al. [45] with slight differences due to different approaches in estimating the ESF.

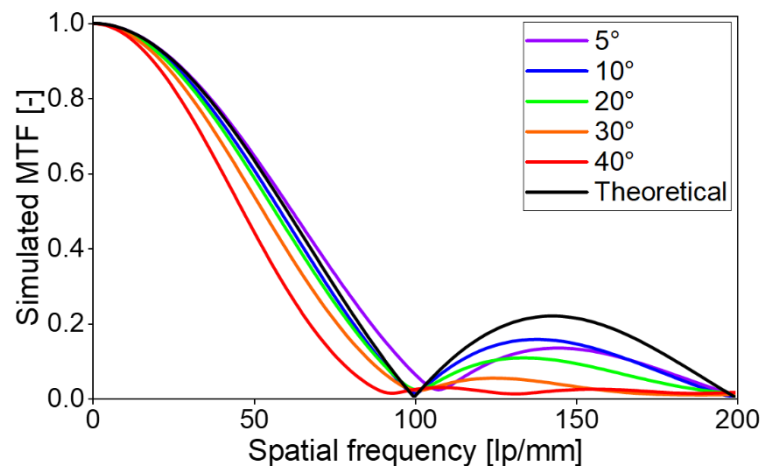


Figure 4.6: Comparison of MTF plots based on synthetic images with the slanted-edge at different angles and theoretical MTF of the sensor.

Since MTF50 is the metric used to compare the performance of different imaging systems in this work, the values obtained by MTF plots at different slanted-edge angles are

compared with theoretical MTF50 value in the Figure 4.7. The graph shows that the MTF50 for 5° slanted-edge angle is overestimated compared to the theoretical MTF50 (60.3 lp/mm), which is obtained from the theoretical MTF curve, while all the rest are underestimated with a plateau between 8° and 12°. A slanted-edge angle of approximately 9° was used in this work, since it was in the middle of the plateau and a slight error in reproducing this angle in different experiments would not result in significant error.

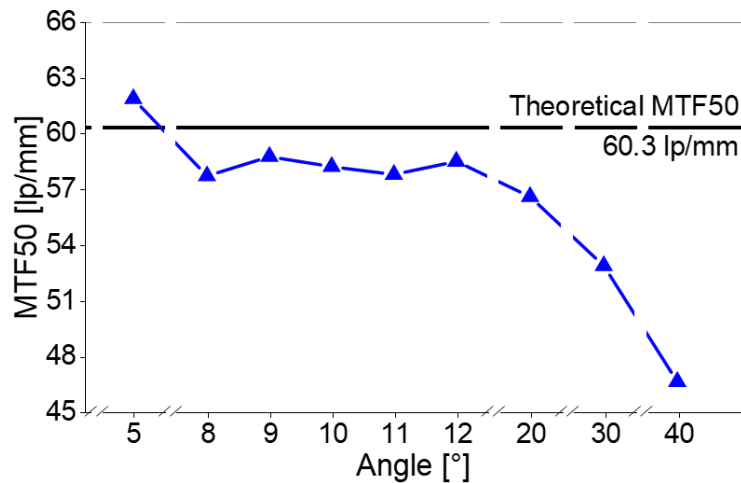


Figure 4.7: MTF50 as a function of the angle of the slanted edge.

4.4 Results

4.4.1 Chromatic aberrations

Figure 4.8 shows the MTF50 of all imaging systems over the investigated wavelength range. The relay magnification was 1:2 for the results in this section. The black-edged points represent the focus wavelength and the points without black edges (connected by lines) represent results from wavelength sweeps with the focus unchanged. For reference, the pixel-limited MTF50 for the CCD is 45.3 lp/mm. Thus, for all combinations with the CCD, the system resolution is dominated by the optics, not the sensor.

Figure 4.8a shows that with the DOE, ‘good’ system resolution is indeed limited to the design wavelength range of 275–350 nm. When the system is focused in the central region of this range, the performance is considerably better, as can be seen by the 310 nm point and the 325 nm line. When focused at 325 nm, performance degrades towards the spectral edges of the design range, and further degrades outside the design range. When the system is focused at the wavelengths near the edges of the design range, i.e., 280 nm and 355 nm, performance is degraded in the central design range, and is better towards the other edge of

the design range. This behavior is consistent with the results by Reichle et al. [11]. The results with the reduced apertures of $f/2.8$ and $f/3.5$ on DOE are shown in Figure 4.8b and Figure 4.8c respectively. As expected, by reducing the aperture, the system resolution was generally improved. However, the peaks of the wavelength sweeps are still narrower than with the LV and CERCO lenses, indicating that the narrow chromatic correction range is an inherent feature of the design approach.

The performance of the LV lens coupled with the front endoscope is shown in Figure 4.8d. In all cases, the MTF50 values are higher than with the DOE. Contrary to the DOE, the LV lens maintained the system resolution over the whole investigated wavelength range. The peaks for wavelength sweeps were broader than with the DOE when focused at 325 and 355 nm. Also, the “resolution trough” that the DOE showed when focused at 280 and 355 nm was not observed for any focus wavelength. Somewhat surprisingly, as Figure 4.8e and Figure 4.8f show, combining the LV lens with either UV achromat drastically reduces system resolution. The 200-mm achromat yields worse performance than the 300-mm one. The LV achromat combinations, however, still limited chromatic aberration over a larger wavelength range than the DOE, especially for detection wavelengths around the short-wavelength edge of the DOE design range of 275–350 nm.

Figure 4.8g shows that with the CERCO as a relay lens, the system had similar resolution as with the LV lens. It had slightly worse performance in the deep UV (280 nm). However, at 1:2 magnification the working distance of the CERCO is only 115 mm. This working distance is only half of that afforded by the other options, providing less space for any additional optical elements such as beam splitters and filters to be placed in the optical bath, which may limit using the short-focal length CERCO as a relay lens.

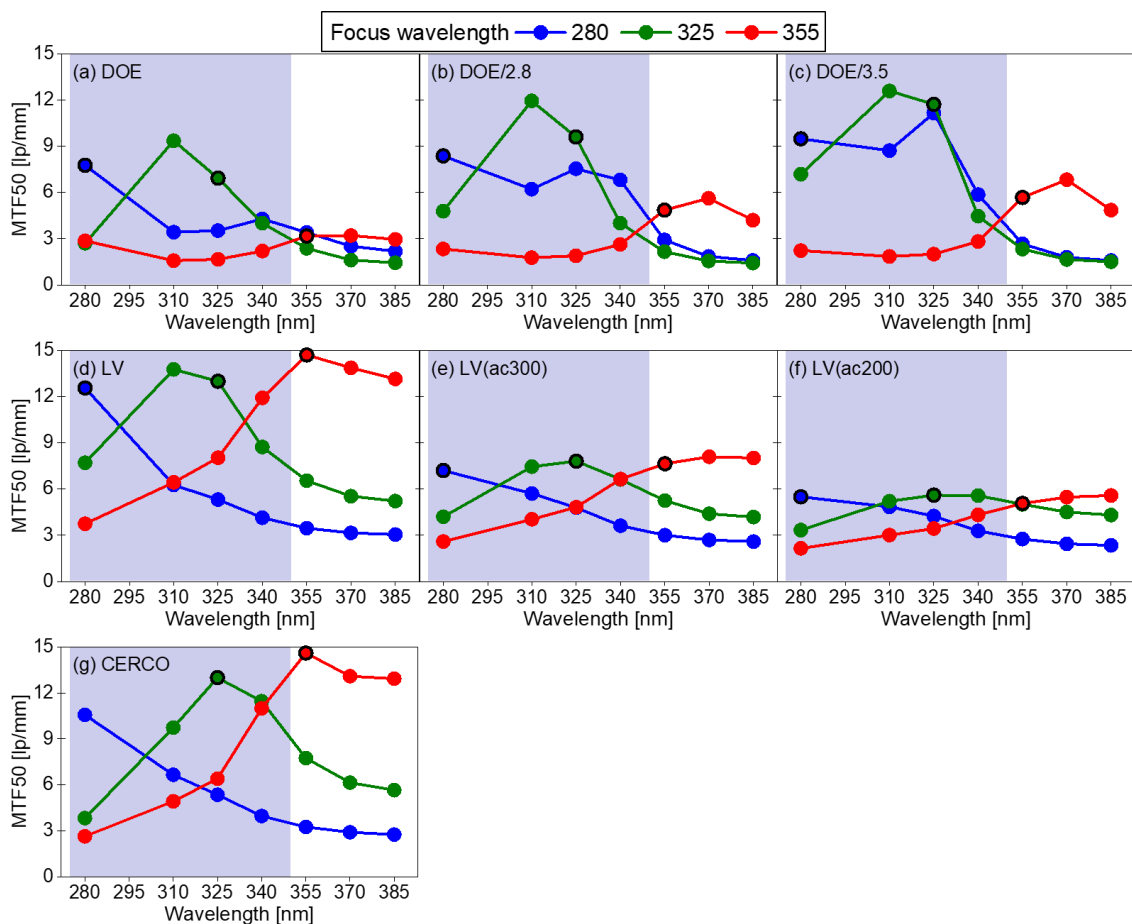


Figure 4.8: MTF50 as a function of illumination wavelength for all imaging systems. Black-edged points represent the focus wavelength. Connected points represent wavelength sweeps with fixed focus. The blue background indicates the design wavelength range of the DOE.

4.4.2 Quasi-monochromatic resolution

The resolution performance of the imaging systems focused at each wavelength is summarized in Figure 4.9. Since the illuminating LEDs had a narrow spectral range, these results essentially reflect monochromatic resolution. The relay magnification was 1:2 here. The LV lens yields the best system performance over the whole wavelength range, closely followed by the CERCO. Both of these systems slightly degrade towards the deep UV, probably a consequence of the two lenses being designed for the UV and visible range. With the DOE stopped down to $f/3.5$, the system resolution is nearly the same as that with LV or CERCO at 280 to 325 nm, but significantly worse at longer wavelengths. Among all systems, LV with either UV achromat yields the worst performance in the deep UV but is competitive with the DOE above 340 nm. Overall, the results indicate that the refractive

element works best only in its spectral design range, even when refocusing at the detection wavelength.

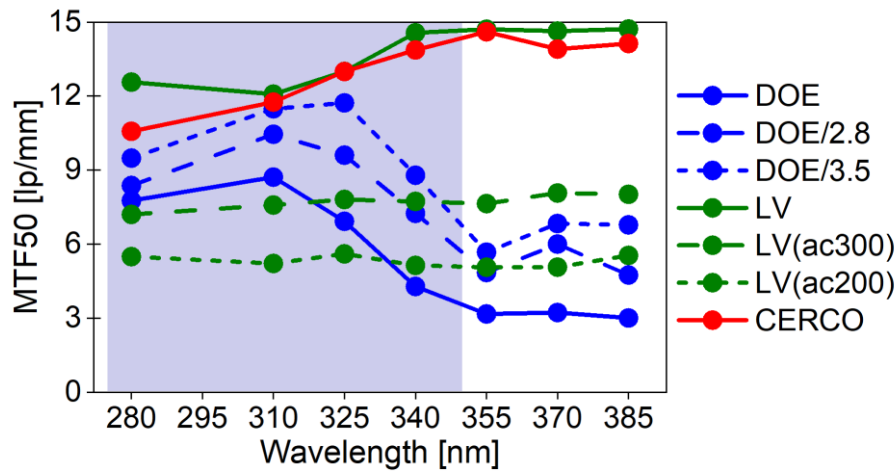


Figure 4.9: MTF50 values at the focus wavelength. The blue background indicates the design wavelength range of the DOE.

4.4.3 Light collection efficiency

Figure 4.10 compares the detected intensity in the center of flat-field frames. The results from all seven wavelengths for each system were averaged. As expected from their larger apertures, DOE and CERCO yield similarly bright images, while the system's sensitivity with the LV lens is about a factor of three worse. Even at $f/2.8$ and $f/3.5$, the DOE collects more light from the front endoscope's field lens than the LV lens wide open, although at $f/3.5$ the numbers are close. This is consistent with the transmission-corrected relative aperture of $t/3.9$ that the manufacturer quotes for that lens. Adding the 300 or 200-mm achromat to the LV lens improves light collection by 31 % and 47 %, respectively. From the f -numbers, for an isotropic light source, 61 and 100 %, respectively, would have been expected, but the field lens is not an isotropic source (directing the light towards the relay is its purpose), and the achromats were uncoated.

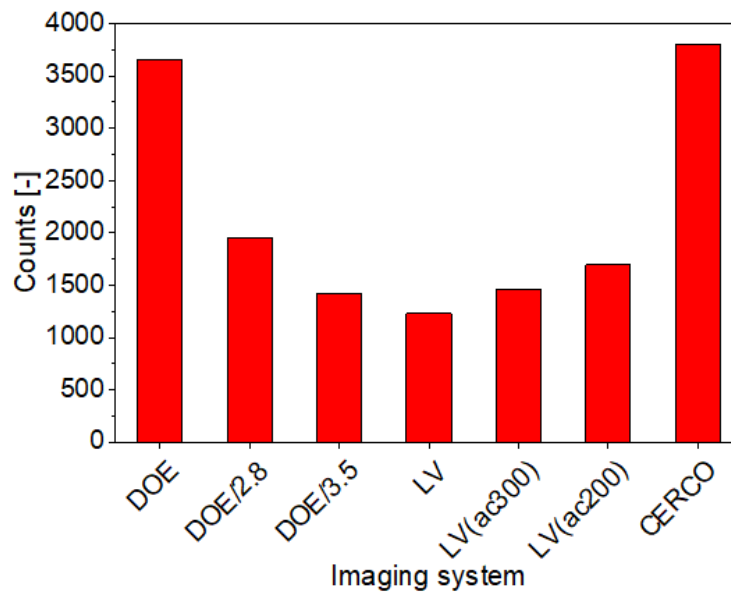


Figure 4.10: Light collection for different imaging systems using two different cameras.

4.4.4 Effect of magnification

The effect of magnification on the resolution was investigated by performing the experiments with the CCD at the relay magnification of 1:1 and comparing them with results at the relay magnification of 1:2. Figure 4.11 shows the resulting MTF50 values. With the DOE at 1:1, the MTF50 is almost unaffected by reducing the aperture. The divergence angle of the light from the field lens is narrow. At the short working distance at 1:1 magnification, the actually-illuminated entrance pupil diameter is similar in diameter as the apertures in front of the DOE. The actually-illuminated entrance pupil diameter was found to be about 28 mm, and the diameters of the physical apertures placed in front of the DOE were 32.1 mm and 25.7 mm for DOE/2.8 and DOE/3.5, respectively.

For an isotropic light source, doubling the magnification would decrease the MTF50 by about half, since (in first order) the aberrations are magnified by a factor of two. This is not what is observed in the experiments represented in Figure 4.11. For DOE, LV and CERCO, a reduction of about 26–28 % was observed. This is probably because the MTF50 in the former case (with magnification 1:2) are affected by spherical aberrations produced in the outer periphery of the relay lens. In the latter case, these spherical aberrations are not produced because the illuminated entrance pupil diameter was smaller.

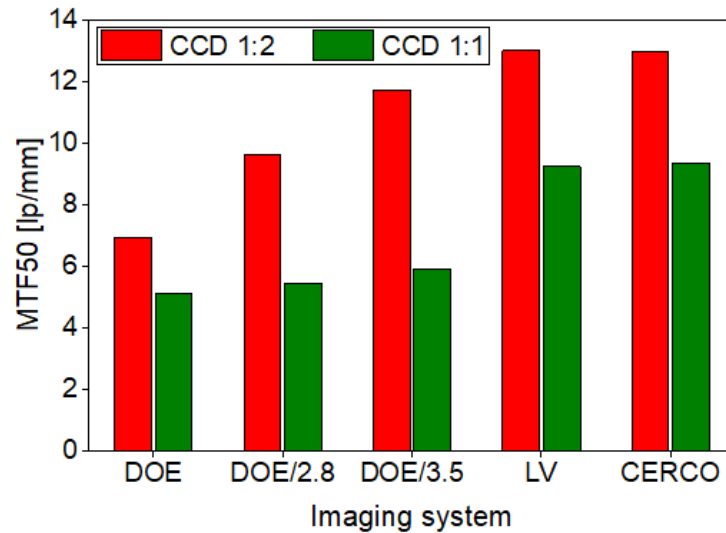


Figure 4.11: MTF50 values with CCD camera at different magnifications

Figure 4.12 shows a comparison of the light collection at 325 nm with the CCD at different magnifications. Again, in contrast to $m = 1:2$, at $m = 1:1$ the light collection remains unaffected by the apertures in front of the DOE because of the smaller illuminated entrance pupil. CERCO has a similar light collection as DOE and its variants. LV, despite having similar aperture as DOE/2.8, has worse by a factor of two light collection. This is simply due to the worse transmission of LV, as indicated by its transmission-corrected relative aperture of $t/3.9$

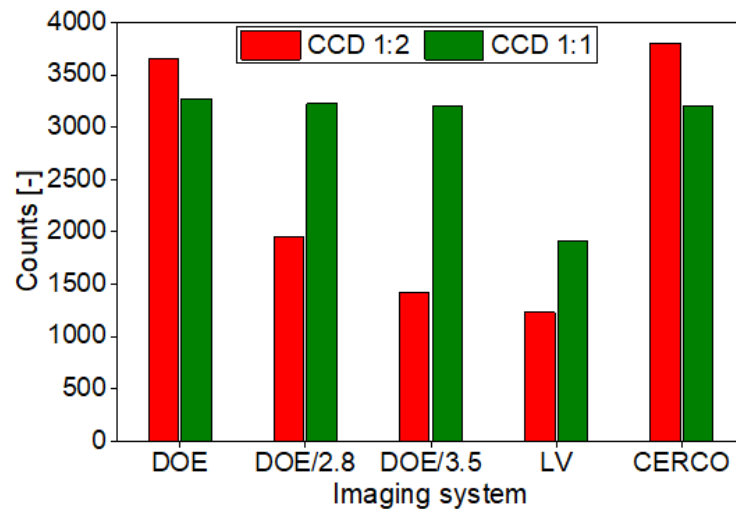


Figure 4.12: Light collection with the CCD camera at different magnifications.

4.4.5 Effect of the intensifier on the resolution

Figure 4.13 shows the MTF50 values at 325 nm with CCD and ICCD cameras. The relay magnification was the same for both cameras, i.e., 1:1. The hybrid UV endoscope system was originally designed for a relay magnification of 1:1 in combination with an intensified camera [2]. The ICCD used here has an internal magnification factor of 1:2 between the intensifier photocathode and the camera sensor. For a fair comparison, the MTF50 values were calculated at the sensor plane and then translated onto the plane of the photocathode by dividing them by two.

The results in Figure 4.13 shows that intensifier limits the resolution in all investigated imaging systems. Also, DOE and its variants showed similar performance with CCD and ICCD at same magnification. This validates the original design concept of the hybrid UV endoscope system, in which the resolution of an intensifier was considered as one of the boundary conditions [2].

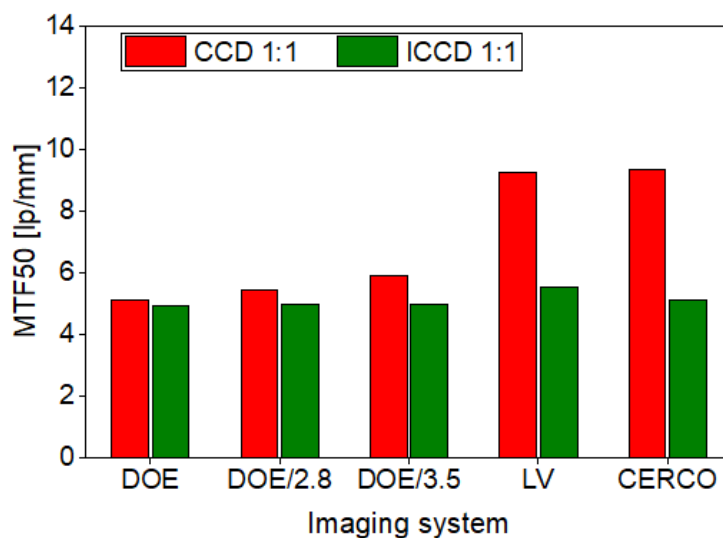


Figure 4.13: Influence of the intensifier on MTF50.

4.4.6 OH*-chemiluminescence imaging

The imaging systems, except for the combinations of LV and achromats, were used to image the OH*-chemiluminescence in a production spark-ignition 4-cylinder BMW engine (see section 5.2 for the engine details). The engine has port-fuel injection and was run stoichiometric at 2000 min⁻¹ and 60 Nm brake torque (3.78 bar BMEP). Snapshot images with 20 μs exposure time at fixed crank angles were acquired by an intensified CCD camera

with a 312/35 nm bandpass filter in front of the relay lens, as in [15]. The camera was focused about 6 mm in front of the cylinder's center plane. For each imaging system, Figure 4.14 shows an example image at 15 and at 20°CA aIT.

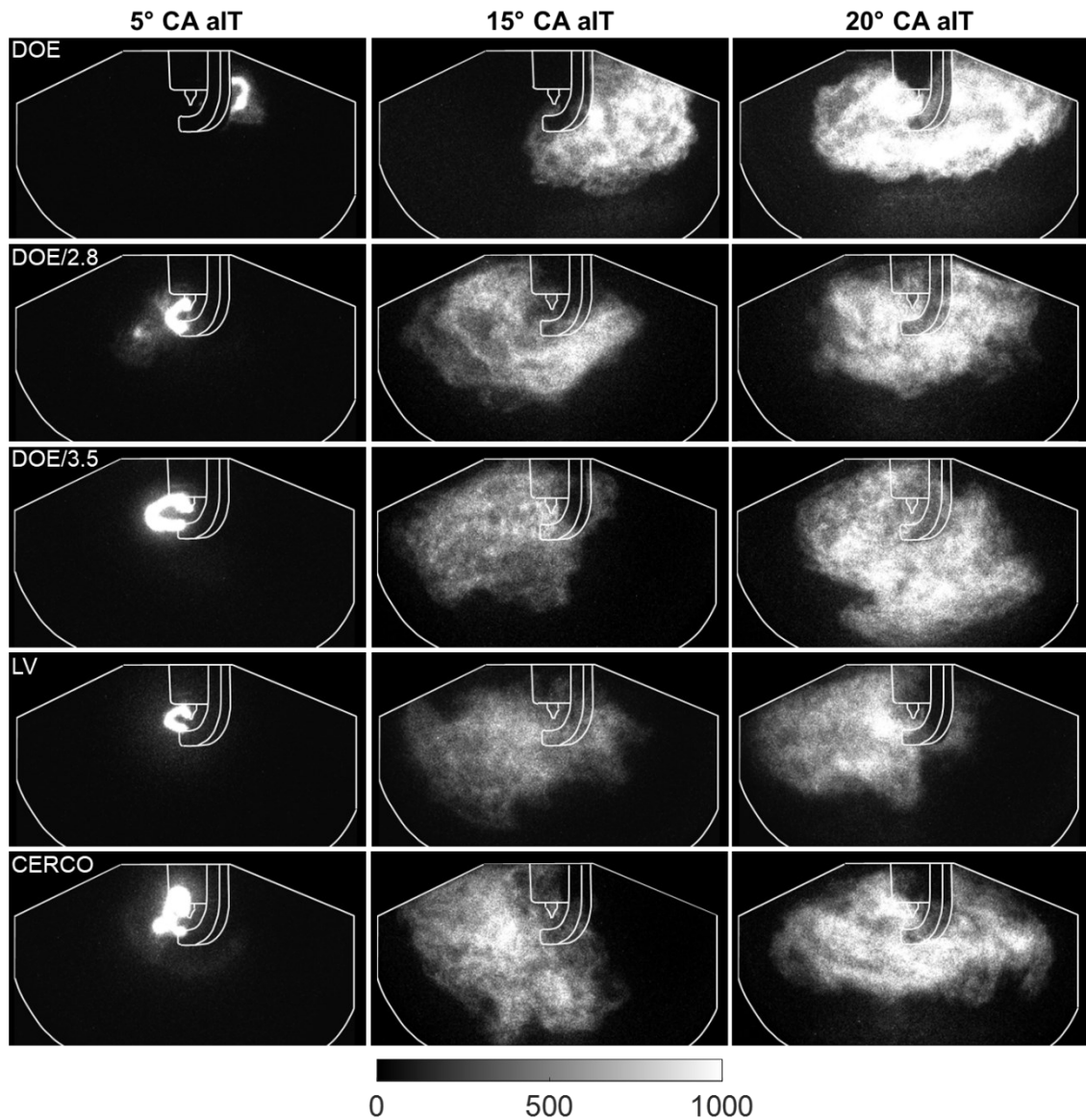


Figure 4.14: OH*-chemiluminescence images taken endoscopically in a spark ignition engine with different imaging systems.

In general, the resolution of all the imaging systems is well-suited for this application. However, the edges of the apparent flame front are clearly more blurred with the DOE, which also produces reduced contrast. Reducing the aperture brings the image in line with those recorded with the LV and CERCO lenses for relay imaging. Among the few sample shots shown here, CERCO and DOE/3.5 seem to yield the best-resolved images, but this may also be due to the particular flame realizations captured in the snapshots. Qualitatively,

the relative image brightness is consistent with the bench-top results as summarized in section 3.4.1.

5 Endoscopic two-color anisole-LIF temperature imaging in a PFI engine

5.1 Introduction

Tracer-based laser-induced fluorescence (LIF) has been widely used as a non-intrusive diagnostic for quantitative measurement of fuel concentration, temperature and fuel/air ratio in combustion applications [19, 20]. LIF has also been used to detect the flame front by negative-LIF technique in [5, 72], and to investigate the formation and evaporation of piston fuel films [73-75]. The effect of tracer quantity added into the non-fluorescent base fuel can generate substantial systematic error due to different physical properties, and hence prevent the accurate quantification of LIF signals [19]. In particular, toluene has been well investigated as a tracer for LIF applications [21, 23, 30], and used as a tracer for LIF measurements in combustion engines, e.g., to image equivalence ratio and fuel distribution [16, 76, 77], to investigate fuel films in DISI engines [74, 78, 79], and to image the gas-phase temperature distribution [58, 80, 81]. Toluene has also been used as a pure fuel for LIF application in combustions engines in [82]. Recently, anisole (methoxybenzene, $\text{CH}_3\text{OC}_6\text{H}_5$, boiling point 154°C) was characterized spectroscopically for engine-relevant pressures and temperatures [83-86] and emerged as a potentially advantageous alternative to toluene [23, 84, 87]. The absorption cross-section of anisole when excited at 300 K with 266 nm laser is $1 \times 10^{-17} \text{ cm}^2$, which is two orders of magnitude larger than the absorption cross-section of toluene [85]. Therefore, anisole produces stronger LIF signal per volume than toluene, which may enable better measurements, while having less effect on the combustion process due to the lower tracer concentration required.

This work is a direct extension of the work of Goschütz [5] and preliminary work of the author, Shahbaz et al. [88]. In this work, it was investigated if the previously reported endoscopic two-color LIF-thermometry [58] could be improved to single-shot imaging by substituting anisole for toluene. Anisole LIF spectra exhibit a red-shift with increasing temperature and oxygen partial pressure (p_{O_2}) which was exploited for temperature measurements using two-color thermometry. The effect of p_{O_2} is more profound at pressures lower than what corresponds to atmospheric pressure i.e. 210 mbar p_{O_2} [85]. This

temperature and p_{O_2} dependence of the anisole LIF spectra was used to devise a spectroscopic model for determining the gas-phase temperature from the pixel-wise red/blue signal ratio and p_{O_2} , with latter determined from the in-cylinder pressure data. This theoretical spectroscopic model was then calibrated in-situ. It was found that anisole LIF can indeed be used to determine the gas-phase temperature based on single-shot images [5, 88], but the accuracy of the results was low due to the inaccuracies in the in-situ calibration. Another issue was the selection of an appropriate interpolation function for the spectroscopic model. A 2nd order polynomial function by Luong et al. [81], and a 3-parameter exponential function by Kranz et al. [89, 90] are few of the many possible functions. Additionally, most of the previously reported works included experiments in nitrogen environment and the effect of p_{O_2} was not investigated [27, 81, 91]. Here, a customized yet simple calibration equipment was designed and used to perform in-situ calibrations over broader range of temperatures and with air and nitrogen as bath gases. Also, different mathematical interpolation models were used to extend the range of the spectroscopic models. These models were then used to determine temperatures along the compression stroke, and the results were compared to the adiabatic core temperature. Finally, a selected model was used to visualize temperature stratification and mixing of fresh charge and internally-recirculated exhaust gas during the gas-exchange process.

5.2 Engine and optics

Measurements were performed in a production line 4-cylinder inline, naturally aspirated, spark-ignited engine (BMW N46 B20). The engine operated with stoichiometric fuel/air ratio and was equipped with port fuel injection (PFI) and a mechanically actuated variable intake valve train (Valvetronic). The engine was coupled to a speed-controlled dynamometer, with the torque controlled by an analogue input to the engine control unit (ECU). Actuators, valve lift and timing, phasing and injection were managed by the production engine control unit (ECU) accordingly, to which there was read-out access only. The engine geometry and operating parameters are given in Table 5.1.

Table 5.1: Engine geometry and parameters

Displaced volume	1995 cm ³
Bore	84.0 mm
Stroke	90.0 mm
Compression ratio	10.0:1
Number of valves per cylinder	4
Intake valve lift	0.3–9.7 mm
Exhaust valve lift	9.7 mm
Fuel	Isooctane (C ₈ H ₁₈)
Equivalence ratio	1.0

The engine is modified in the 4th cylinder (the one nearest to the flywheel) to have two mutually perpendicular small endoscopic ports, one for laser light sheet endoscope and other for the front endoscope of the hybrid UV-endoscope system, each with a diameter of 13 mm. The light sheet endoscope and the detection endoscope are described in detail in Chapter 3. The engine, camera, laser guiding arm, and the optical geometry of the modified cylinder are shown in Figure 5.1. More details about the engine and modifications for endoscopic access can be found in [4, 60]. The engine was mounted such that the cylinder axis was tilted 38° from vertical. The camera axes were also tilted as shown in Figure 5.1, to avoid errors arising in the post-processing from rotating the images. However, this arrangement is challenging to realize. The cameras and the laser guiding arm were mounted on a separate frame, which provided some, but not complete, vibration-isolation from the engine. The laser-guiding arm is particularly sensitive to vibrations, as a very small spatial deviation in any direction could result in complete misalignment of the laser beam.

A custom fuel supply allowed “clean” operation on surrogate fuels without unknown fluorescing compounds in the endoscopically accessed cylinder, while a commercial fuel pump supplied high-octane commercial fuel (Shell V-Power Racing 100, RON = 100) to the other cylinders. This fuel was chosen because it closely matches the octane number of isooctane and is much cheaper than isooctane.

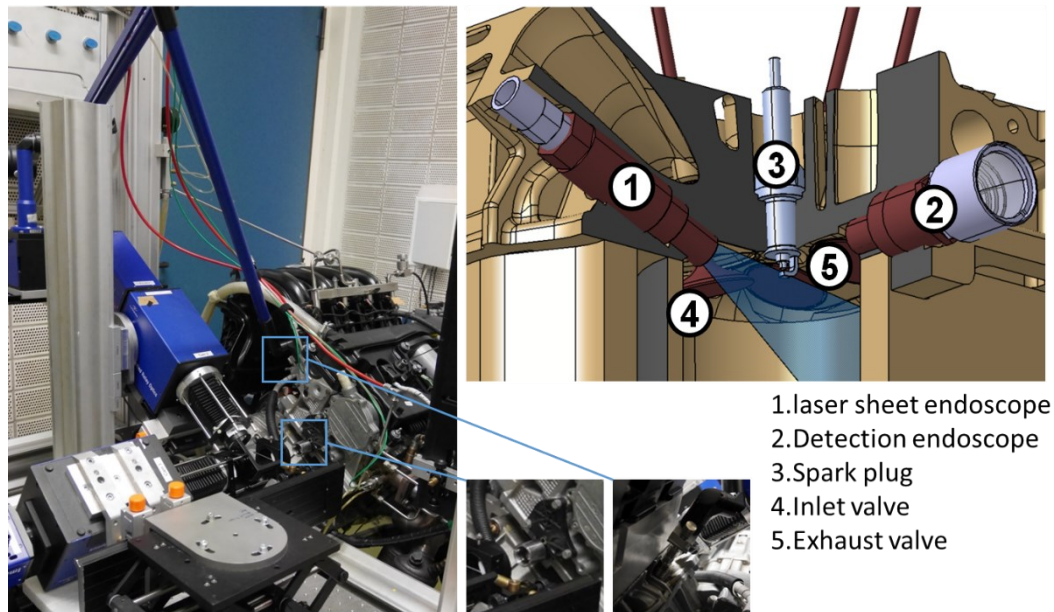


Figure 5.1 : Left: BMW all-metal engine with endoscopic optical access, laser guiding arm, and ICCDs. The insets show the detection endoscope (left inset) and the light sheet endoscope (right inset). Right: Schematic representation of the optical geometry of the modified cylinder [58].

All measurements were performed in continuously fired operation at 2000 min^{-1} and 4 bar indicated mean effective pressure. Throttling to this part-load was achieved by an intake valve lift of 2.2 mm. Ignition occurred at -35°CA . (In this thesis, 0°CA is taken to be compression top-dead center, i.e., crank angles during intake and compression are negative.) On the endoscopically accessed cylinder the crank-angle resolved pressure was measured and recorded. The temperatures of the intake and exhaust gases, engine oil, and the cooling water for the measurements used to measure temperature in section 5.4 are given in Table 5.2. The cameras and laser were controlled and synchronized with the engine by DaVis: imaging software from LaVision.

Table 5.2: Air, water, and engine oil temperatures measured during the experiment.

	Temperature [K]
Intake air	308
Exhaust gases	880
Engine oil	390
Cooling water inlet	298
Cooling water outlet	380

The schematics of the engine and optics are shown in Figure 5.2, while Figure 5.3 gives an overview of the most important spectral features in emission and detection.

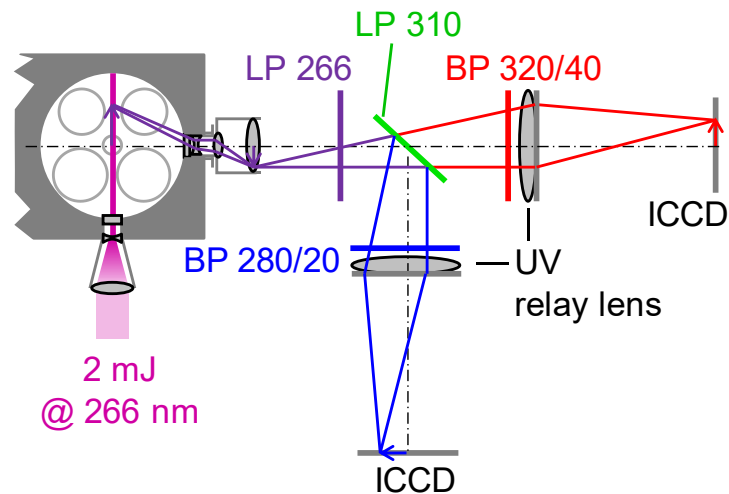


Figure 5.2: Arrangement of engine, optics, and detectors.

The beam of an Nd:YAG laser at 266 nm with a maximum repetition rate of 10 Hz was introduced into the light-sheet endoscope via the laser guiding arm. The laser energy was 2 mJ/pulse as measured before the endoscope that generates a 1 mm thick diverging laser light sheet through a set of cylindrical optics. A long-pass filter (LP 266) mounted behind the detection endoscope blocked reflected laser light. A beam splitter (LP 310) transmitted light above 310 nm onto an intensified CCD yielding an image from the “red” part of the LIF spectrum, while the reflected light below 310 nm was detected by an identical camera in the “blue” channel. Band-pass filters further constrained the spectral range of each “color” channel (BP 320/40 for the red channel and BP 280/20 for the blue channel). Both cameras were gated for 200 ns bracketing the laser pulse.

As the fluorescence spectrum of anisole red-shifts with increasing temperature, as shown in Figure 5.3a, the ratio of the signals detected on each camera changes. In principle, this ratio can be related to local temperature by a suitable calibration, as discussed in section 5.4.2.

With toluene as the tracer, from our previous work on two-color tracer-LIF [58], 20 % were used in isoctane. Alternatively, to keep absorption of the laser beam across the field of view similar, only 2.5 % anisole was added to the isoctane fuel.

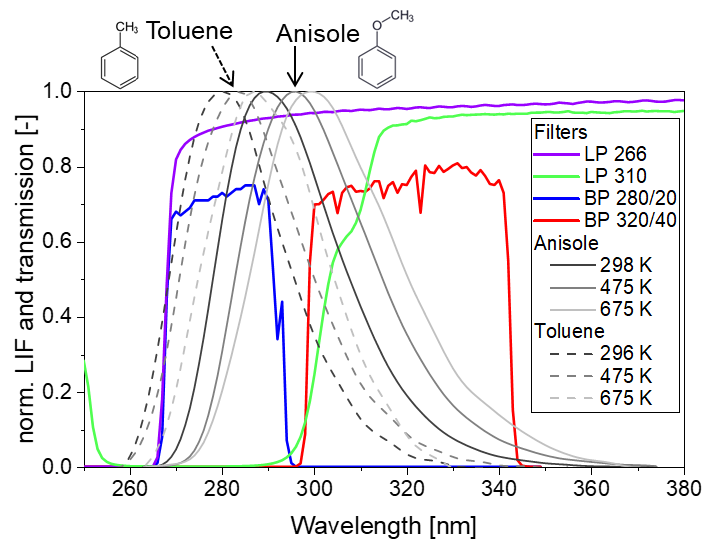


Figure 5.3: Spectral overview of emission and detection. Toluene and anisole LIF at different temperatures, and transmission of the filters used for two-color detection. Anisole and toluene spectra are from [23].

5.3 Anisole vs. toluene as a fuel tracer

For each tracer/fuel-mixture, Figure 5.4 shows two averaged red-channel images at -60°CA , and average counts in both channels in a 100×100 pixel ROI below the spark plug (red square). The laser energy was similar in both cases. The intensifier gate, gain, and binning were kept the same i.e. 200 ns, 80, and 2×2 respectively. Figure 5.4 shows that, in the red channel, the average detector counts from anisole-LIF are 5.5 times higher than toluene, although the volume of anisole added to iso-octane was 8 times less. This can also be attributed to the fact that more of the anisole spectrum is captured in the red channel than in the case of toluene (Figure 5.3). However, in the blue channel the situation is the opposite and toluene spectrum is spread over almost entire blue channel at 475 K, while anisole spectrum at 475 K covers roughly 40 % of the blue channel. Nevertheless, anisole LIF still has 1.5 times higher average counts in the blue channel.

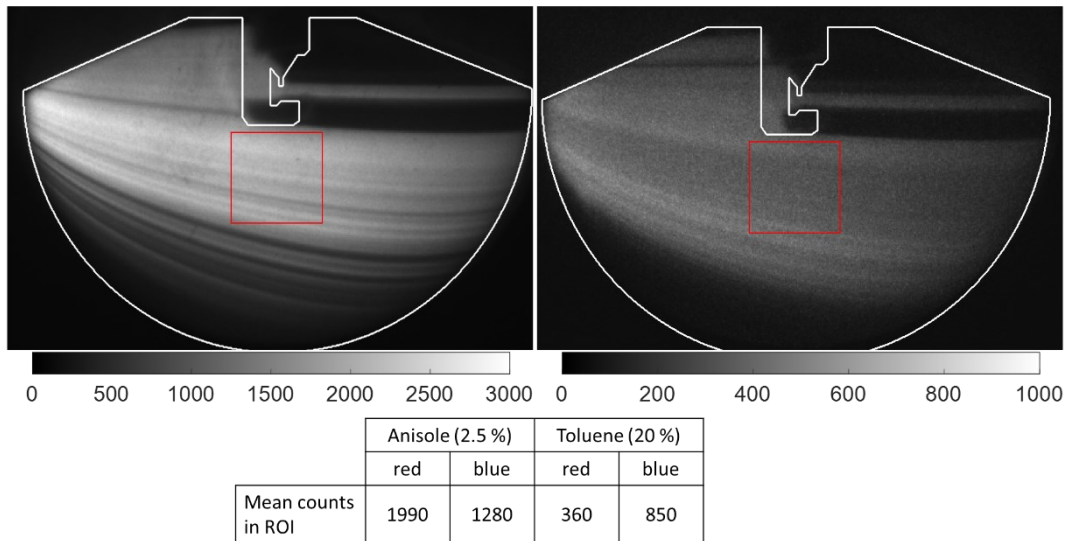


Figure 5.4: LIF images from red channel at -60°CA at the engine speed of 2000 min^{-1} and 75 Nm torque. Left: anisole. Right: toluene. Table shows the average counts in the red square.

Figure 5.5 shows anisole- and toluene- LIF single-shot images from the red channel at crank angles close to compression TDC. Anisole has much brighter LIF emission and therefore yields better image quality than toluene. Anisole-LIF images with 2×2 binning have approximately 4–5 times higher signal intensity than toluene-LIF images with same binning. Toluene-LIF images with 4×4 binning show similar intensity as anisole-LIF images with 2×2 binning, but the resolution of the images is worse and noise is also increased. Anisole-LIF images with 4×4 binning also have about 4 times higher signal intensity than toluene-LIF with 4×4 binning, but anisole-LIF images had much better image quality. With anisole, details in the wrinkled turbulent flame front burning into the mixture can be resolved, while with toluene at best the approximate location of the flame can be discerned.

The resolution of the imaging system is surprisingly good, as evidenced by the “stripes” that originate from flaws in the transverse beam profile and from beam steering in the flame front. A comparison of the ensemble-mean of the series (not shown) confirms that in fact attenuation is similar for the two tracers, as intended by the difference in concentrations. Overall, anisole appears to be a good candidate for LIF imaging in low-light applications such as endoscopic engines.

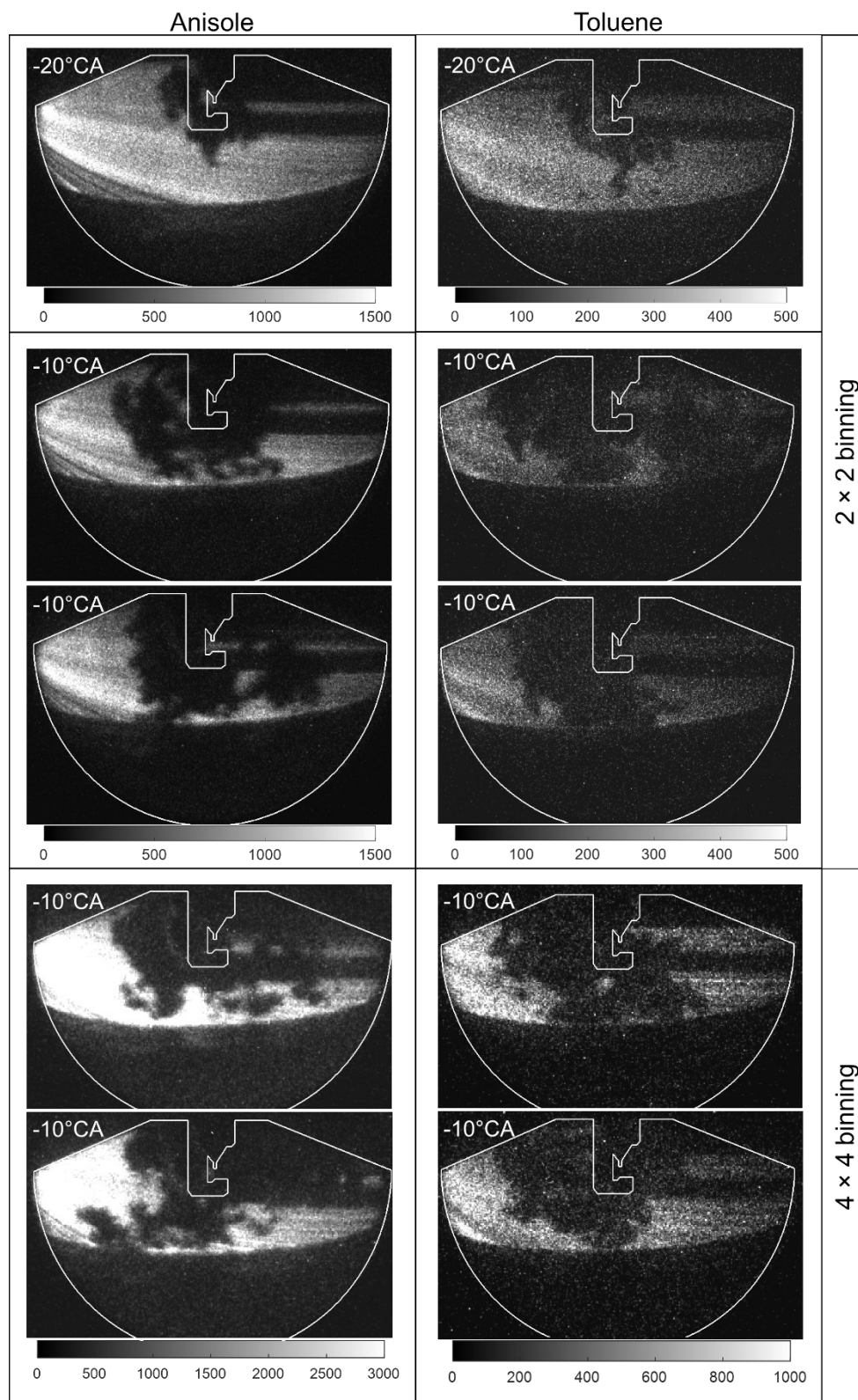


Figure 5.5: Single-shot images from the red channel of anisole- and toluene-LIF at different crank angles and different CCD binning. Engine speed = 2000 min^{-1} , torque = 75 Nm , ignition time = -34°CA . Anisole-LIF images at 4×4 binning are software-binned, the rest are hardware-binned.

5.4 Gas-phase temperature measurement

5.4.1 Spectroscopic model

Figure 5.6 shows peak-normalized anisole LIF spectra shifting towards longer wavelengths (red-shift) with increase in temperature and p_{O_2} [85]. The ‘red’ and ‘blue’ spectral regions that are used to determine the signal ratio are highlighted. This red-shift can be exploited to determine the temperature using two-color thermometry technique explained in section 2.1.2.1.

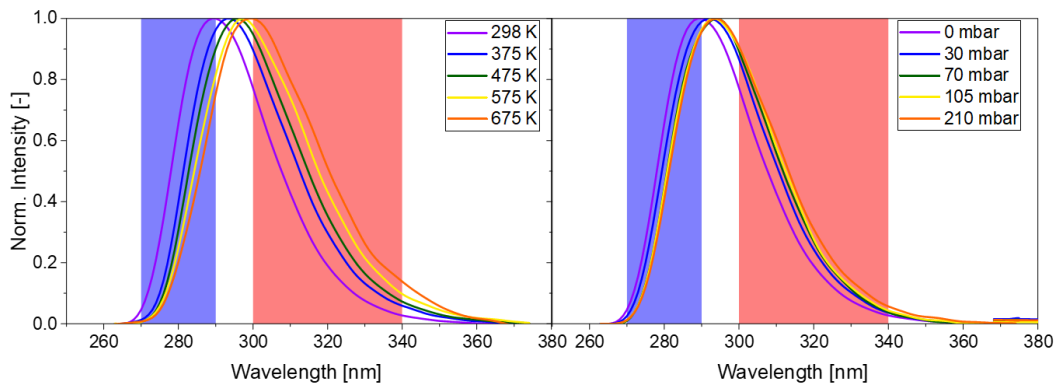


Figure 5.6: (left) Spectral shift of anisole spectra with temperature (in nitrogen) and (right) with p_{O_2} (at 296 K). Spectral data from [85].

The change between the red/blue signal ratio with temperature and p_{O_2} was determined by first estimating the expected LIF signals in each channel at different temperatures and p_{O_2} . The accurate estimation of expected signal in both channels requires considering the wavelength-dependent quantum efficiency of each detection channel, which includes the transmissivity of sapphire window and quartz lenses in the front endoscope, spectral response of the beam splitter to different wavelengths, transmissivity of band pass filters, as well as intensifier quantum efficiency. The effect of intensifier gain were assumed constant for both channels. Figure 5.7 shows the resulting convolution of peak-normalized anisole-LIF spectra with respective detection quantum efficiencies of red and blue channels at different temperatures with (a) air and (b) nitrogen as bath gases. Due to the red-shift of the anisole-LIF spectra with increasing temperature, the signals decrease in the blue channel and increase in the red channel, increasing the red/blue signal ratio.

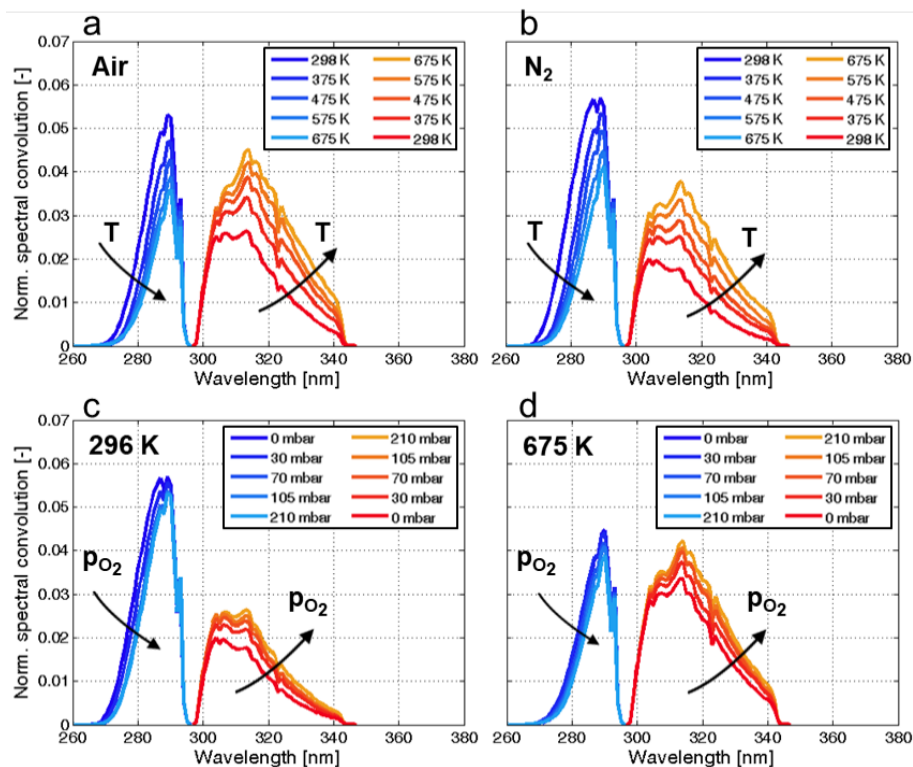


Figure 5.7: Convolved anisole spectra based on the normalized fluorescence spectra and filter transmission curves at (a) different temperatures in air (b) different temperatures in nitrogen (c) different p_{O_2} at 296 K (d) different p_{O_2} at 675 K [5].

Figure 5.7 (c) and (d) shows that, due to the red-shift of anisole-LIF spectra with increase in p_{O_2} , the signals decrease in the blue channel and increase in the red one with the increase in p_{O_2} , at room temperature (296 K) and at 675 K respectively. The consequent increase in red/blue signal ratio is stronger at lower p_{O_2} than at higher p_{O_2} . This effect is of particular importance at actual engine conditions, where p_{O_2} may be as low as 100 mbar in the intake stroke (based on about 20 % EGR) [92]. The signal in the red channel at 675 K is higher than at 296 K at the same p_{O_2} due to the red-shift of the anisole LIF spectra caused by an increase in temperature.

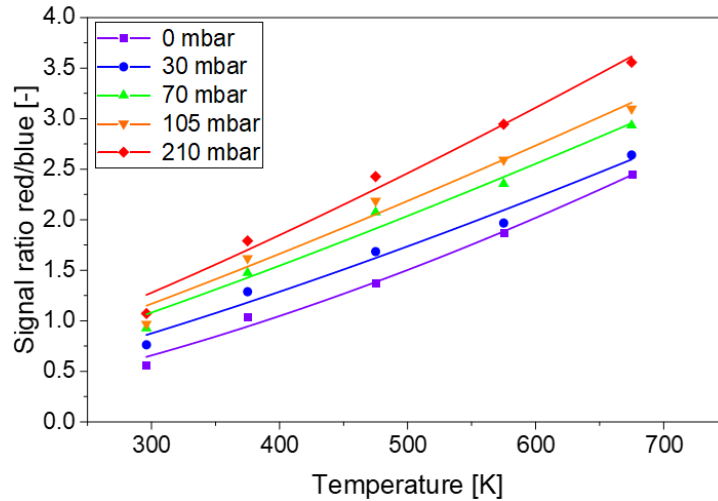


Figure 5.8: Spectroscopic signal-ratio model from measured anisole-LIF spectra at different p_{O_2} and temperatures [85].

Figure 5.8 shows the signal ratios estimated by spectral integration of anisole spectra at five temperatures, and five p_{O_2} . The discrete data points are fitted with an exponential-growth function given in Eq 5.1. The values of the coefficients a and b for calibrated data points are given in App 4 (see section 5.4.2 for calibration procedure).

$$y = ax^b \quad \text{Eq 5.1}$$

The choice of a suitable fitting function is not a trivial task. The available spectroscopic data has a smaller range than typical range of engine temperature (up to 1000 K) and p_{O_2} (upto 3000 mbar based on pressure traces during experiments). The deviations in the available data, such as the point at 30 mbar p_{O_2} and 575 K in Figure 5.8, render the interpolation based on a 3-parameter exponential function, as used by Kranz et al. [90], unsuitable. This is discussed in detail in section 5.4.3. Figure 5.9 shows how the signal ratio (red/blue) is affected by p_{O_2} . The points show the rearranged signal ratios from Figure 5.8, and the dashed lines represent the exponential decay fit function as described in Eq 5.2 below. The values of the coefficients a , b , and c for calibrated data points are given in App 5 (see section 5.4.2 for calibration procedure).

$$y = a + b \cdot \exp(cx) \quad \text{Eq 5.2}$$

$(a, b, \text{ and } c \text{ are constants, } c < 0)$

It is evident from Figure 5.9 that the effect of p_{O_2} is stronger at lower p_{O_2} and lessens with the increase in p_{O_2} . However, at higher temperatures, the saturation point of the curve is at

higher p_{O_2} , as shown by the slope at the end of the fitted curve at 675 K. Since higher temperatures are more relevant to engine conditions, the effect of higher than 210 mbar p_{O_2} becomes increasingly important to consider. The range of available data is small, and more data at higher p_{O_2} may yield a different fit function.

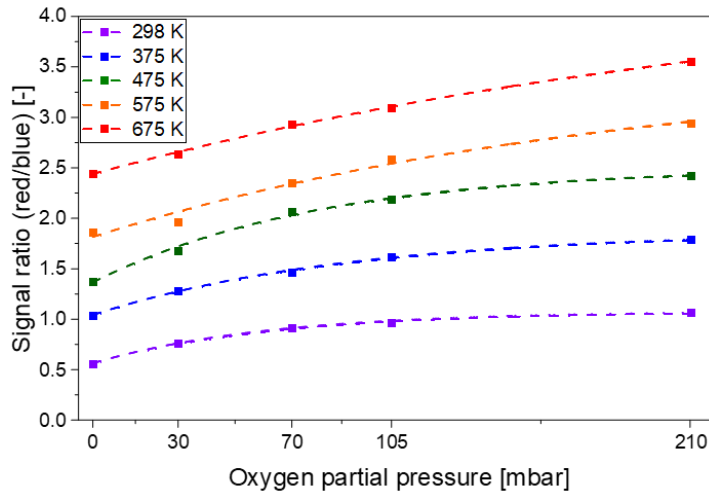


Figure 5.9: Effect of p_{O_2} on the signal ratio at different temperatures.

Since the signal ratios vary differently with temperature and p_{O_2} , the fit functions, both exponential but completely different, are combined using two different strategies.

1. 2D surface fit function
2. 2-step fit function

These are explained in detail in section 5.4.3.

5.4.2 Calibration

The signal ratios estimated at different temperatures and p_{O_2} are based on some assumptions which might change during experiments. This includes the angle of the beam splitter, similar response of both intensifiers at similar gain value, similar noise in both intensifiers and non-linearities in the intensifiers. That is why an in-situ calibration is needed. For this purpose, calibration measurements in the engine were performed at different temperatures with anisole seeded into two bath gases, air or nitrogen, i.e., 210 and 0 mbar p_{O_2} respectively. Tracer was added to the bath gas through a bubbler filled with anisole. The tracer concentration was not controlled since the signal ratio is independent of tracer concentration. The tracer-seeded bath gas was then passed through a heated quartz tube, with an exit diameter of 7 mm, via the spark-plug bore into the combustion chamber. The

temperature of the bath gases was measured by a thermocouple 5 mm downstream of the tube exit and was controlled by varying the voltage supplied to the heater by a DC power supply. The gases were supplied at the pressure of 1 bar pressure and flow rate of $2.8 \times 10^{-4} \text{ m}^3/\text{s}$. The Reynolds number at the nozzle exit was approximately 3200 (transition regime).

Since the shot noise in the background was changing in each image, a dynamic background subtraction strategy was used. One method used for dynamic background subtraction is to use SLIPI (structured laser illumination planar imaging) [93, 94] method by placing Ronchi gratings in front of the light sheet endoscope. However, this was challenging due to the physical limitations of endoscopic imaging. Also, the strong vertical divergence of the laser beam would make the computations difficult. Three methods were compared, which are:

- a) Background subtraction from thermocouple-blocked region
- b) Illumination by the “point endoscope” (see section 3.3.2)
- c) Background subtraction from a wire-blocked region

These methods are referred to as thermocouple-blocked, point endoscope, and wire-blocked in the following text. Figure 5.10 shows the blue channel images from the three methods. The black box in each image represents the ROI for measuring the averaged signal and the red box for averaged dynamic background. The ROIs are called signal ROI and background ROI in the following discussion. In the first method, a region behind the quartz tube was shadowed by ca. 2 mm thick thermocouple wire, and the background was obtained by averaging a 50×50 pixel area in the shadowed region. The assumption in this method is that the tracer/bath gas mixture was at the same temperature throughout the whole combustion chamber. To ensure this, the tracer/bath gas mixture was allowed to flow for approximately 1 minute at each temperature before recording the images. In the second method, the point endoscope (see section 3.3.2) was used. This endoscope was positioned so that one beam of laser passed through the space between the tube exit and thermocouple tip. This method enabled extracting the background from the region close to the signal ROI, which means that the temperature of the jet would be the same in both signal and background ROIs and, therefore, the temperature-dependent component of the background could be measured effectively. In the third method, a region directly below the signal ROI was shadowed by a wire placed behind the laser light sheet endoscope. The background was obtained by averaging a 50×50 pixel region from the shadowed region as shown in Figure 5.10.

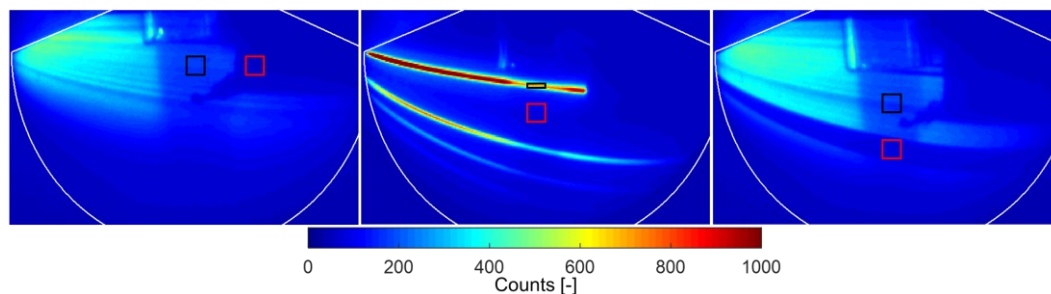


Figure 5.10: Blue channel images from three calibration methods. Left: Thermocouple-blocked. Center: Point endoscope. Right: Wire-blocked. Black square represent ROI for signal integration, red for BG.

Figure 5.11 shows the signal ratios obtained by the three calibration methods at different temperatures. With air as the bath gas, the signal ratios obtained by the three methods were similar at lower temperatures, but signal ratios from the thermocouple-blocked method deviated at higher temperatures. With nitrogen as the bath gas, wire-blocked and point endoscope method yielded similar signal ratios, and the deviation of the signal ratios from thermocouple-blocked method became larger at higher temperatures.

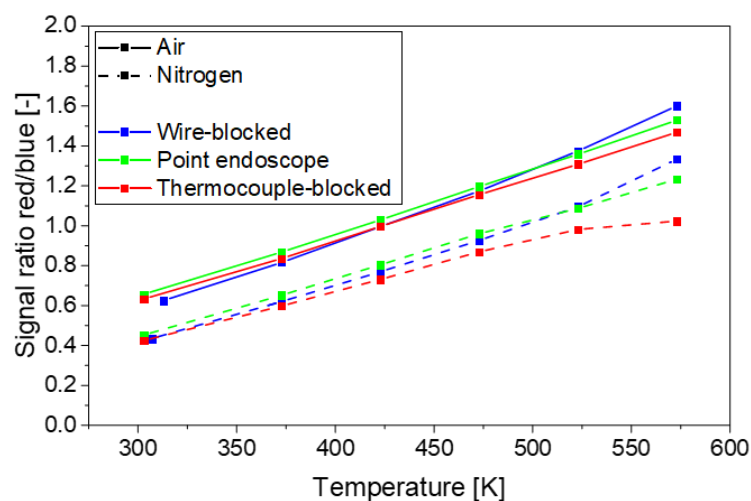


Figure 5.11: Signal ratios from different calibration methods at different temperatures.

In previously reported works, the signal ratio increase exponentially with temperature in any bath gas [81, 91, 95]. Here, in the calibration measurements, the signal ratios decrease because the fluorescence signals are extremely low at higher temperatures, and therefore an unsuitable dynamic-background subtraction can significantly and incorrectly alter the signal ratios. Therefore, another important parameter for selecting the suitable calibration method is the signal-to-noise ratio (SNR) of the fluorescence signals, especially at higher temperature.

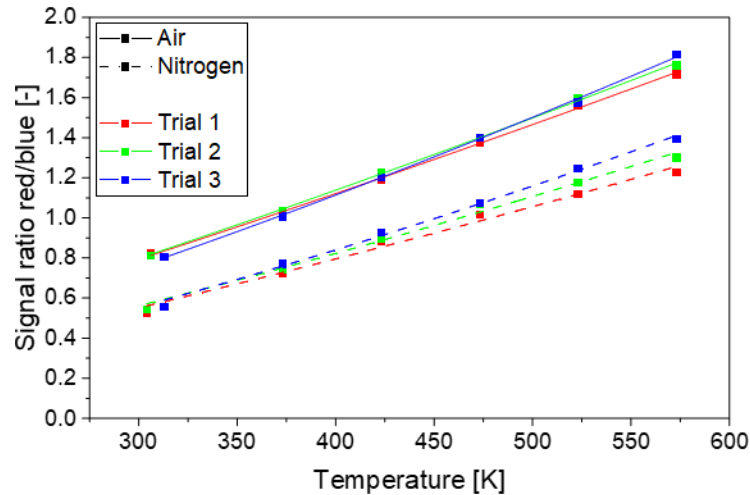


Figure 5.12: Three calibration measurements using the point endoscope.

Among the three methods, the point-endoscope method had the highest SNR at higher temperatures. Therefore, this method was chosen for calibration. Three measurements were performed, and unseeded air was allowed to flow through the combustion chamber between each measurement for at least 30 minutes to ensure complete flushing and cooling the cylinder. Care was taken to keep the optical setup the same for the calibration measurements and the engine runs. The measurements were performed in forward and backward direction (increasing and decreasing temperature), and the values of signal ratios at each temperature were ensemble averaged and shown in Figure 5.12. The points show the signal ratios obtained at different temperatures, and the lines are the fit according to the Eq 5.1. The three measurements with air as bath gas were similar, and only showed a small relative standard deviation of 2 % at 573 K, which corresponds to a deviation of 11 K. On the other hand, the calibration measurements with nitrogen as the bath gas showed higher relative standard deviation of 5.3 % (30 K). It was found that small amounts of air were occasionally introduced through the spark plug hole, probably because of higher ambient pressures caused by malfunctioning ventilation, resulting in higher deviations in calibration measurements with nitrogen as the bath gas.

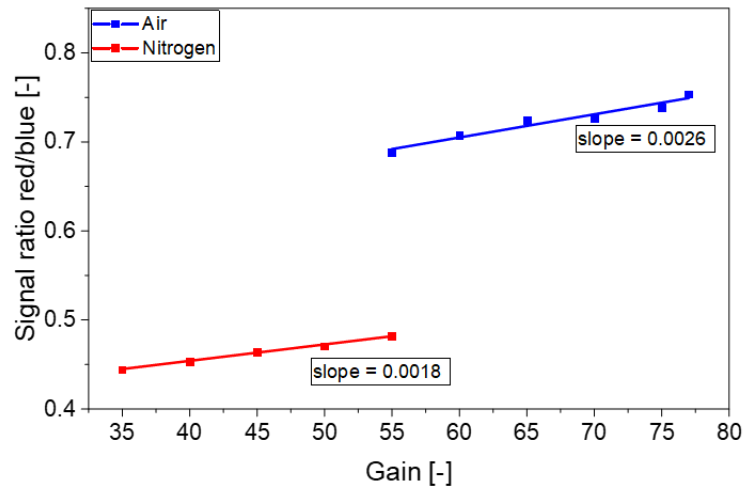


Figure 5.13: Effect of intensifier gain on the signal ratio.

In another experiment, the effect of intensifier gain on the signal ratio was investigated. It was suspected that the quantum efficiency of the intensifier at different values of gain is not the same, and thus the signal ratio might change with a change in gain value. This is important since the calibration measurements and the measurements in the running engine are performed at different gain values. The measurements were performed with anisole seeded separately into both air and nitrogen as bath gases. The flow conditions were similar to those for the other calibration measurements. With nitrogen as the bath gas, gains of 35 to 55 were selected with a step of 5, and with air, 55 to 75 and one final measurement at the gain of 77. The results are shown in Figure 5.13. It was found that the intensifier gain indeed affects, apparently linearly, the signal ratios. The slope of the linear fits to both measurements was similar. Therefore, the ensemble averaged signal ratios from the three calibration measurements were corrected for the difference in the gain between calibration measurements and the measurements in the running engine using an average value of the slope, i.e., 0.002.

Figure 5.14 shows the averaged and gain-corrected averaged signal ratios for the calibration measurements. The points show the measurements, and the lines represent an exponential fit according to Eq 5.1. Since calibration measurements with nitrogen as bath gas were performed in the lower gain range of 35–55, the signal ratios were more affected by correcting for the gain difference in the calibration and engine measurements.

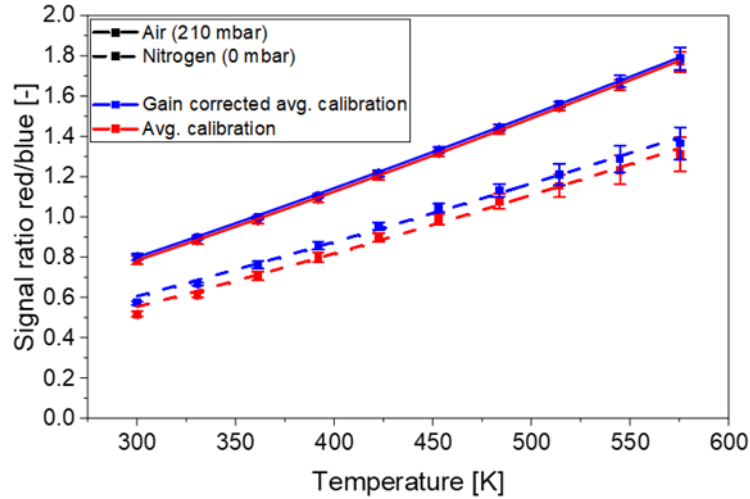


Figure 5.14: Signal ratios from the calibration measurements before and after correcting for the difference in gain between calibration and engine measurements.

The gain-corrected averaged signal ratios from the calibration measurements as shown in Figure 5.14 were used to calibrate the spectroscopic signal model shown in Figure 5.8. A calibration function was found by trial and error considering different pre-factors and orders of dependencies. The factors tried were signal ratio, p_{O_2} , temperature and their products. The final ad-hoc calibration function is a combination of a constant offset, second-order dependency on the signal ratio, and a first order dependency on the product of signal ratio and temperature.

$$SR_{calibrated} = 0.44 + 0.16 \cdot SR - 0.039 \cdot SR^2 + 0.000705 \cdot SR \cdot T \quad Eq 5.3$$

where

SR	Signal ratio
T	Temperature [K]

The signal model obtained from spectroscopic data, and the calibrated signal model after applying Eq 5.3 are shown in Figure 5.15. The signal ratios are fitted with the exponential function given by Eq 5.1. The signal ratios obtained from the calibration measurements are shown as black lines encompassing the calibrated signal model. The calibrated signal ratios are much lower than the signal ratios obtained from the spectroscopic data showing the necessity of an in-situ calibration for accurate application of two-color thermometry. The calibrated model shows very good agreement with the calibration data. But there are slight deviations at higher temperatures that are shown later.

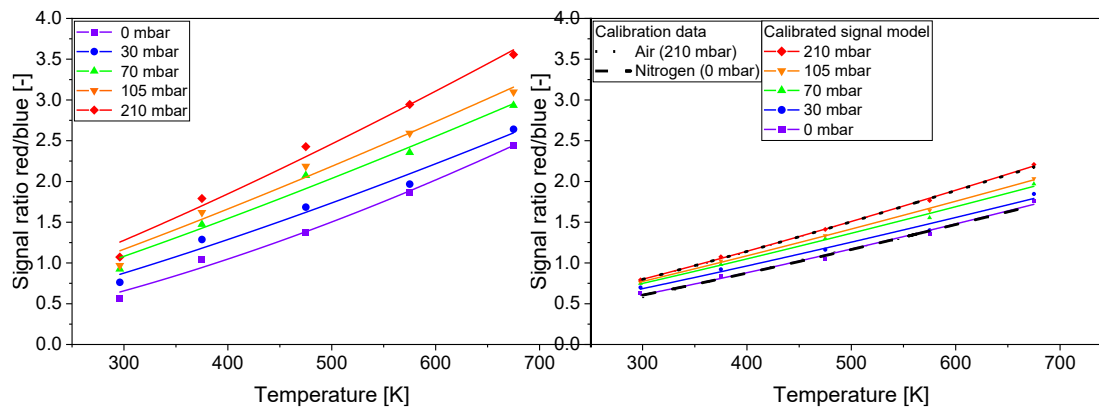


Figure 5.15: Calibration of the signal model. (Left) Signal model from the spectroscopic data. (Right) Calibrated signal model and calibration data.

5.4.3 Extrapolation of calibrated signal model

The calibration data, as shown in Figure 5.15 (right) are limited to 210 mbar p_{O_2} and a temperature of 675 K whereas in the measurements in the running engine, the p_{O_2} is as high as 3 bar, and the temperature up to 1000 K. Therefore, the calibrated model must be extrapolated. Two different strategies were adopted for this extrapolation.

5.4.3.1 2-step fit

As discussed in section 5.4.1, the signal ratios follow a (saturating) exponential trend w.r.t. p_{O_2} (Figure 5.9), and an exponential fit function describing the trend is given in Eq 5.2. On the other hand, the signal ratio increases exponentially with temperature, and one possible correlation to describe the trend is given in Eq 5.1. In order to increase the range of the signal model, first, five saturating exponential fit functions, as shown in Figure 5.9, were extracted in MATLAB (see App 5 for values of coefficients). These functions describe how the signal ratios change with p_{O_2} at five different temperatures and were used to generate a discretized data set of signal ratios up to 3000 mbar p_{O_2} at five temperatures, with increments of 1 mbar. This is shown in Figure 5.16.

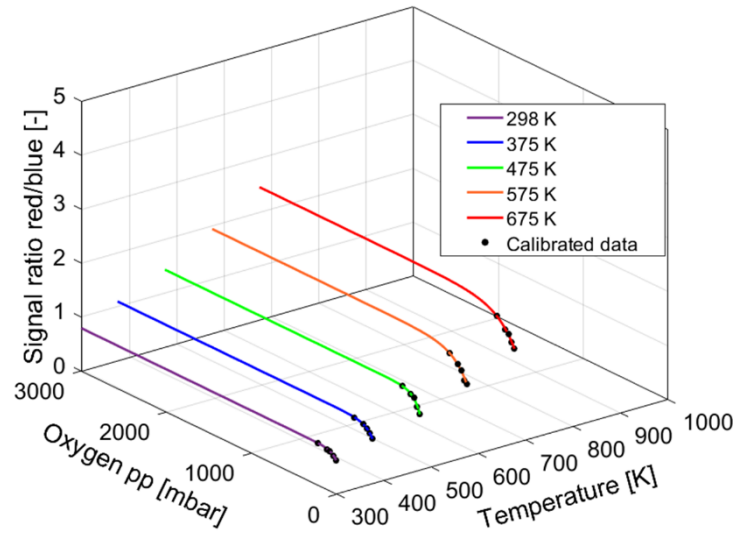


Figure 5.16: Effect of p_{O_2} on signal ratio extrapolated up to 3000 mbar.

In the second step an exponential growth fit function, as given in Eq 5.1, is determined for any given value of p_{O_2} . This means that a new fit function will be determined for each image based on the corresponding value of p_{O_2} , which requires less computational resources because 3000 fit functions for every value of p_{O_2} do not to be kept in memory. Each exponential growth fit function originally has temperature as dependent and signal ratio as independent variable. However, the equation is later rearranged to determine the temperature from the signal ratio at a given p_{O_2} . In order to visualize the evolution of the signal model, the fit functions for each value of p_{O_2} were determined and plotted up to a temperature of 1000 K in 10 K steps as shown in Figure 5.17. Note that the exponential functions at p_{O_2} have stronger increase compared to the ones at lower p_{O_2} .

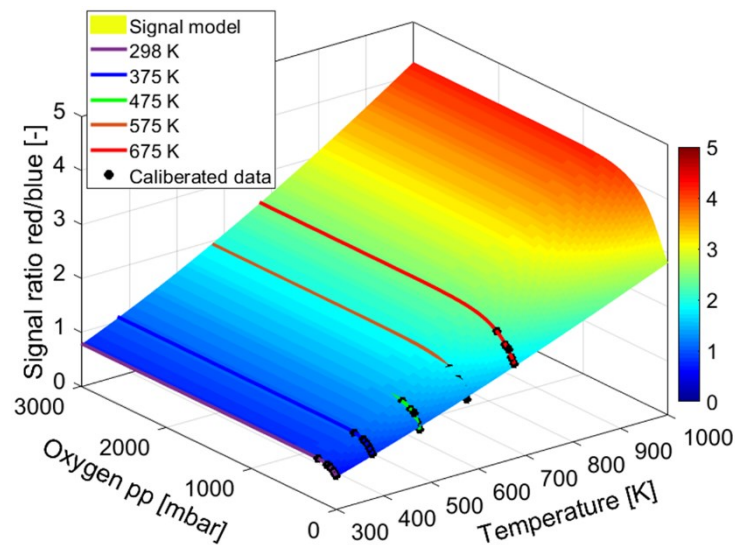


Figure 5.17: Effect of temperature and p_{O_2} on signal ratio based on 2-step extrapolation.

In order to compare different approaches, the exponential growth function were replaced by a linear function, and alternatively a 3-parameter exponential function as used by Kranz et al. [89]. The signal models using these two functions are shown in Figure 5.18. Compared to the model shown in Figure 5.17, the model with the linear fit has lower signal ratios towards the high p_{O_2} and high temperature region, while the model with 3-parameter exponential function has higher ratios in this region. The model with 3-parameter fit function is distorted in low p_{O_2} and high temperature region due to some irregular trend in the signal ratios obtained from the spectroscopic data at 30 and 70 mbar p_{O_2} . However, this distortion does not influence the results because in engine operation, the crank angles in the compression stroke that have high temperature also have high p_{O_2} and none of the data points from the measurement would lie in the distorted region. The results are calculated using these three methods in section 5.4.5.1 and compared.

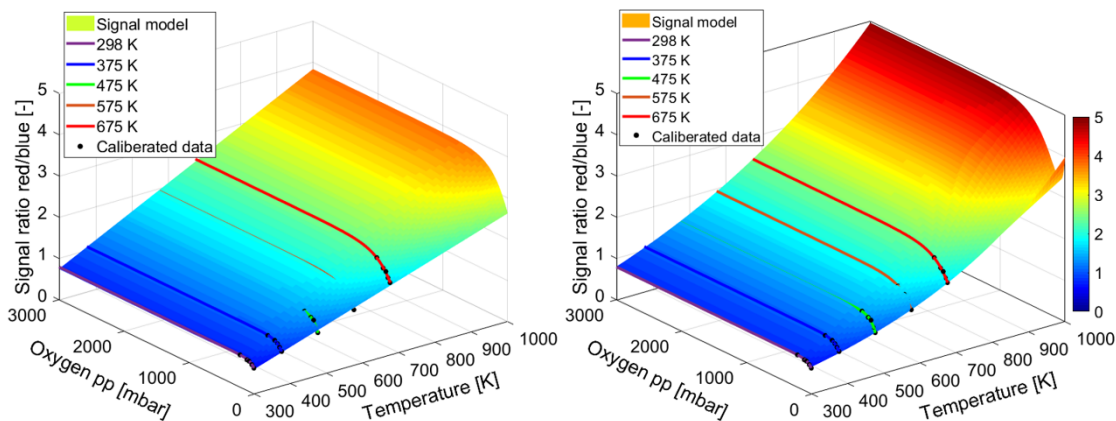


Figure 5.18: 2-step signal models based on linear (left) and 3-parameter exponential (right) dependency of the signal ratio on temperature.

5.4.3.2 3D surface fit

In this method, a single surface-fit function was determined instead of two different functions for the effects of p_{O_2} and temperature on the signal ratio. The equation for the surface fit (Eq 5.4) was formulated by combining Eq 5.1 and Eq 5.2. The surface fitting was performed in MATLAB, and the result is shown in Figure 5.19. The values of the coefficients a , b , c , d , and f for calibrated data points are given in App 6 (see section 5.4.2 for calibration procedure).

$$SR = (a + b \cdot \exp(cy)) \cdot (dx^f) \quad \text{Eq 5.4}$$

where

	$a, b, c, d,$ and f are constants, $c < 0$
SR	Signal ratio
x	Temperature [K]
y	Oxygen partial pressure, p_{O_2} [mbar]

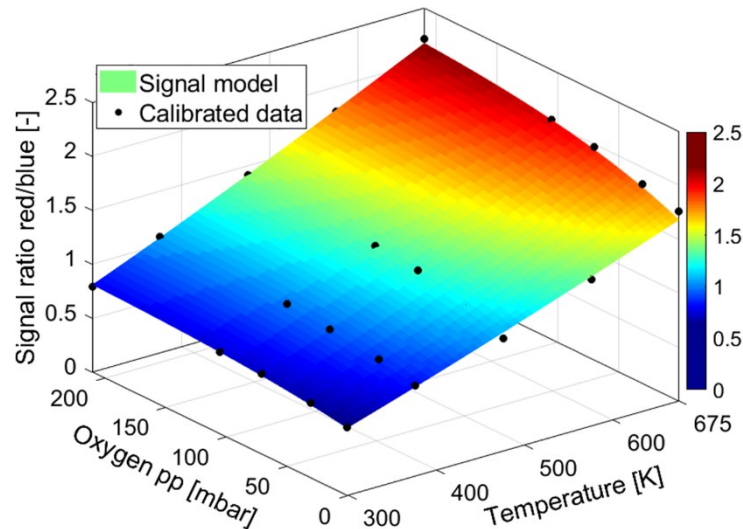


Figure 5.19: 3D surface fit of the spectroscopic data. The black points represent the data points from the spectroscopic data, and the surface is the signal model based on the surface fit.

To visualize the behavior of this surface-fit function, the function was evaluated over a similar range as the 2-step models and is shown in Figure 5.20. The exponential rise of the temperature-dependent signal-ratio in the higher temperature region was dampened in this case. Although part of the surface fit equation (Eq 5.4) governing the temperature-dependent rise is exponential in nature, the simulated surface is similar to the 2-step interpolation with linear temperature dependence (see Figure 5.18). In an attempt to replace the 2-parameter temperature-dependent part of the surface-fit equation (dx^e) with a 3-parameter exponential function ($d + e \cdot \exp(fy)$), the fit did not converge. A linear temperature-dependent function also resulted in a very similar surface as in Figure 5.20, and is therefore not included here.

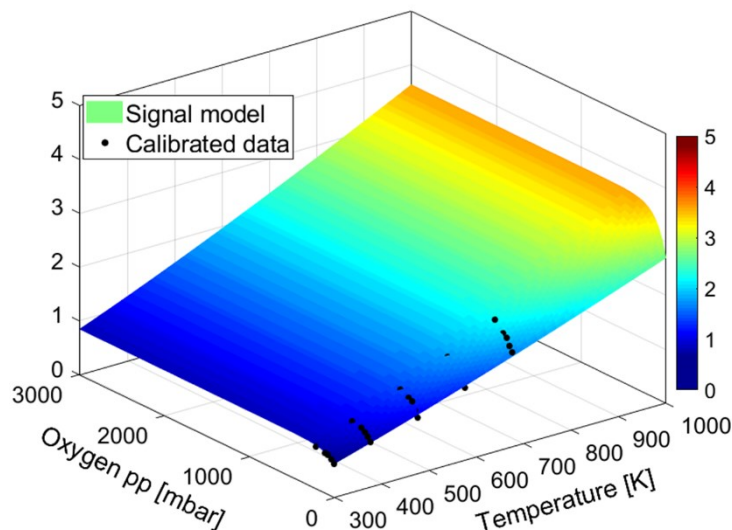


Figure 5.20: Extrapolated 3D surface fit based on Eq 5.4.

Contrary to the 2-step fit function method, here, a new fit function is not determined for every p_{O_2} . Instead, a single equation (Eq 5.5) is formulated by rearranging the equation of the surface fit, and the temperature is calculated from the values of signal ratios and p_{O_2} .

$$x = \exp\left(\frac{1}{f} \cdot \ln\left(\frac{SR}{d \cdot (a + b \cdot \exp(cy))}\right)\right) \quad \text{Eq 5.5}$$

where

	$a, b, c, d,$ and f are constants, $c < 0$
SR	Signal ratio
x	Temperature [K]
y	Oxygen partial pressure, p_{O_2} [mbar]

5.4.4 Images and post-processing

The images were first registered in DaVis with a UV-illuminated target that was mounted on the detection endoscope replacing the field lens. The target registration with the engine is not simple. The engine slightly shifts relative to the optical system under the load in the running condition, therefore the target registration cannot completely account for the relative difference between the images captured by two cameras. Therefore, the remaining error in registration was corrected in MATLAB, as shown in Figure 5.21. A simple vertical translation of blue image by 3 pixels was sufficient to get rid of the “high signal-ratio zones” resulting from the insufficient registration.

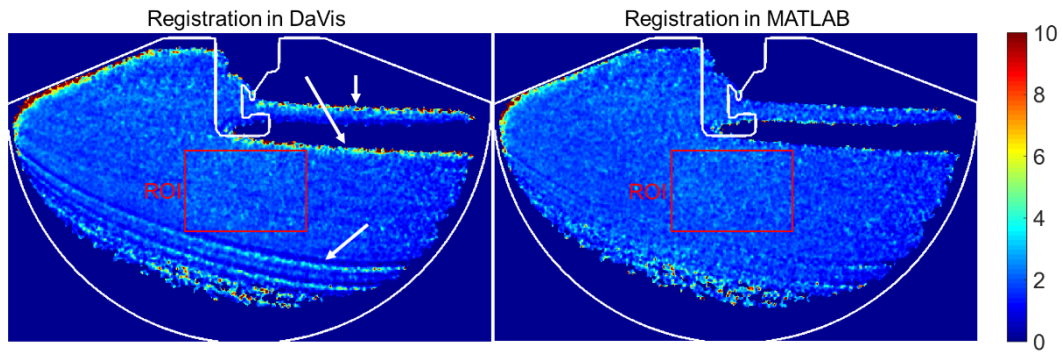


Figure 5.21: Red/blue ratio images at -40°CA bTDC. (left) Registration performed in DaVis only. (Right) Additional registration performed in MATLAB. ‘excessive-ratio zones’ caused by inaccurate registration, labeled in the left image by white arrows, disappear after additional manual registration in MATLAB.

Figure 5.22 shows the image post-processing steps to extract the signal ratios for each image at all crank angles. After registration, the regions outside the field-of-view and, where applicable, those blocked by the piston are masked out. The dynamic background was then subtracted from each image by averaging a 30×100 pixel area from the shadowed region behind the spark-plug ground electrode. The next step was essentially to suppress the ‘burnt area’ at later crank angles, where the signals are only background. To achieve this, a flatfield was obtained by averaging all the images obtained at each crank angle, and single-shot images were divided by the flatfield image to partially correct for laser absorption. If this flatfield-correction is not performed, binarizing by simple thresholding would also eliminate some ‘useful’ regions extreme downstream that have low signal. The flat-field corrected images were then smoothed by a 5×5 mean filter, normalized by the maximum count value and binarized by thresholding at 18 % of that maximum count value. This binarizing process eliminated all of the burnt-gas and unilluminated regions. The binary image was then multiplied with the original images, without 5×5 mean filtering and flatfield correction, from both channels and 3×3 mean filtering was applied to reduce the noise. The image from the red channel was divided pixel-wise by the image from the blue channel. The average signal ratio was determined by averaging just the non-zero pixels in a 100×150 pixel ROI below the spark plug, as shown in the Figure 5.22. If the number of non-zero pixels in the ROI filled less than 25 % of the ROI, as could be the case at later crank angles with larger burnt regions, the results were discarded. This resulted in 100 values for signal ratio crank angles before and right after ignition, and less values as the flame propagated. At TDC, only 9 out of 100 images could be used to obtain a value for signal ratio. The whole process was robust and used for all crank angles.

The average signal ratios for each image were further averaged at each crank angle, which was used in combination with the averaged p_{O_2} at that crank angle to calculate the temperature. The divided images are also converted into temperature images by calculating temperature for each pixel assuming a constant p_{O_2} throughout the field of view. In addition to signal ratios for each image at all crank angles, the mean and standard deviation of pixel values in the ROI was also determined for BG-subtracted red and blue images, and for the divided images.

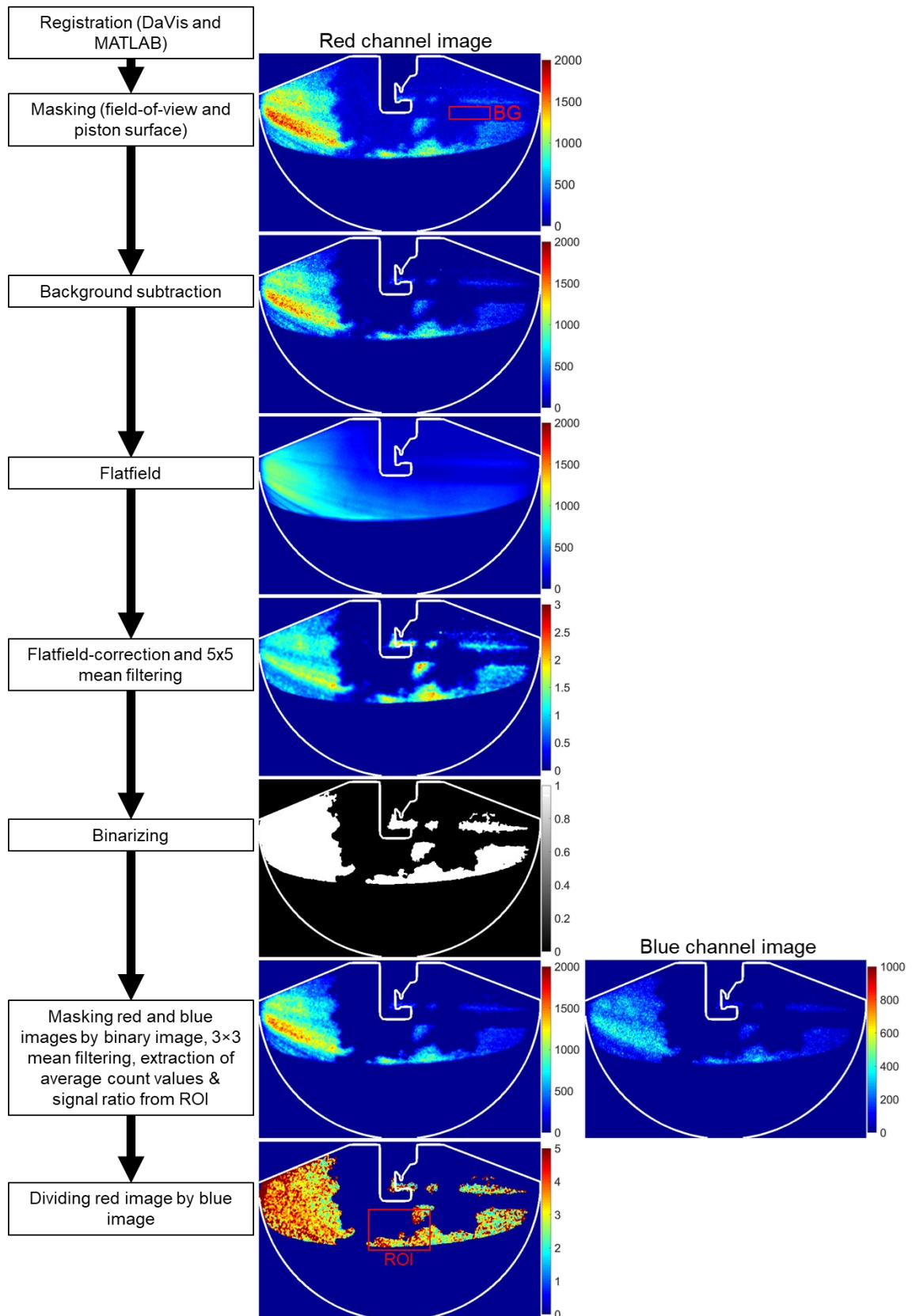


Figure 5.22: Image post-processing steps.

5.4.5 Results

5.4.5.1 Temperature variation during the compression stroke

Figure 5.23 shows the temperature progression throughout the compression stroke measured by two-color LIF thermometry using different signal models compared to the adiabatic temperature. The results show that both of the 3D surface fits much over calculated the temperature. The temperature at the start of compression stroke (-180°CA), as calculated by the 2-step fit model with 2-parameter exponential temperature-dependent part, is 322.5 K. One approximation to determine the in-cylinder gas temperature at IVC (-173°CA) is averaging the temperatures of intake air and cooling water, i.e., 309 K and 383 K (see Table 5.2) respectively, resulting in an estimated temperature of 345.6 K, whereas the temperature measured at this crank angle is ~ 325 K. However, since the measured temperature lies within the range of in-situ calibration, which was repeated multiple times, the accuracy of the measured temperature is likely.

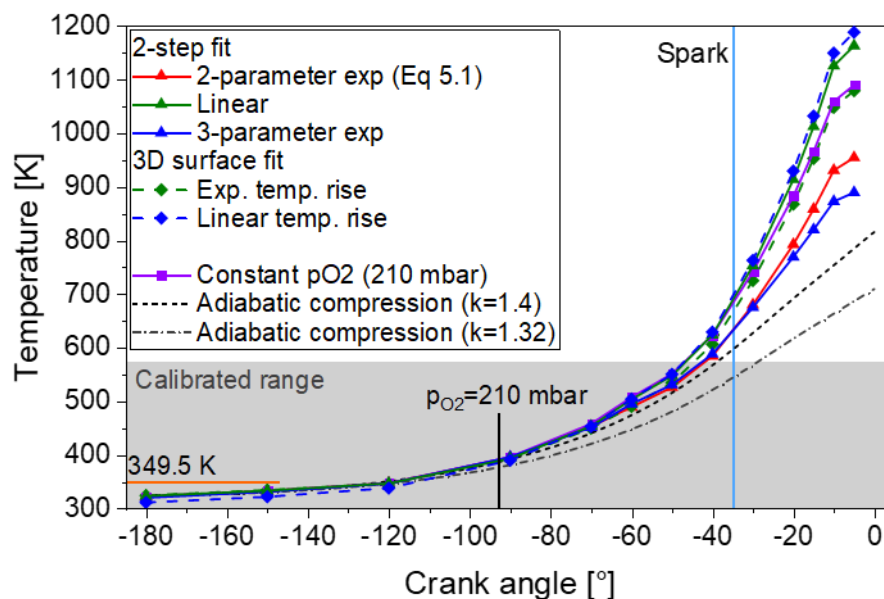


Figure 5.23: Temperature in the compression stroke with various signal models compared to the adiabatic temperature. The legend entries describe the temperature-dependant part of the signal model. The p_{O_2} -dependent part of all signal models was same as in Eq 5.2.

The measured temperature in the first half of the compression stroke is similar for all the investigated models and is in a good agreement with adiabatic temperature ($\kappa = 1.4$). This value of κ is used here for comparison as the measured temperatures represent the ‘core temperature’ which is near-adiabatic [96], as opposed to the ‘bulk temperature’ for which

a consolidated value of $\kappa = 1.32$ is used [97]. In the following text, ‘adiabatic’ refers to this core temperature. In theory, the measured temperatures should be close to the adiabatic temperature until ignition (-35°CA in this case) and will deviate afterwards due to additional heat addition from the combustion. However, Figure 5.23 shows that when p_{O_2} reaches 210 mbar, the measured temperatures start deviating from the adiabatic temperature. The degree of deviation is different for each model. However, at ignition the 2-step fit models with exponential temperature-dependent part have the lowest deviation (~ 35 K) from the adiabatic temperature. The 3D surface-fit models, although seemed convenient, show a deviation of 70 and 100 K for the models with exponential and linear temperature-dependent part respectively. The model with p_{O_2} assumed constant (210 mbar) throughout the compression stroke also showed a deviation of about 84 K at ignition.

Due to lowest deviation, and the fact that previous studies have reported that signal ratio increases exponentially with the temperature, the 2-step fit function with 2-parameter exponential temperature-dependent part was chosen for further evaluation. Figure 5.24 shows the measured temperature evaluated with this method compared to adiabatic temperature. The error bars show the fluctuations in the measured temperature, calculated as the standard deviation of the measured temperatures at each crank angle. Evidently, the temperature fluctuations are small at all crank angles before ignition and start increasing afterwards owing to cycle-to-cycle variations. It is clearer in Figure 5.24 that the measured temperature starts deviating from adiabatic temperature just after the p_{O_2} in the cylinder rose above 210 mbar. Although the deviation before ignition is small, it is likely that if the spectroscopic data were available for higher p_{O_2} , the correlation between p_{O_2} and signal ratio could be estimated more accurately and the deviation between measured and adiabatic temperature would decrease. The same can be said about spectroscopic data for higher temperatures, so that a more accurate exponential fit function could be used.

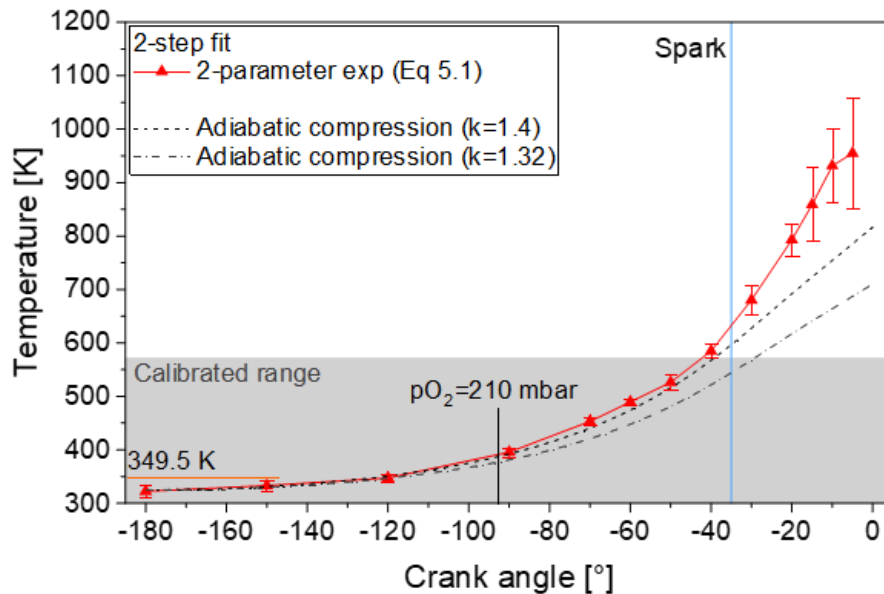


Figure 5.24: Measured temperature evaluated with 2-step fit model with 2-parameter exponential temperature-dependent part. The point shows the mean measured temperature, and the error bars show the standard deviation over the complete data set at each crank angle.

5.4.5.2 Temperature distribution: Compression stroke

Figure 5.25 shows single-shot images of the spatial temperature distribution at different crank angles during the compression stroke. The temperature at the start of compression stroke is generally uniform throughout the FOV. Some deviations can be seen in the upper left corner close to the intake valve, in some stripes in the lower region, and around the spark plug. These are probably due to remaining errors in the registration procedure. However, these are outside of the ROI used for calculating the mean core temperature at each crank angle. The higher temperature around the spark plug is probably correct since the spark plug would be at higher temperature and conduction may have resulted in higher temperatures close to the spark plug. This is consistent with the work by Kranz et al. [89]. The temperature appears to be more uniform at later crank angles, although the SNR decreases.

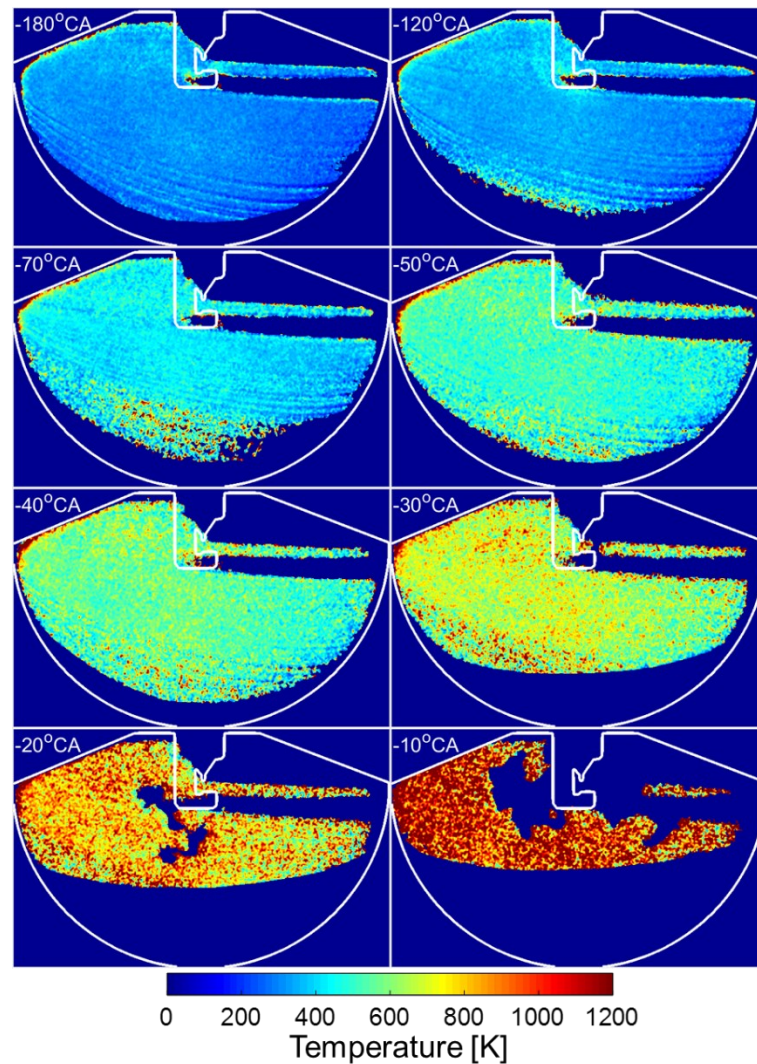


Figure 5.25: Temperature images at different crank angles during the compression stroke.

5.4.5.3 Gas exchange

Two-color LIF thermometry was utilized to visualize the possible temperature stratification during the gas-exchange process. The 2-step fit with 2-parameter temperature dependent part was used to determine the temperature. The results are shown in Figure 5.26. Here, 360°CA represents the gas-exchange TDC and 380 and 400°CA represent the intake stroke of the following cycle. The phenomena observed with anisole LIF are similar to what was observed with toluene LIF in previous work on the same test bench by Gessenhardt et al. [58], in which it was determined that at this operating point the combustion efficiency is 97.9 %, and the signals appearing at crank angles late into the exhaust stroke are mostly due to unburnt gases, or other aromatic combustion products with spectral properties similar to those of toluene. In this work, the temperatures for these gases

were determined assuming that the signals come from unburnt anisole or aromatic compounds with similar properties. At 340°CA, unburnt residuals appear in the region close to the intake valve with temperatures around 450 K, with some cooler regions probably due to small amount of fresh charge. At 360°CA, the unburnt residuals appear to move to the right with slightly higher temperature. At 380°CA, a clear temperature stratification is observed, with fresh charge being at much lower temperature compared to exhaust gases ahead. The temperature of the residual gas has increased at this crank angle. The reason for this increase in temperature is back flow of exhaust gases from the still open exhaust valve at this crank angle [4], which are at even higher temperature of 607 K. The fresh charge also appears to be at higher temperature than the intake air temperature of 309 K (see Table 5.2), probably because there is conductive heat transfer from the hot engine components and some mixing between residual gases and the fresh charge. At 400°CA, the temperatures of the ‘cooler’ fresh charge and ‘hotter’ residual gases have decreased because more amount of fresh charge has entered the cylinder resulting in overall decrease in temperature. This also support the accuracy of the temperature measured at BDC (start of compression stroke), since the temperature is showing a decreasing trend towards the temperature of the fresh charge (309 K). Apart from this decrease in temperature caused by fresh charge, additional cooling can be expected from the gas expansion due to lower pressures in the cylinder.

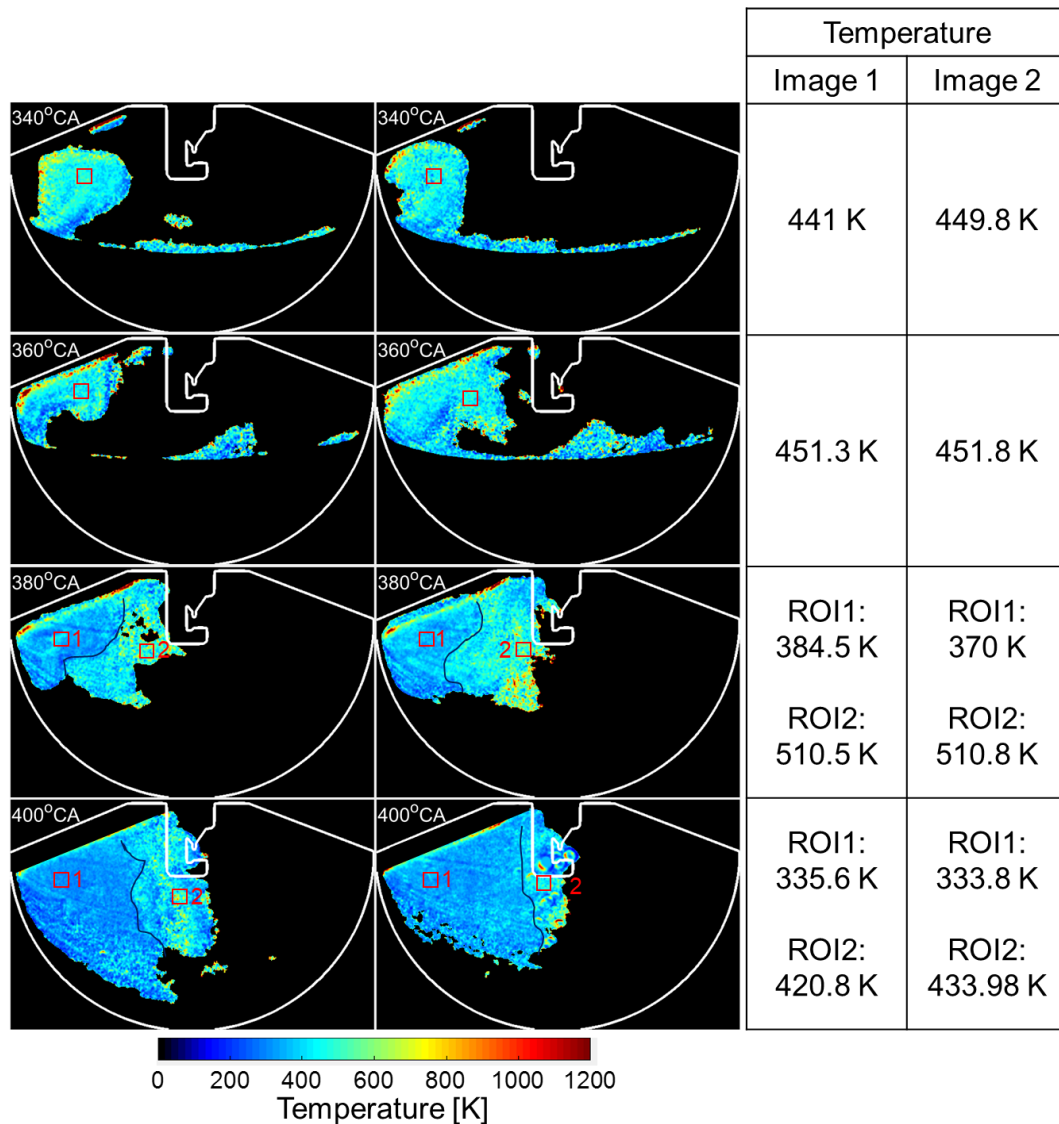


Figure 5.26: Spatial temperature distribution during gas exchange. The red squares represent the ROIs to determine the mean temperature. The blue lines represent the apparent boundary between the fresh charge and the residual unburnt gas from the previous cycle.

5.5 Experimental challenges

The application of two-color thermometry on an all-metal engine with endoscopic access is very promising, as in-cylinder temperatures can potentially be determined in a realistic speed-load range. However, this proved to be a very challenging task. The problems encountered during the experiments are summarized below to show the possible challenges in applying similar laser-based diagnostics endoscopically.

5.5.1 Laser

Sufficient laser energy, and a uniform and repeatable profile is beneficial for any laser-based diagnostic technique. However, introducing the laser into the cylinder via 5×5 mm lenses limits the energy that can be transmitted without damaging the lenses. This is especially crucial for the off-center cut plano-concave lenses in the illumination endoscope, whose production is expensive and time-intensive. One way to transmit more energy is using a pulse stretcher, which decreases the instantaneous power of the laser pulse by extending the pulse duration. A single-cavity pulse stretcher loop [98] was in fact tried, but it greatly increased the alignment sensitivity of the whole laser system. The pulse stretcher was mounted on a frame that also housed the Nd:YAG laser, and was not as rigid as an optical table. A small disturbance in the alignment of pulse stretcher components resulted in severe misalignment at the exit of laser guiding arm. The laser guiding arm and geometry of the micro lenses in the illumination endoscope limited the effective laser beam diameter to 5 mm. In previous work [5, 88, 99], the laser beam was clipped by an aperture to a diameter of 5 mm, choosing the ‘best’ part of the beam profile. Due to reduced overall laser energy over the years, a Galilean telescope with a magnification of 0.5 was used to reduce the diameter of the beam instead of clipping. The telescope further increased the alignment sensitivity, and it was observed that the beam profile was compromised and the risk of misalignment due to engine vibrations during the experiments was increased. For similar experiments, it is highly recommended to use a pulse stretcher mounted on an optical bench. The base plate of the laser guiding arm should be mounted on a frame that is sufficiently vibration-isolated.

5.5.2 Engine

The condition of the engine used in this work had deteriorated over the years. One problem encountered during this work was significant amount of engine oil leaking into the cylinder and covering the sapphire windows, thus blocking the optical access for both illumination and detection. Upon combustion, the engine oil leaves a residue on the windows, which would render the optical measurements impossible. Repair attempts included replacing the engine head gasket and valve stem seals. The leakage was reduced by replacing these items, but not completely eliminated. The engine block and the cylinder head may have to be resurfaced to ensure proper sealing between the oil jacket and the cylinders and the piston

rings may have to be replaced with new ones to prevent the seepage of engine oil into the cylinder.

The engine has a rated output of 200 Nm at 3750 min⁻¹, while the dynamometer can only hold a maximum of 90 Nm. The resulting continuous low-load operation prevented the so-called 'self-cleaning' of the engine deposits mainly consisting of soot coming from the combustion of engine oil. These deposits are only effectively cleaned at high engine loads due to higher temperatures and stronger convective mass transfer induced by fast-moving gases. Therefore, before each experiment, the engine was run at the maximum possible load of 90 Nm at 2200 min⁻¹ for some time. Afterwards, the engine was shut down, both endoscopes were quickly cleaned and re-inserted, and the illumination endoscope was adjusted before starting the actual experiment. However, this procedure sometimes needed to be repeated several times before sufficient cleaning was achieved.

6 Spray, fuel film and combustion imaging in a DISI engine

This chapter presents the results from measurements performed in collaboration with Robert Bosch GmbH at their R&D campus in Renningen, Germany as part of the European Union's project PaREGEn – Particle Reduced, Efficient Gasoline Engines. Most of this chapter has been published by Shahbaz et al [100]. My role in that work was experiment planning and execution including data acquisition, as well as data analysis and most of the writing.

6.1 Introduction

In gasoline direct-injection spark-ignition (DISI) engines, fuel films from piston wetting have been identified as a primary source for soot production [25, 82]. With tightened emissions regulations, this group of phenomena has thus been the target of various optical investigations. Various studies found that sooting combustion caused by fuel films survives until the exhaust stroke and the produced soot does not oxidize completely due to low temperatures and ends up as exhaust emission [14, 25, 82]. The fuel films persisting in the exhaust stroke also contribute towards unburnt hydrocarbons in the exhaust [73, 101-103]. Among the techniques to investigate the formation and evaporation of fuel films are refractive index matching (RIM) and laser-induced fluorescence (LIF). RIM has been used to measure the fuel-film thickness by [25, 102, 104]. Henkel et al. for example investigated the effect of temperature on the evaporation of different fuel components, and suggested that control of the wall temperature may reduce the liquid fuel deposits and particulates [104]. Drake et al. combined RIM with endoscopic visualization of spray, combustion and soot luminosity, but found the light collection efficiency of the visible-only endoscope to be poor [25]. LIF has been used to visualize fuel films in optical engines [75, 105], and to determine fuel-film thickness in model experiments at room temperature [106, 107]. Schulz et al. used LIF to visualize the fuel films and investigated the effect of operating parameters on the formation of fuel films in a pressure vessel [78, 79, 108, 109], Park et al. to perform simultaneous point measurements of film thickness and temperature in an optical DISI engine [110]. In our previous work, Jüngst et al. visualized the fuel film

via LIF, and soot via laser-induced incandescence in a constant-flow facility, focusing on the effect of wall temperature and combustion on the evaporation of fuel films [111]. Geiler et al. investigated the formation and evaporation of fuel films in an optically accessible engine. Their focus was the quantification of the LIF signal, which was found to depend on film temperature [74]. Quantitative RIM and LIF imaging both require in-situ calibration, which is challenging in all-metal engines with endoscopic access.

In the current work, three endoscopic imaging techniques for the visualization of spray, fuel films, chemiluminescence, and soot incandescence were implemented in an all-metal engine. First, in motored operation, the evaporating fuel films on the piston top were visualized via LIF. The effects of injection timing, injection pressure, engine temperature and combustion on fuel-film evaporation duration were investigated. The film survival time (in cycles after injection) serves as a semi-quantitative metric. Second, in skip-fired operation, the fuel films were visualized quasi simultaneously with natural soot incandescence, giving insights on the instantaneous spatial correlation between evaporating fuel films and soot. Finally, high speed color combustion-imaging was performed, showing the temporal evolution of spray, broadband chemiluminescence from the flame front, and soot incandescence.

6.2 Experiment

6.2.1 Engine and optics

The experiments were performed in a gasoline single-cylinder DISI research engine with a total displacement of 449 cm³, a bore/stroke of 82/85 mm, and a compression ratio of 12.5. The engine temperature (T_{eng}) was maintained externally. In this work, 0°C is at compression top-dead center (TDC), i.e., crank angles during intake and compression are negative. A centrally located 6-hole injector injected one of two fuels: gasoline (reference fuel for Euro V testing) or a mixture of isooctane and 5 % toluene (isooct/tol). Mixtures of isooctane and toluene are the most commonly used simple surrogate fuels in fuel-film LIF imaging because these two liquids have similar boiling points (99 and 111°C, respectively) that are near the center of the boiling curve of gasoline, and the photophysical properties of toluene are relatively well-known. The many fluorescent species in gasoline are much less well-characterized, but gasoline has more practical significance and was expected to have potentially very different evaporation and soot-formation characteristics.

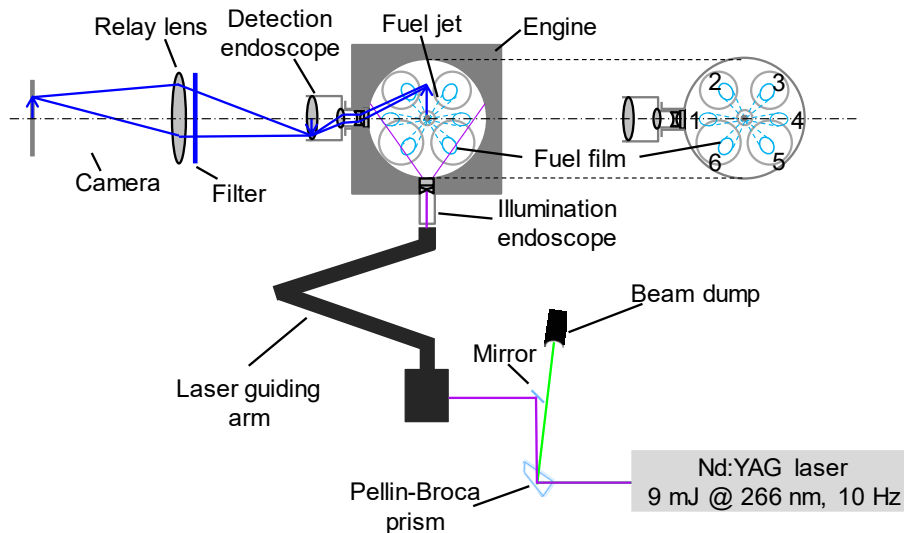


Figure 6.1: Engine, laser, and optics. For reference, the spray jets and fuel films are numbered. Filter and relay lens were different for different imaging techniques.

Figure 6.1 shows the optical layout of the experiment. Optical access to the cylinder is provided by two mutually perpendicular endoscope ports, with a diameter of 8.1 mm for illumination and 12 mm for detection. Both endoscope ports are inclined 15° to the horizontal. Parts of the piston can be illuminated and viewed within a crank-angle window of 60°CA before and after each TDC. Illumination utilizes a metal housing with a press-fit sapphire window to isolate the optics from the cylinder environment. A commercial $\text{\O}8$ mm light sheet endoscope (LaVision) was modified to produce flood illumination as mentioned in section 3.3.3. The front endoscope from hybrid UV endoscope system was used here in combination with commercial UV lenses, because the wavelength range of the investigated phenomena in this work was too wide to use the hybrid relay lens.

For fuel-film LIF, laser pulses from an Nd:YAG laser at 266 nm were directed to the illumination endoscope via a laser guiding arm. Laser pulses at 532 nm were separated using a Pellin-Broca prism and dumped into a beam dump. The pulse energy was ~ 9 mJ/pulse, measured after the laser endoscope. The laser was triggered at a constant repetition rate of 10 Hz and synchronized with the cameras and the engine by LaVision software and hardware. Operating the laser at its (fixed) design repetition rate kept the shot-to-shot energy fluctuations low, such that a shot-energy correction was not deemed necessary for the current qualitative imaging. Fluorescence was detected by an intensified CCD (Imager Intense from LaVision) camera with a resolution of 1040×1376 pixel. The relay lens was a UV camera lens (Cerco, $f = 100$ mm, $f/2.8$). Imaging was performed with 2×2 pixel hardware binning for gasoline and 4×4 binning for isoocet/tol. The gate was set

to 100 ns, and the gain (as set in LaVision's control software DaVis) was 50 for gasoline and 60 for isooot/tol. To block scattered laser light, for isooot/tol, a bandpass filter (Semrock 292/27 Brightline HC), and for gasoline a longpass filter (Semrock 266 nm RazorEdge) were used.

For quasi-simultaneous visualization of fuel-film LIF and soot incandescence, an intensified double-frame CCD camera (DiCam pro from PCO) with a resolution of 1024×1280 pixel was employed. The intensifier gate was set to 100 ns for the first frame, mainly capturing fuel film LIF, and to 5–10 μs for the second frame, capturing soot incandescence. The time delay between the two frames was 2.1 μs , which is short compared to the relevant time scales of the in-cylinder flow. The intensifier gain was 50 for the first frame and was varied between 30 and 40 for the second frame, and 2×2 hardware binning was used for all measurements. The longpass filter (Semrock 266 RazorEdge) was used for both fuels.

For high-speed color imaging, the laser illumination was replaced by a broadband halogen-lamp light source (Technolight 270 from Karl Storz) fiber-guided to the flood-illumination endoscope. A high-speed color camera (Photron, FASTCAM SA-Z) was operated at 7344 frames/second at 1024×1024 pixel resolution, corresponding to one image per 1°CA at the engine speed of 1200 min^{-1} . A commercial macro lens (Nikon, $f=105 \text{ mm}$, $f/2.8$) was used as the relay lens. Spray visualization was performed from -360°CA to -300°CA , with an exposure time of 135 μs , while in separate engine runs the chemiluminescence and soot incandescence were visualized from -20°CA to $+60^\circ\text{CA}$ with an exposure time of 70 μs . A blue Schott-glass filter (BG23, 1 mm thick) partially suppressed soot incandescence to better balance the available dynamic range of the three color channels. Both illumination and detection endoscopes were cleaned after every measurement in fired mode.

6.2.2 Operating conditions

The experiments were performed at an engine speed of 1200 min^{-1} and an intake pressure of 0.5 bar, some in motored, some in fired mode. Although the all-metal engine used in this work could be operated at higher engine speeds, which is the key advantage of such engines, the engine speed of 1200 min^{-1} was chosen to operate the engine, laser, and camera at 10 Hz repetition rate capturing an image every cycle. The engine was operated in

rest-and-work mode i.e., every work cycle with spray (and combustion in case of fired mode) was followed by number of rest cycles, constituting the rest-to-work ratio (R/W). R/W was varied throughout the experiments depending on the fuel and the operating conditions, to ensure that fuel films from the previous work cycle were completely evaporated before the next one. As an example, R/W for gasoline at $T_{eng} = 303$ K was 39:1 (1 work cycle followed by 39 rest cycles), whereas R/W for isoocet/tol at same T_{eng} was 9:1 owing to much faster evaporation of isoocet/tol. Since in work-and-rest mode the piston and cylinder walls never warm up much, this low-speed throttled operation may correspond to what is encountered shortly after a moderate cold start. For each operating point, at least 9 work cycles were recorded.

Table 6.1: Operating conditions. Superscripts: 1 - Fuel-film LIF, 2 - Simultaneous fuel-film LIF and soot incandescence, 3 - High-speed color combustion-imaging

Parameter	Variation			Constant
SOI ¹ [°CA]	-360	-340	-320	$T_{eng} = 303, 353$ K, $p_{inj} = 100$ bar
p_{inj} ¹ [bar]	100	200	350	$T_{eng} = 303, 353$ K, SOI = -360°CA
T_{eng} ^{1,2,3} [K]	303	328	353	$p_{inj} = 100$ bar, SOI ¹ = -360°CA

Table 6.1 summarizes the parameter variations explored in this work. For fuel-film LIF imaging, measurements were performed in motored operation, with injection but without ignition. The nominal global relative air/fuel ratio λ , calculated from the injected fuel mass and the intake air flow rate, was 1.0. To investigate the effect of start-of-injection timing (SOI), three different SOI were used (see Table 6.1). All were close to gas-exchange TDC to have enough fuel in the gas phase for the experiments in fired operation (see below), but also substantial piston wetting and soot formation. This variation of SOI was performed at two different T_{eng} , while the injection pressure (p_{inj}) was kept at 100 bar. The variation of p_{inj} was performed in a similar way as SOI i.e., three variations of p_{inj} at two T_{eng} , while SOI was kept at -360°CA. For T_{eng} variation, SOI and p_{inj} were kept constant. To ensure that the same amount of fuel is injected at each p_{inj} , the injection duration was adjusted to 1.70 ms, 1.23 ms and 0.95 ms at 100, 200, and 350 bar, respectively. These parameter variations were performed for both fuels.

For simultaneous fuel-film LIF and soot incandescence imaging, and high-speed color combustion imaging, only a variation of T_{eng} was investigated. The engine was now

skip-fired. To obtain stable combustion with CA50 (the crank angle at which 50 % of the heat have been released) remaining between 5–10°CA aTDC throughout the measurement, SOI, injection duration, and ignition timing were adjusted in each experiment, while p_{inj} was kept at 100 bar. The injection and ignition timings, injection duration, and IMEP are shown in Table 6.2, and it can be seen that for simultaneous fuel-film LIF and soot incandescence imaging, operating the engine with gasoline at similar operating conditions was possible, while it needed significant adjustments with isoct/tol to obtain a stable combustion. The underlying problem worsened while performing the high-speed color combustion imaging, where longer injection duration was needed to operate the engine with a stable CA50. Since the main objective of this work was to establish the endoscopic diagnostics for fuel-film LIF and soot incandescence, not a lot of efforts were put into resolving the underlying issue and get the SOI, ignition timing, and injection duration similar due to limited time. Typical global relative air/fuel ratios were around $\lambda = 0.7$. This already indicates that a substantial fraction of the fuel had not evaporated at ignition.

Table 6.2: Ignition timings (SOI) and IMEPs for: 1. Simultaneous fuel-film LIF and soot incandescence imaging, 2. High-speed color combustion imaging

	T_{eng} [K]	Gasoline				Isoct/tol			
		SOI [°CA]	Injection [ms]	Ignition [°CA]	imep [bar]	SOI [°CA]	Injection [ms]	Ignition [°CA]	imep [bar]
1	303	-320	1.7	-22	2.3	-320	2.5	-42	4.5
	328	-320	1.7	-22	2.5	-330	1.7	-38	4.0
	353	-320	1.7	-22	3.1	-360	1.7	-20	2.8
2	303	-320	3.0	-38	4.5	-320	2.8	-38	4.4
	328	-320	2.2	-38	4.0	-330	2.0	-38	4.0
	353	-320	2.0	-38	4.0	-360	2.1	-20	4.3

6.3 Image post-processing

Figure 6.2 shows the image post-processing steps for fuel-film LIF of icoct/tol. The raw image is a single-shot from the work cycle and contains the LIF signals from fuel films and engine oil as the piston surface was significantly contaminated by engine oil. The background is the ensemble average (denoted $\langle \rangle$ in this work) of images from 9 rest cycles before the “work” cycle and contains the LIF signals only from engine oil. LIF signal from

that oil was comparable in magnitude to that from the fuel films, but mostly in different locations. The background subtraction procedure effectively removed this oil background, leaving behind a clear spray pattern as shown in Figure 6.2, and was applied to all the fuel-film LIF images.

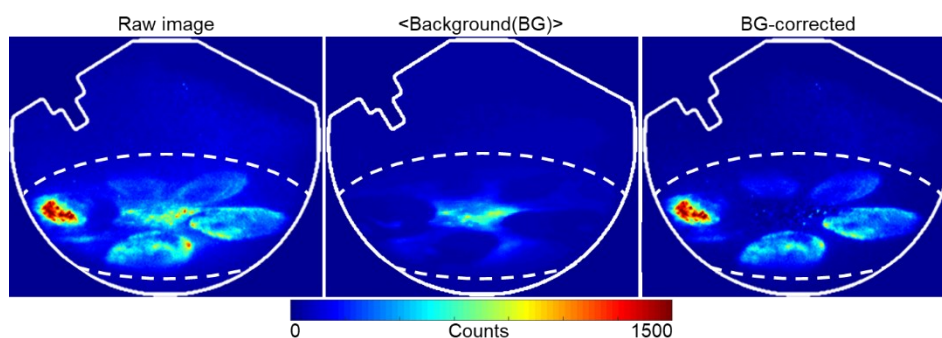


Figure 6.2: Background correction for LIF of isoct/tol fuel film at -320°CA . $\text{SOI} = -360^{\circ}\text{CA}$, $p_{inj} = 100 \text{ bar}$.

Figure 6.3 shows the post-processing steps for simultaneous fuel-film LIF and soot incandescence images. The signals from background-corrected fuel-film LIF images were normalized to the maximum signal intensity in each image, and the normalized image was set as the green and blue channels of a RGB image generating the turquoise color for the fuel-film LIF. The soot incandescence image was normalized to the maximum intensity and was set as the red channel of the respective RGB image. Consolidating the two phenomena in this way helps understanding the spatial correlation of fuel films and soot.

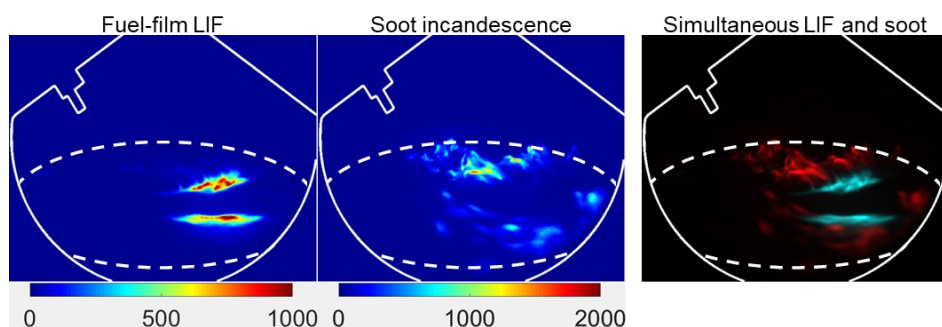


Figure 6.3: Merging of quasi-simultaneous fuel-film LIF and soot incandescence images into a single RGB images. Turquoise represents the fuel-film LIF and red represents soot incandescence.

For high-speed color imaging, a BG 23 filter was used to partially suppress soot luminosity. The signal suppression was stronger in longer wavelengths (red channel) and shifted the color balance. The red channel was enhanced by a factor of 1.5 to partially compensate for the color shift caused by the filter, as shown in see Figure 6.4.

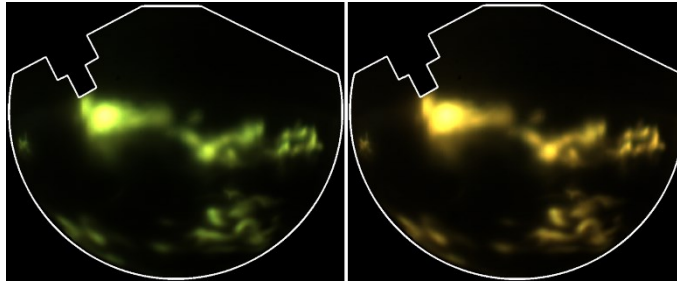


Figure 6.4: Color adjustment applied in post-processing to compensate for the apparent “color-shift” due to the BG 23 filter.

6.4 Results

6.4.1 LIF imaging of fuel films

Figure 6.5 shows background-subtracted ensemble average images of fuel-film LIF of isoct/tol at the operating conditions $T_{eng} = 353$ K, $SOI = -360^\circ CA$, and $p_{inj} = 100$ bar. The first image is from the work cycle and shows the spray at $-350^\circ CA$. The spray plumes impinge on the piston surface resulting in formation of fuel films. At $-340^\circ CA$ fuel film 6 is clearly visible, while the other fuel films are only partially visible due to the viewing angle. Haze from remnant droplets can also be seen. At $-320^\circ CA$, most of the spray has evaporated such that the individual fuel films are distinctively recognizable except fuel films 2 and 3 that merge into contiguous single film, probably because these sprays partially impinge on the spark plug. and then accumulate in the piston cavity right below the spark plug. The images at $-40^\circ CA$ and $20^\circ CA$ (i.e., now just after compression TDC) additionally show gas-phase LIF signal in the upper right side of the image where the diverging laser beam is entering. The gas-phase LIF is not visible in the previous image at $-320^\circ CA$ due to intensity scale being normalized to maximum value in the image, whereas it is shortened to the range of 0–100 counts in the later images, from $-40^\circ CA$ onwards. The gas-phase LIF signal is weak and noisy due to strong fluorescence quenching by oxygen and diminishes at $340^\circ CA$ because much of the vaporized fuel has moved out of the cylinder during the exhaust stroke. At this operating point, fuel film 6 survived a single cycle, since a small residual film is visible on the outer part of the wetted area at $-340^\circ CA$, as indicated in Figure 6.5. However, it has completely evaporated by $-320^\circ CA$ in the cycle after injection, as shown by the last image of Figure 6.5.

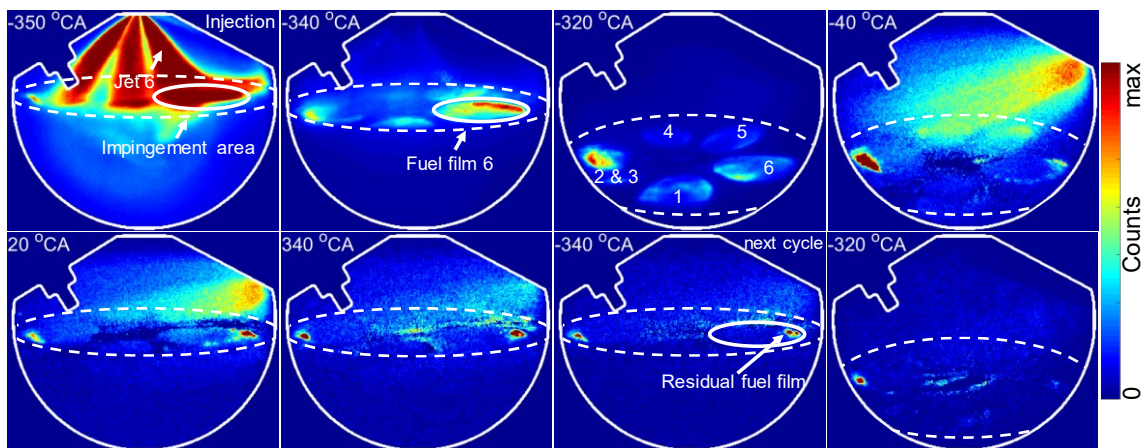


Figure 6.5: LIF images of isoocet/tol fuel-film evaporation. $T_{eng} = 353 \text{ K}$, $SOI = -360^\circ\text{CA}$, $p_{inj} = 100 \text{ bar}$. The images are ensemble-averages from 9 cycles. For the first three images, the intensity is normalized to each image's maximum intensity, for the remainder from 0 to 100 counts.

Figure 6.6 shows background-subtracted images of fuel-film LIF of gasoline at the operating conditions $T_{eng} = 303 \text{ K}$, $SOI = -360^\circ\text{CA}$, and $p_{inj} = 100 \text{ bar}$. The first image shows the spray at -350°CA . Since the fuel films took very long to disappear at these operating conditions (33 cycles in this example), all the images shown are at the same crank angle in subsequent cycles. In the next cycle at the same crank angle of -350°CA , fuel film 6 is clearly visible, while the fuel film 5 is only partially visible. The contiguous fuel films 2 & 3 are visible too. At this point, most of the gas-phase gasoline has already left the cylinder during the exhaust stroke of the previous work cycle. At this operating point, fuel film 6 survived 33 cycles, as a small residual film is visible in the central part of the wetted area, as indicated in Figure 6.6, and is completely evaporated in the next image from 34th cycle after injection.

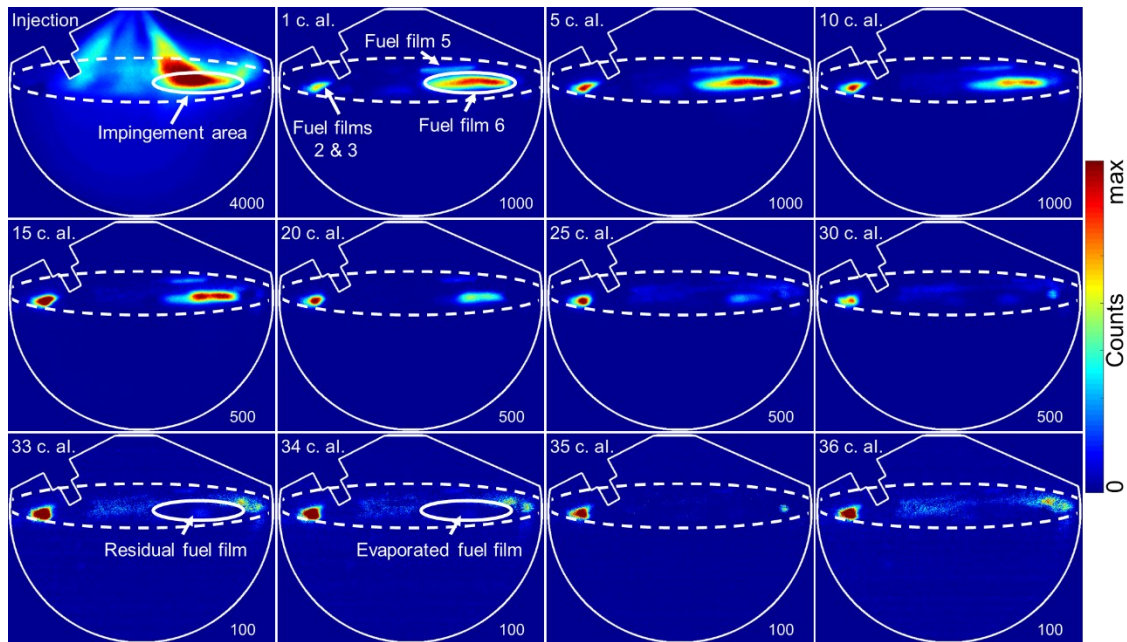


Figure 6.6: LIF single-shot images of gasoline fuel-film evaporation. $T_{eng} = 303$ K, $SOI = -360^\circ CA$, $p_{inj} = 100$ bar. The numbers in the upper-left corner are the number of cycles after injection. The upper limit of color scale for each image is shown in the lower-right corner.

6.4.1.1 Fuel-film survival time

From the LIF images, the survival time of the liquid fuel films was determined. By visual inspection, the number of cycles was counted until the LIF signal of film 6 vanishes into the background (< 10 counts in the BG-subtracted image). This method is insensitive to inhomogeneous laser illumination and shot-to-shot fluctuations in laser energy. Film 6 was chosen because it is the only one visible at all observable crank angles. Examples in Figure 6.5 and Figure 6.6 shows that the LIF signal of that film vanishes at the same time as the signal of the other ones, indicating that the survival time based on film 6 is representative for the whole spray. It can be assumed that - under the same conditions - a film that takes longer to disappear also started out thicker. Thus, the fuel-film survival time may also serve as an approximate indicator of initial thickness.

Figure 6.7 shows the fuel-film survival times under different operating conditions. The fuel-film survival times shown here are averaged from 9 recorded cycles. The standard deviations, represented by the error bars in Figure 6.7, are low, indicating that the effect of cyclic variations in work-and-rest mode is small. The gasoline fuel films typically took an order of magnitude longer than isooot/tol fuel films. Figure 6.7a shows that for $T_{eng} = 303$ K the survival time is reduced by 40 % for gasoline and 60 % for isooot/tol when shifting SOI

from -360 to -320°CA . This is because at later SOIs the piston is further away from the injector and more fuel evaporates before hitting the piston surface due to longer penetration. For $T_{eng} = 353$ K, delaying the SOI decreased the fuel film survival time for gasoline by 30 %, while no change was observed for the survival time of isoocet/tol fuel films. In the latter case, small amounts of residual films were observed around compression TDC, but they had completely evaporated by the end of the work cycle. A value of 0.5 cycles was assigned in such cases, as a more accurate determination was not possible because imaging was limited from -60° to 60°CA around both TDCs. Figure 6.7b shows that by increasing injection pressure from 100 to 350 bar, the survival time was reduced by 50% for gasoline and 40 % for isoocet/tol at $T_{eng} = 303$ K. The smaller droplets produced at higher injection pressure mostly likely evaporate more completely before hitting the piston, offsetting other, potentially contrary trends such as the droplets' shorter travel time. An increase in p_{inj} became less effective in reducing the survival time at elevated engine temperature, and the survival time was reduced by 30 % for gasoline while it remained at about 0.5 cycles for isoocet/tol. Figure 6.7c shows that by increasing the T_{eng} from 303 K to 353 K, the fuel-film survival time decreased by 75 % for gasoline and 80 % for isoocet/tol. This indicates that the T_{eng} had a primary impact on fuel-film survival time. These results are consistent with the studies from Henkel et al. in an optical engine [104], and Schulz et al. in a model experiment [78, 79, 108].

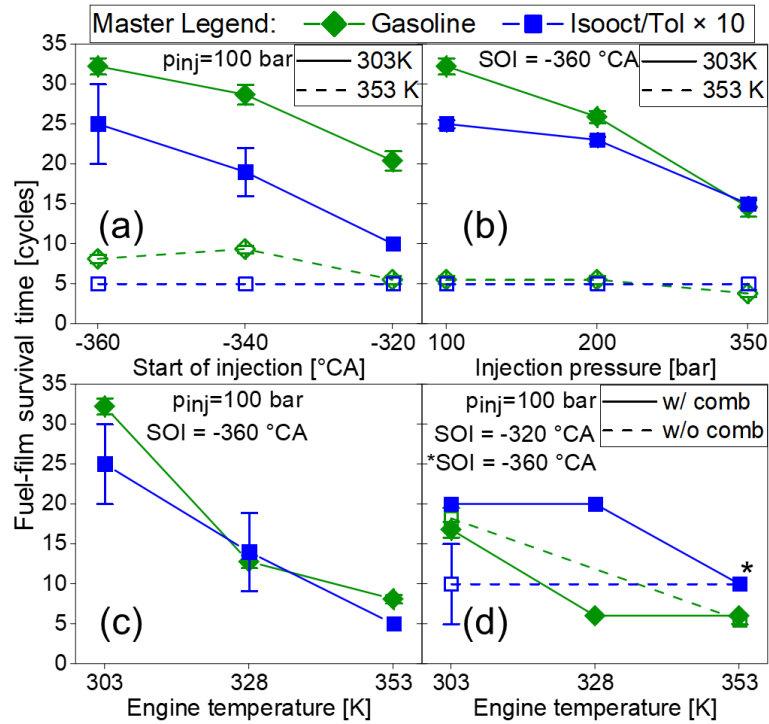


Figure 6.7: Fuel-film survival times for gasoline and isooot/tol for (a) different SOI, (b) different p_{inj} , (c) different T_{eng} , (d) with and without combustion. The survival times for isooot/tol are multiplied by a factor of 10.

6.4.2 Simultaneous fuel-film LIF and soot incandescence imaging

Figure 6.8 shows background-subtracted single-shots and ensemble-average (mean) image of fuel-film LIF (turquoise) and natural soot incandescence (red) at 20 and 50°CA for isooot/tol for different T_{eng} . Small soot pockets were detected near distinct fuel films at $T_{eng} = 303$ K. This is because the fuel films evaporate slowly at this temperature, generating only small fuel-rich regions close to the fuel films that eventually produce soot. At $T_{eng} = 353$ K, the fuel films and the soot incandescence are spread over the piston surface, and also appear to be convectively moved in the direction of the in-cylinder charge motion. This is probably because at higher engine temperature the fuel films evaporate faster and more fuel vapor is generated, creating a larger fuel-rich region over the piston surface. Also, due to the decreasing viscosity at elevated engine temperature the fuel films themselves already spread over a larger area on the piston surface under the influence of in-cylinder charge motion. The difference is evident from both single-shots and ensemble-averaged images at two different engine temperatures, with latter showing that the spatial structure of fuel films and soot is consistent throughout the single shots.

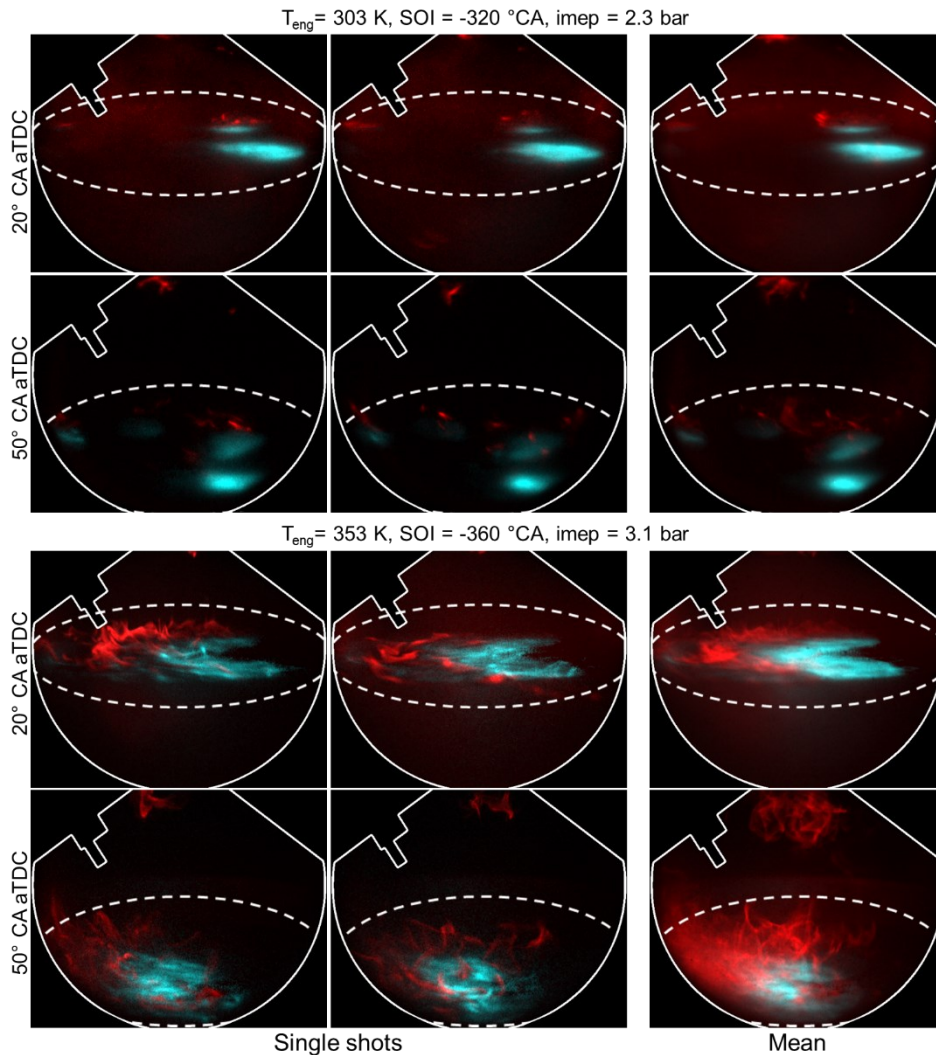


Figure 6.9: Simultaneous fuel-film LIF (turquoise) and soot incandescence (red) single-shot images for gasoline ($p_{inj} = 100$ bar).

This may be because the injection duration for isooc/tol was increased from 1.7 ms to 2.5 ms to obtain stable combustion, and because isooc/tol fuel films evaporate faster than gasoline and generate more vapor in the abutting regions. The former is also reflected by the higher IMEP of 4.5 bar, compared to 2.3 bar for gasoline. At $T_{eng} = 353$ K, the fuel films and the soot incandescence show similar behavior as isooc/tol, i.e., spread over the piston surface, and appear to be convectively moved in the direction of the in-cylinder charge motion. Since the gasoline fuel films survived approximately 6 cycles at this operating point (see Figure 6.7d), there is a high probability that a substantial amount of fuel still adhered to piston surface when these images were taken, as shown in Figure 6.9. Additionally, Figure 6.9 shows soot incandescence around the injector tip for gasoline. This indicates tip wetting, which also results in locally rich fuel/air-mixtures.

Another possible reason for the LIF signals from all over the piston surface at $T_{eng} = 353$ K could be the persistent presence of the engine oil on the piston surface. It can be seen in Figure 6.2 that substantial amount of engine oil is present on the piston surface. Even though the engine oil was cleaned before each measurement, it still rose up in the cylinder during each measurement and contaminated the piston surface. Due to lower viscosity at this engine temperature, the engine oil probably may be more readily transported over the piston surface by the in-cylinder flow, and the resulting LIF signals could not be entirely corrected in background subtraction. However, this speculated behavior needs further investigation.

6.4.3 High-speed visualization of spray, flame front, and soot incandescence

Figure 6.10 shows high-speed image sequence of a spray at $SOI = -320^{\circ}CA$ and $p_{inj} = 100$ bar. The engine speed was 1200 min^{-1} and T_{eng} was 303 K. Images were taken with $1^{\circ}CA$ resolution, but fewer are shown here. The individual spray plumes are recognizable and can be seen impinging the piston surface. The delay between electronic and hydraulic SOI can be observed here, as the injection only starts at $-318^{\circ}CA$ instead of $-320^{\circ}CA$. The piston surface is also visible, and the pattern formed by transportation of deposited soot particles under the impinging jets is also visible, along with the oil droplets the piston surface. The jet impingement areas in the first two images appear to be dry and without droplets, which confirms that the droplets in the other area are actually from engine oil. The fuel-jets were narrow and distinct at the start but increased in cross-section at later crank angles ($-315^{\circ}CA$ and $-300^{\circ}CA$). By this method, jet behavior at different conditions can be studied under real engine conditions.

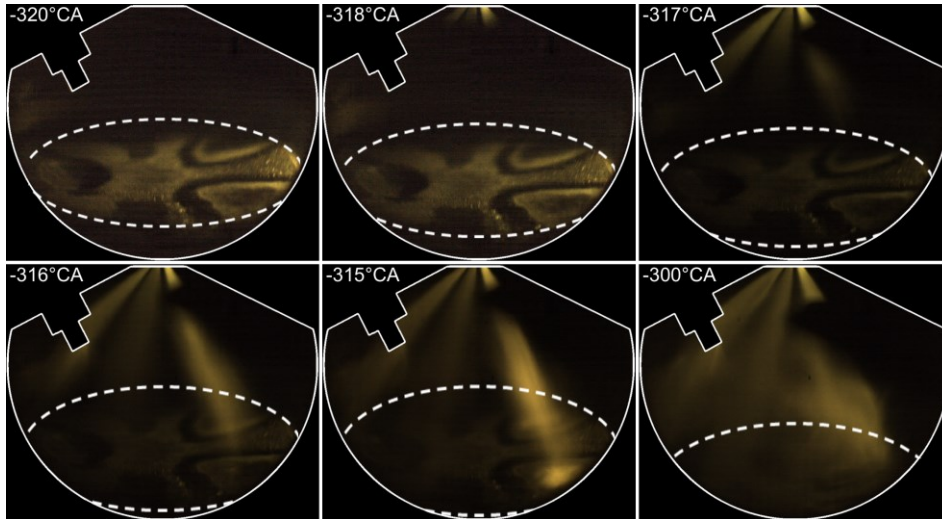


Figure 6.10: High-speed single-shot images of Mie-scattered light from the spray. Fuel: *isooct/tol*, $n = 1200 \text{ min}^{-1}$, $p_{inj} = 100 \text{ bar}$, $SOI = -320^\circ\text{CA}$, ignition at -38°CA .

Figure 6.11 shows a high-speed imaging sequence of the combustion with *isooct-tol* as the fuel at $T_{eng} = 303 \text{ K}$, $SOI = -320^\circ\text{CA}$, $p_{inj} = 100 \text{ bar}$, and ignition at -38°CA . At -10°CA , very weak chemiluminescence signal is observed, with increasing intensity at later crank angles. Until 5°CA solely the chemiluminescence of the flame front is visible. Soot incandescence is additionally detected close to films 2 & 3 at 10°CA . Chemiluminescent combustion and soot formation thus seem to be distinct events with some temporal overlap. It was observed that soot formation started $20\text{--}25^\circ\text{CA}$ (about 2.8 to 3.5 ms) later than the flame front starts to propagate. At 20°CA , the chemiluminescence signal diminishes, and only soot incandescence is visible near the evaporating fuel films. The soot incandescence was observed to be in small pockets, consistent to what was observed with simultaneous fuel-film LIF and soot incandescence imaging at same engine temperature.

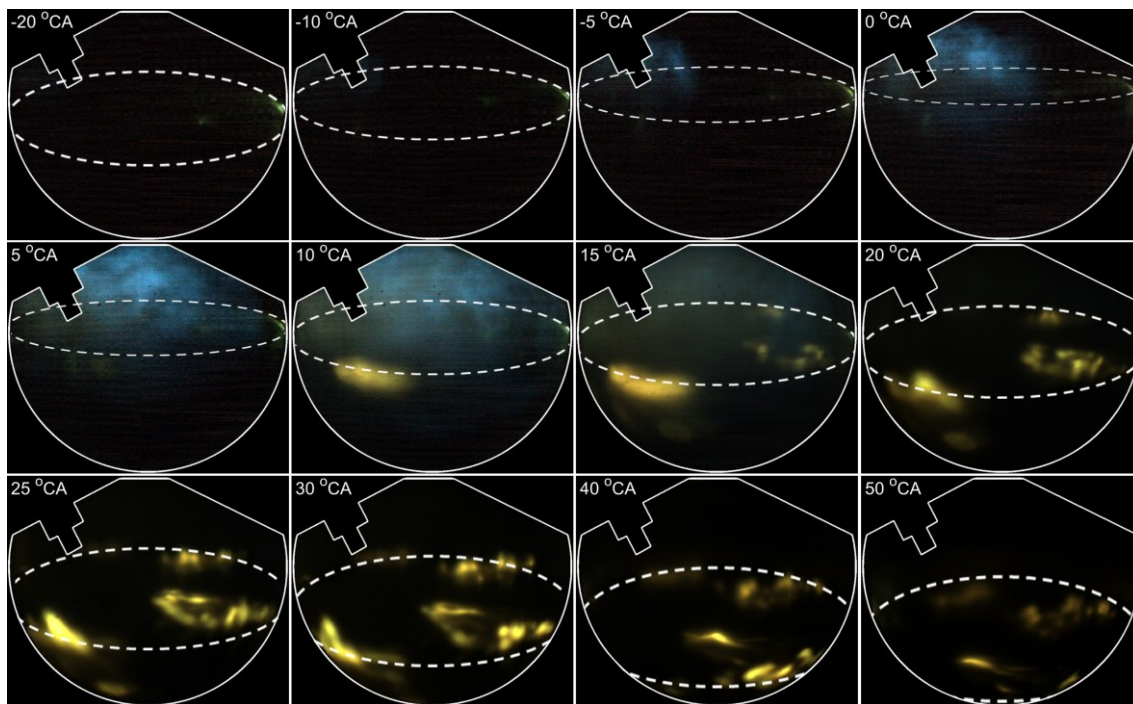


Figure 6.11: High-speed images of Mie-scattered light from the spray, chemiluminescence of the flame, and soot incandescence. Numbers indicate the individual fuel films. Fuel: isooot/tol, $n = 1200 \text{ min}^{-1}$, $p_{inj} = 100 \text{ bar}$, $SOI = -320^\circ\text{CA}$, ignition at -38°CA .

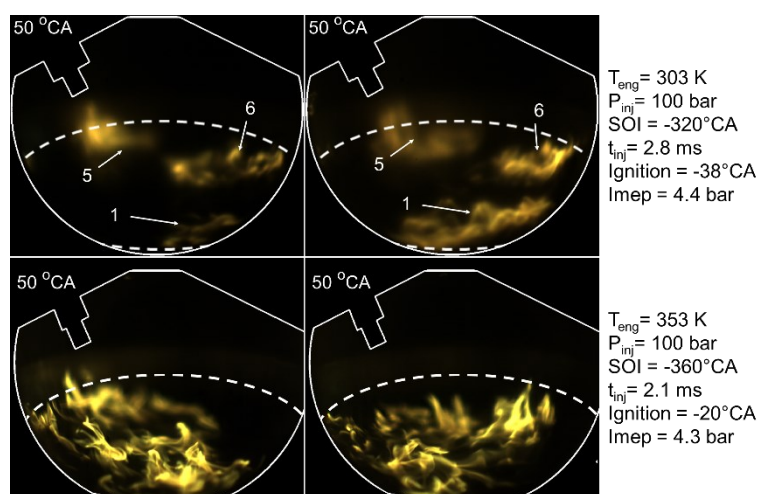


Figure 6.12: Snapshots of soot incandescence images with isooot/tol as a fuel at 50°CA aTDC extracted from high-speed imaging at different T_{eng} . Numbers indicate the individual fuel films.

Figure 6.12 shows the soot incandescence for isooot/tol for two different engine temperatures at 50°CA . At $T_{eng} = 303 \text{ K}$, soot again is detected in distinct, spatially separated regions near the fuel films. These regions appear larger in size for isooot/tol than observed in Figure 6.8 because the injection duration was increased from 2.5 to 2.8 ms for stable engine operation. At $T_{eng} = 353 \text{ K}$, the soot incandescence is spreading over the whole piston surface for both fuels. This behavior is consistent with that seen in Figure 6.8.

Figure 6.13 shows the soot incandescence for gasoline for two different engine temperatures at 50°CA . Here too, soot is detected in distinct, spatially separated regions near the fuel films at $T_{eng} = 303\text{ K}$, and spread over the whole piston surface at $T_{eng} = 353\text{ K}$. These regions at $T_{eng} = 303\text{ K}$ appear much larger in size and hard to distinguish from each other because the injection duration was significantly increased from 1.7 to 3.0 ms, resulting in more fuel mass adhering to the piston surface and later being available for soot formation. Soot incandescence around the injector tip is also observed here. The overall behavior observed here is consistent with that shown in Figure 6.9.

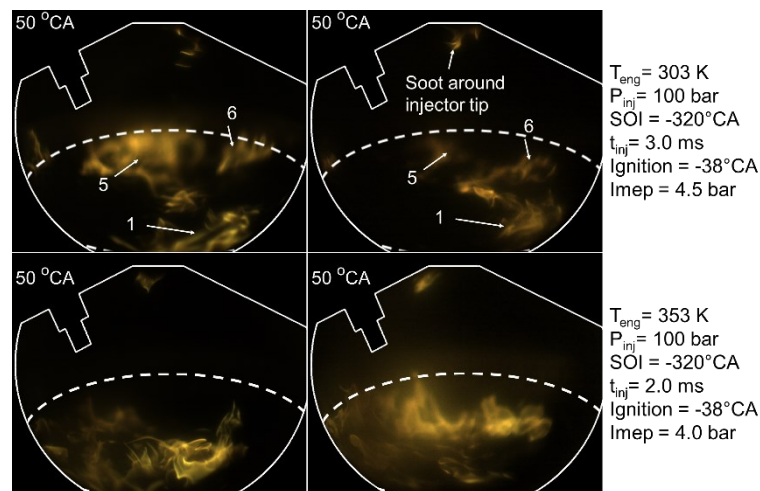


Figure 6.13: Snapshots of soot incandescence images with gasoline as a fuel at 50°CA aTDC extracted from high-speed imaging at different T_{eng} . Numbers indicate the individual fuel films.

7 Conclusions

Optical diagnostics are an excellent non-intrusive method to visualize in-cylinder processes in internal combustion engines. Typically, optical diagnostics are applied in research engines with transparent liners and piston windows. These so-called “optical” engines have different thermodynamic properties and a limited speed/load range compared to commercial engines. An all-metal engine with small endoscopic access can have heat transfer and speed/load range similar to a commercial engine. In this thesis, a hybrid UV endoscope system developed in previous work [2] was modified, characterized, and used to visualize various in-cylinder processes.

In the first part of this thesis, modifications of the hybrid UV endoscope system that originally used a custom-designed refractive/diffractive optical element (DOE) for its single relay stage were investigated. The idea was to examine if it was reasonable to replace the DOE with one of the UV camera lenses that are already available in many combustion laboratories and have a wide range of use cases. Here, a Cerco 45 mm $f/1.8$ and a LaVision 85 mm $f/2.8$ UV lens were compared to a 90 mm $f/2$ DOE designed for 275–350 nm, along with variations in which the aperture of the DOE was reduced or the focal length of the LaVision lens was shortened with additional UV achromats. The performance of the imaging systems was compared at two different magnifications, which yielded different results due to anisotropic light propagation from the detection endoscope.

With the Cerco lens, the system showed the best or nearly the best performance in all three metrics considered here, resolution, chromatic aberration correction, and light collection. However, because of its short focal length, the Cerco has a short working distance of approximately 115 mm between endoscope and relay lens for the 1:2 relay magnification, and 85–90 mm for 1:1 magnification. This short working distance can be a problem when more optical components like beam splitter and/or filters need to be placed between the front endoscope and the camera lens. If the shorter working distance is not an issue, then this lens is the best option among all the imaging systems tested here.

The DOE had equally good light collection as the Cerco lens, but worse resolution. In the former, the best resolution was limited to the central part (310–330 nm) of the design

wavelength range (275–350 nm), and chromatic aberration was also limited over a narrower range. This means a specific DOE is needed for each application with a different wavelength range – which was part of the original design concept [2]. The working distance of the DOE was between 180 and 230 mm for both relay magnifications, enough for multiple optical elements between front endoscope and DOE. At relay magnification of 1:2, reducing the aperture improved resolution at the expense of light collection efficiency, but still, the “better” resolution region was spectrally quite limited. At the relay magnification of 1:1, neither resolution nor light collection were affected by the introduction of apertures down to $f/3.5$, as the effective entrance pupil was similar to the aperture at $f/3.5$ due to anisotropic light propagation from the field lens of the detection endoscope. However, introduction of smaller apertures than $f/3.5$ would affect the resolution and the light collection. Replacing the CCD with an ICCD did not significantly degrade the resolution at the relay magnification of 1:1, again consistent with the original design targets [2]. For applications where the detection wavelengths are within the design range of the DOE, and an intensified camera is necessary due to low light, the DOE may be the better option. It has the advantage of better light collection and sufficient working distance, while the resolution is limited by the intensifier anyway.

With the LaVision lens as the relay, the system had the best resolution among the investigated systems at all relay magnifications and cameras, and also the most limited chromatic aberration, but the difference to the Cerco lens in these two metrics was small. However, the former lens had the worst light collection efficiency. Addition of UV-achromats (300 and 200 mm focal length) as “close-up lenses” degraded the resolution by a factor of two over much of the wavelength range, while increasing light collection only slightly. Thus, neither combination can be recommended. It is likely that a custom-designed achromat could improve the situation, since the degraded quasi-monochromatic performance indicates that spherical aberration is to blame for a large part of the degradation in resolution. If the scene is bright enough, the LaVision lens is recommended because it combines high resolution, sufficient working distance, and limited chromatic aberration with more universal applicability for general combustion imaging.

In the second part, previous work from our group [5] to measure the gas-phase temperature via two-color anisole-LIF in an all-metal engine with endoscopic access was extended. Anisole, due to its photo-physical properties, is a strong candidate for its use as a tracer in non-intrusive LIF diagnostics in combustion engines and other applications. It was used as

a tracer with the base fuel isooctane in an all-metal engine with endoscopic access. The imaging was performed through the hybrid UV endoscope system and two ICCD cameras. Anisole LIF signal levels were first compared to those of toluene. Toluene is one of the best-characterized tracers, but anisole yielded much higher signal levels when both tracers' concentration was limited by laser attenuation, which here was the case for 20 % toluene vs. 2.5 % anisole. The signal was 10 times higher in the early compression stroke and 4 times higher in the late compression stroke. Due to higher signal of anisole LIF, small structures of the turbulent flame burning into the anisole/isooctane-mixture were clearly visible after ignition.

Since this test was promising, anisole was used for ratiometric two-color LIF thermometry, a technique we had implemented endoscopically before with toluene, but without achieving good quality single-shot images [58]. From spectroscopic data in the literature, different empirical signal models considering the effects of temperature and oxygen partial pressure (p_{O_2}) were assembled. The models can be categorized mainly as 2-step fit function, fitting separately for p_{O_2} and temperature, and a single 3D surface fit function incorporating the effect of both parameters on the signal ratio. Each category had further variations in terms of the function governing the effect of temperature on the signal ratio. An in-situ calibration was performed in nitrogen and air at temperatures ranging from room temperature to 573 K. The calibrated models were used to convert the red/blue LIF signal ratio to temperature in the compression stroke, which was compared to the adiabatic pressure-based temperature. It was found that the 3D surface fit functions greatly overestimated the temperatures in the late compression stroke. The 2-step fit functions with exponential temperature-dependent part yielded temperatures closer to the adiabatic temperature until ignition, but with some deviation when the p_{O_2} in the cylinder increased beyond that in available spectroscopic data and the effect of increasing p_{O_2} on the signal ratio was interpolated.

The 2-step fit function with exponential temperature-dependent part was then used to visualize the spatial temperature distribution at different crank angles during the compression stroke. As expected for the port-fuel-injected operation, the temperature was found to be uniform across the FOV, with later crank angles showing more noise because of lower signal due to higher temperatures. The spatial temperature distribution around the gas-exchange TDC were also visualized. The residual gas was assumed to be unaltered anisole, or some similar aromatic hydrocarbons as incomplete combustion products.

Residual gas mixture was observed moving along the in-cylinder tumble at crank angles shortly before TDC with measured temperatures close to the temperature measured in the exhaust downstream of the valve. A clear temperature segregation was observed when fresh charge started entering in the cylinder with temperature decreasing with progressing intake stroke, similar to what was observed in our previous work with toluene LIF [58].

The results clearly showed that for anisole-LIF two-color thermometry considering the effect of oxygen partial pressure is also important. Lack of spectroscopic data is an issue, since the available data only covers about 7 % of the encountered range in p_{O_2} . If further spectroscopic data were available, the accuracy of the temperature determined by two-color thermometry with anisole may be improved. The correlation of signal ratio and temperature also needs to be more accurately established with the help of more spectroscopic data, especially at high temperatures. The available data covered more than 50 % of the required temperature range, but an incorrect exponential fit function may result in large error at high temperatures.

In the first part of this thesis, it was determined that the front endoscope of the hybrid UV endoscope system can indeed be coupled with commercial UV lenses without any major disadvantage when the working distance between front endoscope and relay lens can be relatively small. Therefore, in the third part of this thesis, three endoscopic imaging techniques were applied to visualize spray, fuel films, chemiluminescence, and soot incandescence in an endoscopically accessible all-metal DISI engine. First, in motored operation, fuel films on the piston surface were visualized by flood-illumination UV LIF. The effect of varying injection duration, engine temperature, and injection pressure on the fuel-films' survival times was investigated in a "work"-and-rest scheme. Second, fuel films and soot were quasi-simultaneously visualized via double-frame imaging of LIF and natural incandescence, respectively. Third, high-speed color imaging showed the spray, flame chemiluminescence, and soot incandescence.

The results showed that under all conditions gasoline fuel films survive about an order of magnitude longer than isooctane/toluene films. The engine temperature had a primary effect on the film survival time for both fuels. This is in line with the findings of Henkel et al. [104] and Schulz et al. [78, 108] in model experiments. Delaying the injection timing and increasing the injection pressure resulted in a significant reduction of the survival time only for an engine temperature of 303 K. Combustion (in work-and-rest mode) had no significant effect on the survival time, which is consistent with recent results in a

constant-flow model experiment [111]. However, in this investigation only a single cycle in a sequence of several motored ones was fired, such that each fired cycle corresponded to what might be an early cycle in a cold-to-hot transient. Because of the strong influence of wall temperature, continuous firing is expected to have a stronger effect on fuel-film evaporation.

Simultaneous fuel-film LIF and soot incandescence imaging showed the fuel films on the piston surface and soot incandescence in adjacent regions. Soot incandescence was found preferentially downstream from the films in the direction of the tumble flow, and the spatial structure also indicated shear by the flow. At $T_{eng} = 303$ K the films appeared as distinct spots, while at 353 K they were more contiguous over the whole piston top. We speculate that the decreasing viscosity of both fuel and oil – the latter as a contaminant on the piston surface – lead to this phenomenon. While little soot was seen at $T_{eng} = 303$ K, and more closely just above the distinct fuel films, soot incandescence was spread over the whole piston top with higher intensity at 353 K. It is likely that at the lower surface temperature the lower rate of film evaporation limits the fuel available for pyrolysis and soot formation in the gas phase. Again, in continuously fired operation the implications would be different than in work-and-rest mode, since then the fuel not evaporated in one cycle would carry over to the next fired cycle.

High-speed combustion imaging showed soot incandescence delayed from blue chemiluminescence, and this timing was consistent with what was observed in simultaneous fuel-film LIF and soot incandescence imaging at different temperatures. This is consistent with the notion that most soot formation from fuel films does not take place in pool fires, but due to evaporation and pyrolysis in an environment that is oxygen-depleted by the main combustion event.

From a diagnostics point of view, the three techniques applied here complement each other well. High-speed color imaging gives a quick overview of the major spatio-temporal features of injection and combustion. Endoscopic UV flood-illumination LIF may have been used here for first time and yielded very clear images of the structure of the fuel films. The film survival time was determined here by visual inspection, but this could be automated. Finally, the double-frame intensified camera allowed capturing quasi-simultaneous (but not wavelength-specific) images of soot incandescence with at most minor disadvantages. If available high-repetition-rate UV light sources are found sufficiently powerful to excite well-detectable film fluorescence, the double-frame concept

could be extended into alternate-frame imaging of films and soot at kHz rates with an intensified high-speed camera.

8 References

- [1] Emissions of air pollutants from transport, <https://www.eea.europa.eu/data-and-maps/indicators/transport-emissions-of-air-pollutants-8/transport-emissions-of-air-pollutants-6>
- [2] Reichle, R., Pruss, C., Gessenhardt, C., Schulz, C., Osten, W., Diffractive/refractive (hybrid) UV-imaging system for minimally invasive metrology: design, performance, and application experiments, *Applied Optics* 51 (2012) 1982-1996.
- [3] Zimmermann, F., New approaches for optical and microoptical diagnostics in IC engines, PhD thesis, Ruprecht-Karls-Universität, Heidelberg, 2006.
- [4] Gessenhardt, C., Endoskopische Bestimmung des Temperaturfeldes im Brennraum eines Ottomotors mittels laserinduzierter Fluoreszenz, PhD thesis, University of Duisburg-Essen, Duisburg, 2013.
- [5] Goschütz, M., Endoskopische Brennraumdiagnostik im seriennahen Ottomotor durch Chemilumineszenz und laserinduzierte Fluoreszenz, PhD thesis, University of Duisburg-Essen, Duisburg, 2019.
- [6] International Standard ISO 12233:2018(E)
- [7] Nori, V., Seitzman, J. in: Chemiluminescence Measurements and Modeling in Syngas, Methane and Jet-A Fueled Combustors, *45th AIAA Aerospace Sciences Meeting and Exhibit*, 2007.
- [8] Hardalupas, Y., Orain, M., Local measurements of the time-dependent heat release rate and equivalence ratio using chemiluminescent emission from a flame, *Combustion and Flame* 139 (2004) 188-207.
- [9] Arias, L., Torres, S., Sbarbaro, D., Farias, O., Photodiode-based sensor for flame sensing and combustion-process monitoring, *Applied Optics* 47 (2008) 5541-5549.
- [10] Haber, L. C., Vandsburger, U., A global reaction model for OH* chemiluminescence applied to a laminar flat-flame burner, *Combustion Science and Technology* 175 (2003) 1859-1891.
- [11] Kathrotia, T., Reaction Kinetics Modeling of OH*, CH*, and C²* Chemiluminescence., PhD thesis, Ruprecht-Karls-Universität, Heidelberg, 2011.
- [12] Krishnamachari, S. L. N. G., Broida, H. P., Effect of Molecular Oxygen on the Emission Spectra of Atomic Oxygen-Acetylene Flames, *The Journal of Chemical Physics* 34 (1961) 1709-1711.
- [13] Jakob, M., Hülser, T., Janssen, A., Adomeit, P., Pischinger, S., Grünefeld, G., Simultaneous high-speed visualization of soot luminosity and OH* chemiluminescence of alternative-fuel combustion in a HSDI diesel engine under realistic operating conditions, *Combustion and Flame* 159 (2012) 2516-2529.
- [14] Stojkovic, B. D., Fansler, T. D., Drake, M. C., Sick, V., High-speed imaging of OH* and soot temperature and concentration in a stratified-charge direct-injection gasoline engine, *Proceedings of the Combustion Institute* 30 (2005) 2657-2665.

- [15] Shawal, S., Goschutz, M., Schild, M., Kaiser, S., Neurohr, M., Pfeil, J., Koch, T., High-Speed Imaging of Early Flame Growth in Spark-Ignited Engines Using Different Imaging Systems via Endoscopic and Full Optical Access, *SAE International Journal of Engines* 9 (2016) 704-718.
- [16] Smith, J. D., Sick, V., High-speed fuel tracer fluorescence and OH radical chemiluminescence imaging in a spark-ignition direct-injection engine, *Applied Optics* 44 (2005) 6682-6691.
- [17] Goschütz, M., Schulz, C., Kaiser, S. A., Endoscopic Imaging of Early Flame Propagation in a Near-Production Engine, *SAE International Journal of Engines* 7 (2014) 351-351.
- [18] Sauer, M., Hofkens, J., Enderlein, J., *Handbook of Fluorescence Spectroscopy and Imaging*, Wiley-VCH Verlag GmbH & Co. KGaA, 2011.
- [19] Schulz, C., Sick, V., Tracer-LIF diagnostics: quantitative measurement of fuel concentration, temperature and fuel/air ratio in practical combustion systems, *Progress in Energy and Combustion Science* 31 (2005) 75-121.
- [20] Aldén, M., Bood, J., Li, Z., Richter, M., Visualization and understanding of combustion processes using spatially and temporally resolved laser diagnostic techniques, *Proceedings of the Combustion Institute* 33 (2011) 69-97.
- [21] Koban, W., Koch, J. D., Hanson, R. K., Schulz, C., Oxygen quenching of toluene fluorescence at elevated temperatures, *Applied Physics B: Lasers and Optics* 80 (2005) 777-784.
- [22] Tran, K. H., Morin, C., Kühni, M., Guibert, P., Fluorescence spectroscopy of anisole at elevated temperatures and pressures, *Applied Physics B: Lasers and Optics* 115 (2014) 461-470.
- [23] Faust, S., Characterisation of organic fuel tracers for laser-based quantitative diagnostics of fuel concentration, temperature, and equivalence ratio in practical combustion processes, PhD thesis, University of Duisburg-Essen, Duisburg, 2013.
- [24] O'Connor, J., Musculus, M., In-Cylinder Mechanisms of Soot Reduction by Close-Coupled Post-Injections as Revealed by Imaging of Soot Luminosity and Planar Laser-Induced Soot Incandescence in a Heavy-Duty Diesel Engine, *SAE International Journal of Engines* 7 (2014) 673-693.
- [25] Drake, M. C., Fansler, T. D., Solomon, A. S., Szekely, G. A., Piston Fuel Films as a Source of Smoke and Hydrocarbon Emissions from a Wall-Controlled Spark-Ignited Direct-Injection Engine, SAE Technical Paper 2003-01-0547, 2003.
- [26] Dierksheide, U., Meyer, P., Hovestadt, T., Hentschel, W., Endoscopic 2D particle image velocimetry (PIV) flow field measurements in IC engines, *Experiments in Fluids* 33 (2002) 794-800.
- [27] Peterson, B., Baum, E., Böhm, B., Sick, V., Dreizler, A., High-speed PIV and LIF imaging of temperature stratification in an internal combustion engine, *Proceedings of the Combustion Institute* 34 (2013) 3653-3660.
- [28] Fajardo, C. M., Smith, J. D., Sick, V., PIV, high-speed PLIF and chemiluminescence imaging for near-spark-plug investigations in IC engines, *Journal of Physics: Conference Series* 45 (2006) 19-26.

- [29] Eckbreth, A. C., *Laser diagnostics for combustion temperature and species*, CRC Press, 1996.
- [30] Düwel, I., Kunzelmann, T., Schorr, J., Schulz, C., Wolfrum, J., Application of fuel tracers with different volatilities for planar LIF/Mie drop sizing in evaporating systems, *Proceedings of the 9th International Conference on Liquid Atomization and Spray Systems ICLASS*, 2003.
- [31] Aberrations, <http://hyperphysics.phy-astr.gsu.edu/hbase/geoopt/aberrcon.html>
- [32] Gross, H., *Handbook of Optical Systems: Volume 1*, WILEY-VCH Verlag GmbH & Co. KGaA, 2005.
- [33] Spherical aberration, https://commons.wikimedia.org/wiki/File:Spherical_aberration_2.svg
- [34] Coma, <https://commons.wikimedia.org/wiki/File:Lens-coma.svg>
- [35] Astigmatism, <https://commons.wikimedia.org/wiki/File:Astigmatism.svg>
- [36] Field curvature, https://commons.wikimedia.org/wiki/File:Field_curvature.svg
- [37] Orthoscopic doublet, <http://230nsc1.phy-astr.gsu.edu/hbase/geoopt/mulens.html>
- [38] Eyepieces, <http://hyperphysics.phy-astr.gsu.edu/hbase/geoopt/eyepiece.html>
- [39] Distortion, https://learn.foundry.com/modo/902/content/help/pages/rendering/camera_matching.html
- [40] Chromatic aberration, <https://photographylife.com/what-is-chromatic-aberration>
- [41] Diffractive optical element, <https://commons.wikimedia.org/wiki/File:Diffractive.png>
- [42] Achromatic doublet, <https://commons.wikimedia.org/wiki/File:Lens6b-en.svg>
- [43] Introduction to Modulation Transfer Function, <https://www.edmundoptics.eu/knowledge-center/application-notes/optics/introduction-to-modulation-transfer-function>
- [44] Boreman, G. D., *Modulation Transfer Function in Optical and Electro-Optical Systems*, SPIE Press, 2001.
- [45] Estribeau, M., Magnan, P., Fast MTF measurement of CMOS imagers using ISO 12333 slanted-edge methodology, *Proceedings of SPIE 5251, Detectors and Associated Signal Processing*, 2004.
- [46] Mtui, P., Hill, P., Ignition Delay and Combustion Duration with Natural Gas Fueling of Diesel Engines, SAE Technical Paper 961933, 1996.
- [47] J. Eismark, M. Balthasar, A. Karlsson, T. Benham, M. Christensen, Role of Late Soot Oxidation for Low Emission Combustion in a Diffusion-controlled, High-EGR, Heavy Duty Diesel Engine, SAE Technical Paper 2009-01-2813, 2009.
- [48] Kong, S.-C., Ricart, L. M., Reitz, R. D., In-Cylinder Diesel Flame Imaging Compared with Numerical Computations, SAE Technical Paper 950455, 1995.
- [49] Miers, S. A., Ng, H., Ciatti, S. A., Stork, K., Emissions, performance, and in-cylinder combustion analysis in a light-duty diesel engine operating on a fischer-tropsch, biomass-to-liquid fuel, SAE Technical paper 2005-01-3670, 2005.

- [50] Bakenhus, M., Reitz, R. D., Two-Color Combustion Visualization of Single and Split Injections in a Single-Cylinder Heavy-Duty D.I. Diesel Engine Using an Endoscope-Based Imaging System, SAE Technical Paper 1999-01-1112, 1999.
- [51] Shiozaki, T., Nakajima, H., Kudo, Y., Miyashita, A., Aoyagi, Y., The Analysis of Combustion Flame Under EGR Conditions in a DI Diesel Engine, SAE Technical Paper 960323, 1996.
- [52] Sczomak, D. P., Zhao, A., Simon, M. S., Zeng, Y., High Speed Endoscope Imaging to Supplement CFD Analysis and Combustion Testing for SIDI Engine Startup Development, SAE Technical Paper 2010-01-0347, 2010.
- [53] Sementa, P., Maria Vaglieco, B., Catapano, F., Thermodynamic and optical characterizations of a high performance GDI engine operating in homogeneous and stratified charge mixture conditions fueled with gasoline and bio-ethanol, *Fuel* 96 (2012) 204-219.
- [54] Schänzlin, K., Koch, T., Boulouchos, K., Characterization of the Combustion in a Direct Injection Spark Ignition Engine, SAE Technical Paper 2002-01-0834, 2002.
- [55] T. Kato, K. Akiyama, T. Nakashima, R. Shimizu, Development of Combustion Behavior Analysis Techniques in the Ultra High Engine Speed Range, SAE Technical Paper 2007-01-0643, 2007.
- [56] F. Wytrykus, R. Duesterwald, Improving Combustion Process by Using a High Speed UV-Sensitive Camera, SAE Technical Paper 2001-01-0917, 2001.
- [57] Richter, M., Axelsson, B., Aldén, M., Engine Diagnostics Using Laser Induced Fluorescence Signals Collected Through an Endoscopic Detection System, SAE Technical Paper 982465, 1998.
- [58] Gessenhardt, C., Schulz, C., Kaiser, S. A., Endoscopic temperature imaging in a four-cylinder IC engine via two-color toluene fluorescence, *Proceedings of the Combustion Institute* 35 (2015) 3697-3705.
- [59] Gessenhardt, C., Zimmermann, F., Schulz, C., Reichle, R., Pruss, C., Osten, W., Hybrid Endoscopes for Laser-Based Imaging Diagnostics in IC Engines, SAE Technical Paper 2009-01-0655, 2009.
- [60] Witzel, B., Konstruktion optischer Zugänge an einem 4-Zylinder Serienmotor zur Durchführung laseroptischer Messungen mittels mikroinvasiver Endoskoptechnik, Bachelor thesis, University of Duisburg-Essen, Duisburg, 2007.
- [61] Plano-convex cylindrical lens LJ4305-UV, <https://www.thorlabs.com/thorproduct.cfm?partnumber=LJ4305-UV>
- [62] Plano-concave cylindrical lens LK4351-UV, <https://www.thorlabs.com/thorproduct.cfm?partnumber=LK4351-UV>
- [63] Bi-concave spherical lens LD4797-UV, <https://www.thorlabs.com/thorproduct.cfm?partnumber=LD4797-UV>
- [64] Sidebottom, H. W., Badcock, C. C., Calvert, J. G., Rabe, B. R., Damon, E. K., Lifetime studies of the biacetyl excited singlet and triplet states in the gas phase at 25°C., *Journal of the American Chemical Society* 94 (1972) 13-19.
- [65] Okabe, H., Noyes, W. A., The relative intensities of fluorescence and phosphorescence in biacetyl vapor., *Journal of the American Chemical Society* (1957) 810-806.

- [66] Malm, H., Sparr, G., Hult, J., Kaminski, C. F., Nonlinear diffusion filtering of images obtained by planar laser-induced fluorescence spectroscopy, *Journal of the Optical Society of America. A, Optics, Image Science, and Vision* 17 (2000) 2148-56.
- [67] Aleiferis, P. G., Hardalupas, Y., Taylor, A. M. K. P., Ishii, K., Urata, Y., Flame chemiluminescence studies of cyclic combustion variations and air-to-fuel ratio of the reacting mixture in a lean-burn stratified-charge spark-ignition engine, *Combustion and Flame* 136 (2004) 72-90.
- [68] Aleiferis, P. G., Taylor, A. M. K. P., Whitelaw, J. H., Ishii, K., Urata, Y., Cyclic Variations of Initial Flame Kernel Growth in a Honda VTEC-E Lean-Burn Spark-Ignition Engine, SAE Technical Paper 2000-01-1207, 2000.
- [69] Salazar, V., Kaiser, S., Influence of the Flow Field on Flame Propagation in a Hydrogen-Fueled Internal Combustion Engine, *SAE International Journal of Engines* (2011) 2376-2394.
- [70] Shahbaz, M. A., Kaiser, S. A., Schütte, M., Berg, T., Characterization of UV endoscopic imaging systems for combustion applications, *Proceedings of the European Combustion Meeting*, 2019.
- [71] Spickermann, M., Abbildung laserinduzierter Kavitationsblasen durch gepulste LED und digitale Spiegelreflexkamera, Master's thesis, University of Duisburg-Essen, 2017.
- [72] Attar, M. A., Zhao, H., Herfatmanesh, M. R., Cairns, A., Turbulent flame boundary and structure detection in an optical DISI engine using tracer-based two-line PLIF technique, *Experimental Thermal and Fluid Science* 68 (2015) 545-558.
- [73] Alger, T., Huang, Y., Hall, M., Matthews, R. D., Liquid Film Evaporation Off the Piston of a Direct Injection Gasoline Engine, SAE Technical Paper 2001-01-1204, 2001.
- [74] Geiler, J. N., Grzeszik, R., Quaing, S., Manz, A., Kaiser, S. A., Development of laser-induced fluorescence to quantify in-cylinder fuel wall films, *SAE International Journal of Engine Research* 19 (2017) 134-147.
- [75] Hochgreb, S., Liquid Fuel Impingement on the Piston Bowl of a Direct-Injection, Spark-Ignited (DISI) Engine under Stratified Operation, SAE Technical Paper 2001-01-3646, 2001.
- [76] Frieden, D., Sick, V., Investigation of the fuel injection, mixing and combustion processes in an SIDI engine using quasi-3D LIF imaging, *SAE Transactions Journal of Engines* 2003 (2003) 270-281.
- [77] Smith, J. D., Sick, V., Real-Time Imaging of Fuel Injection, Ignition and Combustion in a Direct-Injected Spark-Ignition Engine, SAE Technical Paper 2005-01-3753, 2006.
- [78] Schulz, F., Beyrau, F., Systematic Investigation of Fuel Film Evaporation, SAE Technical Paper 2018-01-0310, 2018.
- [79] Schulz, F., Samenfink, W., Schmidt, J., Beyrau, F., Systematic LIF fuel wall film investigation, *Fuel* 172 (2016) 284-292.
- [80] Gessenhardt, C., Zimmermann, F., Schulz, C., Endoscopic imaging LIF diagnostics in IC engines, *Proceedings of the European Combustion Meeting*, 2009.

-
- [81] Luong, M., Zhang, R., Schulz, C., Sick, V., Toluene laser-induced fluorescence for in-cylinder temperature imaging in internal combustion engines, *Applied Physics B: Lasers and Optics* 91 (2008) 669-675.
- [82] Warey, A., Huang, Y., Matthews, R. D., Hall, M., Ng, H., Effects of Piston Wetting on Size and Mass of Particulate Matter Emissions in a DISI Engine, SAE Technical Paper 2002-01-1140, 2002.
- [83] Tran, K. H., Morin, C., Kühni, M., Guibert, P., Fluorescence spectroscopy of anisole at elevated temperatures and pressures, *Applied Physics B: Lasers and Optics* 115 (2013) 461-470.
- [84] Benzler, T., Photo-physical characterization of aromatic compounds for laser-induced fluorescence based diagnostics of fuel concentration, temperature, and equivalence ratio in practical combustion processes, PhD thesis, University of Duisburg-Essen, Duisburg, 2019.
- [85] Faust, S., Dreier, T., Schulz, C., Photo-physical properties of anisole: Temperature, pressure, and bath gas composition dependence of fluorescence spectra and lifetimes, *Applied Physics B: Lasers and Optics* 112 (2013) 203-213.
- [86] Zabeti, S., Aghsaei, M., Fikri, M., Welz, O., Schulz, C., Optical properties and pyrolysis of shock-heated gas-phase anisole, *Proceedings of the Combustion Institute* 36 (2017) 4525-4532.
- [87] Faust, S., Goschütz, M., Kaiser, S. A., Dreier, T., Schulz, C., A comparison of selected organic tracers for quantitative scalar imaging in the gas phase via laser-induced fluorescence, *Applied Physics B: Lasers and Optics* 117 (2014) 183-194.
- [88] Shahbaz, M. A., Goschütz, M., Kaiser, S. A., Endoscopic anisole-LIF imaging of flame propagation and temperature fluctuations in a production SI engine, *Proceedings of the European Combustion Meeting*, 2017.
- [89] Kranz, P., Fuhrmann, D., Goschütz, M., Kaiser, S., Bauke, S., Golibrzuch, K., Wackerbarth, H., Kawelke, P., Luciani, J., Beckmann, L., Zachow, J., Schuette, M., Thiele, O., Berg, T., In-Cylinder LIF Imaging, IR-Absorption Point Measurements, and a CFD Simulation to Evaluate Mixture Formation in a CNG-Fueled Engine, SAE Technical Paper 2018-01-0633, 2018.
- [90] Kranz, P., Imaging of mixing processes in spark-ignition engines via quantitative laser-induced fluorescence, PhD thesis, University of Duisburg-Essen, Duisburg, 2020.
- [91] Cundy, M., Trunk, P., Dreizler, A., Sick, V., Gas-phase toluene LIF temperature imaging near surfaces at 10 kHz, *Experiments in Fluids* 51 (2011) 1169-1176.
- [92] Witzel, O., Klein, A., Wagner, S., Meffert, C., Schulz, C., Ebert, V., High-speed tunable diode laser absorption spectroscopy for sampling-free in-cylinder water vapor concentration measurements in an optical IC engine, *Applied Physics B* 109 (2012) 521-532.
- [93] Berrocal, E., Kristensson, E., Richter, M., Linne, M., Alden, M., Multiple Scattering Suppression in Planar Laser Imaging of Dense Sprays by Means of Structured Illumination, *Atomization and Sprays* 20 (2010) 133-139.

- [94] Mishra, Y. N., Kristensson, E., Koegl, M., Jönsson, J., Zigan, L., Berrocal, E., Comparison between two-phase and one-phase SLIPI for instantaneous imaging of transient sprays, *Experiments in Fluids* 58 (2017)
- [95] Einecke, S., Schulz, C., Sick, V., Measurement of temperature, fuel concentration and equivalence ratio fields using tracer LIF in IC engine combustion, *Applied Physics B: Lasers and Optics* 71 (2000) 717-723.
- [96] Fitzgerald, R. P., Steeper, R., Snyder, J., Hanson, R., Hessel, R., Determination of Cycle Temperatures and Residual Gas Fraction for HCCI Negative Valve Overlap Operation, *SAE International Journal of Engines* 3 (2010) 124-141.
- [97] Pischinger, S., *Lecture notes: Energiewandlungsmaschinen II - Kolbenmaschinen, in Lehrstuhl für Verbrennungskraftmaschinen*, 2007, RWTH-Aachen.
- [98] Khare, R., Shukla, P. K., Temporal Stretching of Laser Pulses in: *Coherence and Ultrashort Pulse Laser Emission*, 2010, p 206-207.
- [99] Shahbaz, M. A., Visualization of the flame-front via OH*-chemiluminescence and laser-induced fluorescence in a near-production engine with endoscopic access., Masters thesis, University of Duisburg-Essen, Duisburg, 2016.
- [100] Shahbaz, M. A., Jüngst, N., Grzeszik, R., Kaiser, S. A., Endoscopic fuel film, chemiluminescence, and soot incandescence imaging in a direct-injection spark-ignition engine, *Proceedings of the Combustion Institute* 38 (2021) 5869-5877.
- [101] Li, J., Huang, Y., Alger, T., Matthews, R. D., Hall, M., Stanglmaier, R. H., Roberts, C. E., Dai, W., Anderson, R. W., Liquid Fuel Impingement on In-Cylinder Surfaces as a Source of Hydrocarbon Emissions From Direct Injection Gasoline Engines, *Journal of Engineering for Gas Turbines and Power* 123 (2001) 659-668.
- [102] Maligne, D., Bruneaux, G., Time-Resolved Fuel Film Thickness Measurement for Direct Injection SI Engines Using Refractive Index Matching, SAE Technical Paper 2011-01-1215, 2011.
- [103] Stanglmaier, R. H., Li, J., Matthews, R. D., The Effect of In-Cylinder Wall Wetting Location on the HC Emissions from SI Engines, SAE Technical Paper 1999-01-0502, 1999.
- [104] Henkel, S., Beyrau, F., Hardalupas, Y., Taylor, A. M., Novel method for the measurement of liquid film thickness during fuel spray impingement on surfaces, *Optics Express* 24 (2016) 2542-2561.
- [105] Stevens, E., Steeper, R., Piston Wetting in an Optical DISI Engine: Fuel Films, Pool Fires, and Soot Generation, SAE Technical Paper 2001-01-1203, 2001.
- [106] Cho, H., Min, K., Measurement of liquid fuel film distribution on the cylinder liner of a spark ignition engine using the laser-induced fluorescence technique, *Measurement Science and Technology* 14 (2003) 975-982.
- [107] Alonso, M., Kay, P. J., Bowen, P. J., Gilchrist, R., Sapsford, S., A laser induced fluorescence technique for quantifying transient liquid fuel films utilising total internal reflection, *Experiments in Fluids* 48 (2009) 133-142.
- [108] Schulz, F., Beyrau, F., The effect of operating parameters on the formation of fuel wall films as a basis for the reduction of engine particulate emissions, *Fuel* 238 (2019) 375-384.

- [109] Schulz, F., Schmidt, J., Beyrau, F., Development of a sensitive experimental set-up for LIF fuel wall film measurements in a pressure vessel, *Experiments in Fluids* 56 (2015)
- [110] Park, S., Ghandhi, J. B., Fuel Film Temperature and Thickness Measurements on the Piston Crown of a Direct-Injection Spark-Ignition Engine, SAE Technical Paper 2005-01-0649, 2005.
- [111] Jüngst, N., Kaiser, S., Imaging of Fuel-Film Evaporation and Combustion in a Direct-Injection Model Experiment, SAE Technical Paper 2019-01-0293, 2019.
- [112] Goschütz, M., Shahbaz, M. A., Shawal, S., Kaiser, S. A., Endoscopic visualization of the early premixed flame kernel in an SI engine by high-speed chemiluminescence imaging and tracer-LIF, *13th International Congress of Engine Combustion Processes: Current Problems and Modern Techniques (ENCOM)*, 2017.

8.1 Publications

8.1.1 Journal publications

1. Shahbaz, M. A., Jüngst, N., Grzeszik, R., Kaiser, S. A., Endoscopic fuel film, chemiluminescence, and soot incandescence imaging in a direct-injection spark-ignition engine, *Proceedings of the Combustion Institute* 38 (2021) 5869-5877. <https://doi.org/10.1016/j.proci.2020.09.004> [100].
2. (In preparation)
Shahbaz, M.A, Kaiser, S.A., Schütte, M, Berg, T., Characterization of different endoscopic imaging systems in visible and ultraviolet range for hostile environments
This paper is based on chapter 4 of this thesis and is currently being prepared for "Applied Optics".

8.1.2 Conference proceedings

1. Shahbaz, M. A, Kaiser, S.A., Schütte, M., Berg, T., 'Characterization of UV endoscopic imaging systems for combustion applications', *Proceedings of the European Combustion Meeting*, 2019. [70]

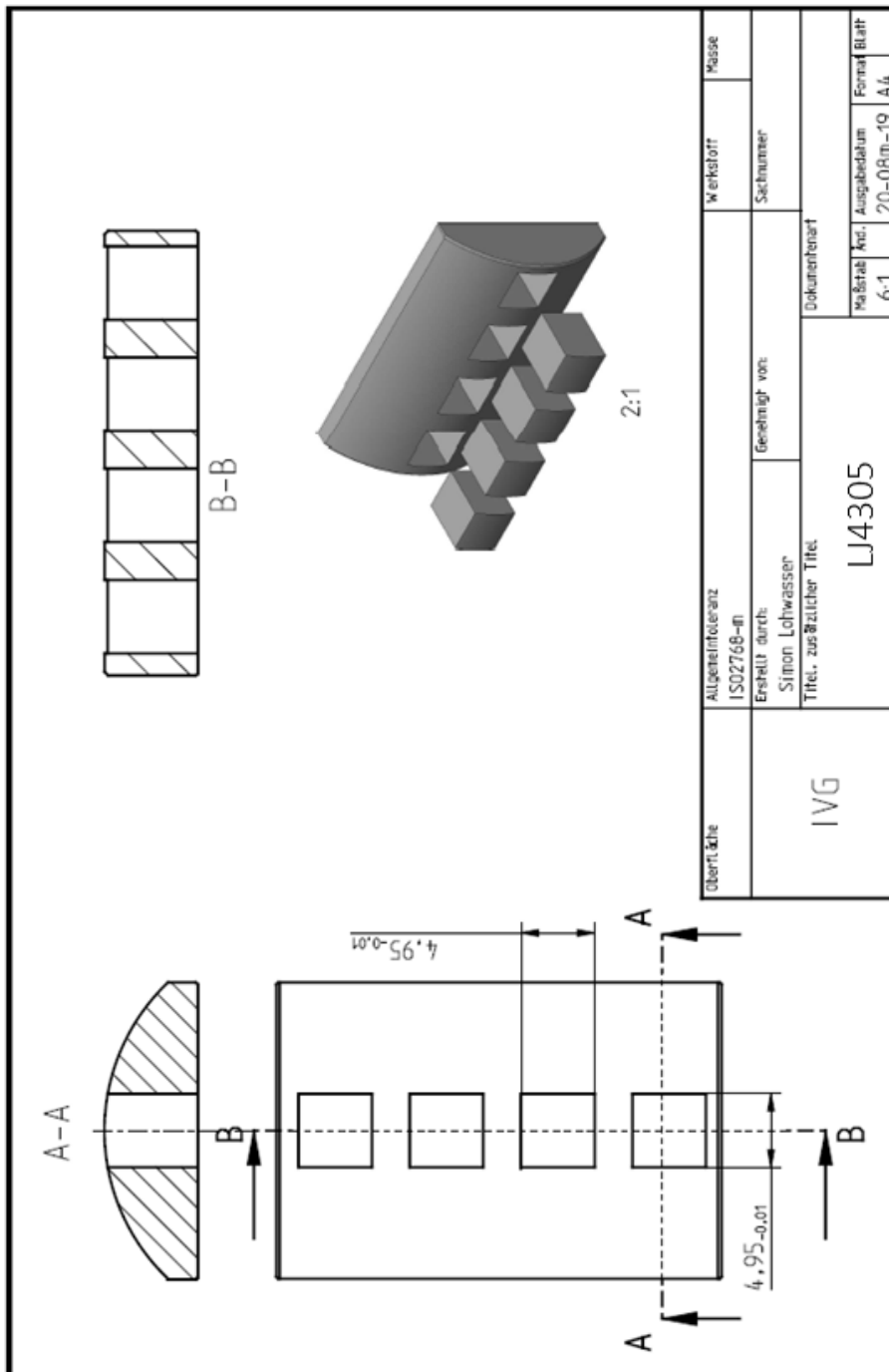
2. Goschütz, M., Shahbaz, M. A., Shawal, S., Kaiser, S.A., 'Endoscopic visualization of the early premixed flame kernel in an SI engine by high-speed chemiluminescence imaging and tracer-LIF', *13th International Congress of Engine Combustion Processes: Current Problems and Modern Techniques (ENCOM)*, 2017. [112]
3. Shahbaz, M. A., Goschütz, M., Kaiser, S.A., 'Endoscopic anisole-LIF imaging of flame propagation and temperature fluctuations in a production SI engine', *Proceedings of the European Combustion Meeting*, 2017. [88]

8.2 Supervised student theses

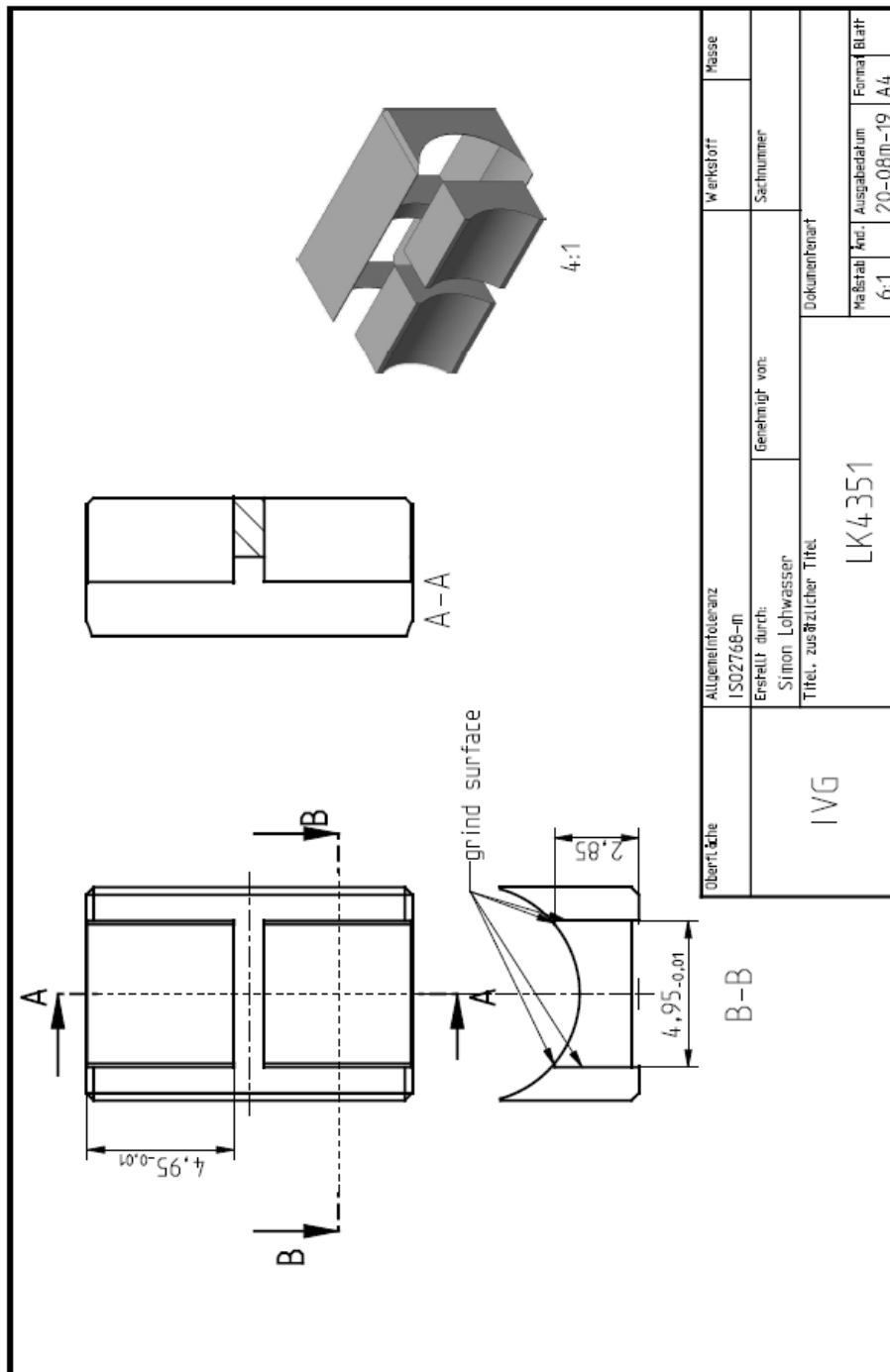
1. Kara, E., ‘*Endoskopische Kraftstoffvisualisierung durch laserinduzierte Fluoreszenz in einem Ottomotor*’, Master thesis, 2019.
2. Karapinar, E., ‘*Charakterisierung eines Distanzmikroskops für ultraviolettes und sichtbares Licht*’, Bachelor thesis, 2019.
3. Shaik, S., ‘*Two-color anisole fluorescence thermometry in a near-production spark-ignition engine with endoscopic access*’, Master thesis, 2018.
4. Daud, S., ‘*Characterization of Selected UV Endoscopic Imaging System*’, Bachelor thesis, 2018.
5. Meller, D., ‘*Charakterisierung der Auflösung und Helligkeit von UV-Endoskopsystemen mittels Modulationsübertragungsfunktion (MTF)*’, Internship, 2018.

9 Appendices

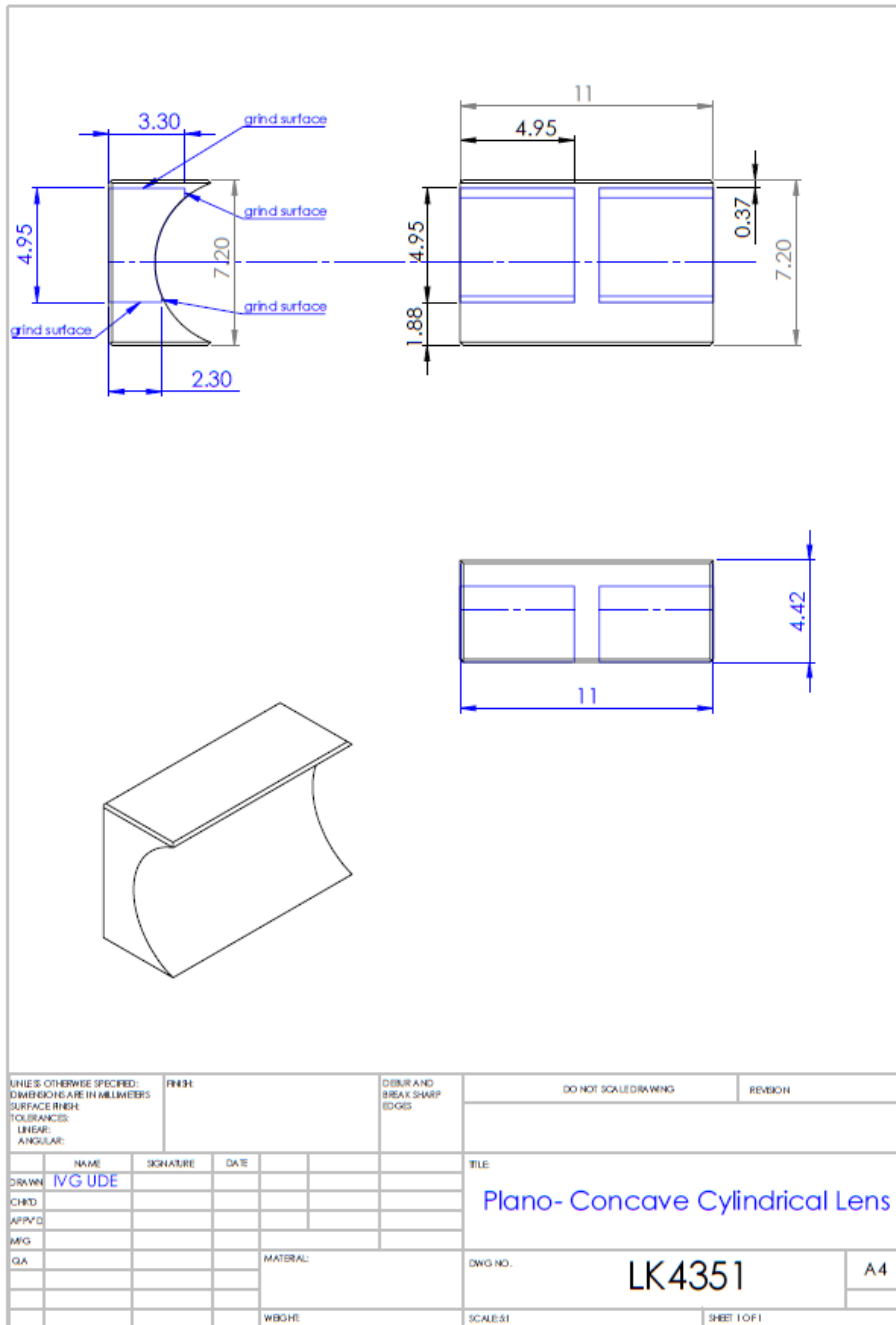
App 1: Plano-convex cylindrical lens for the illumination endoscope and cutting details (For description, see section 3.3.1)



App 2: Plano-concave cylindrical lens for the illumination endoscope and cutting details of the original design (For description, see section 3.3.1)



App 3: Plano-concave cylindrical lens for the illumination endoscope and cutting details of the modified design (For description, see section 3.3.1.1)



Coefficients of interpolation functions in section 5.4.

App 4: Coefficients of interpolation function in Eq 5.1

$$y = ax^b \quad \text{Eq 5.1}$$

p_{O_2} [mbar]	a	b
0	0.000414	1.279
30	0.000795	1.185
70	0.000929	1.173
105	0.000909	1.183
210	0.000674	1.241

App 5: Coefficients of interpolation function in Eq 5.2

$$y = a + b \cdot \exp (cy) \quad \text{Eq 5.2}$$

($a, b,$ and c are constants, $c < 0$)

T [K]	a	b	c
298	1.085	-0.521	-0.0159
375	1.874	-0.832	-0.0110
475	2.514	-1.149	-0.0124
575	3.529	-1.713	-0.0053
675	4.479	-2.040	-0.0038

App 6: Coefficients of interpolation function in Eq 5.4

$$SR = (a + b \cdot \exp (cy)) \cdot (dx^f) \quad \text{Eq 5.4}$$

$a, b, c, d,$ and f are constants, $c < 0$

a	0.168
b	-0.227
c	-0.662
d	0.779
f	0.934

Eidesstattliche Versicherung

Ich versichere an Eides statt durch meine unterstehende Unterschrift,

- Dass ich die vorliegende Arbeit – mit Ausnahme der Anleitung durch die Betreuer – selbstständig ohne fremde Hilfe angefertigt habe
- Dass ich alle Stellen, die wörtlich oder annähernd wörtlich aus fremden Quellen entnommen sind, entsprechend als Zitate gekennzeichnet habe
- Dass ich ausschließlich die angegebenen Quellen (Literatur, Internetseiten, sonstige Hilfsmittel) verwendet habe
- Dass ich alle entsprechenden Angaben nach bestem Wissen und Gewissen vorgenommen habe, dass sie der Wahrheit entsprechen und dass ich nichts verschwiegen habe.

Mir ist bekannt, dass eine falsche Versicherung an Eides Statt nach § 156 und nach § 163 Abs.1 des Strafgesetzbuches mit Freiheitsstrafe oder Geldstrafe bestraft wird.

Lahore, 19.04.2021

Ort, Datum



Muhammad Ali Shahbaz

(Matrkl. Nr.: 3009464)

DuEPublico

Duisburg-Essen Publications online

UNIVERSITÄT
DUISBURG
ESSEN

Offen im Denken

ub | universitäts
bibliothek

Diese Dissertation wird via DuEPublico, dem Dokumenten- und Publikationsserver der Universität Duisburg-Essen, zur Verfügung gestellt und liegt auch als Print-Version vor.

DOI: 10.17185/duepublico/74779

URN: urn:nbn:de:hbz:464-20210916-105027-2

Alle Rechte vorbehalten.